AN INERTIA-CAPACITANCE BEAM SUBSTRUCTURE FORMULATION BASED ON BOND GRAPH TERMINOLOGY WITH APPLICATIONS TO ROTATING BEAM AND WIND TURBINE ROTOR BLADES

by

Yihan Xing

Masters Thesis

Norwegian University of Science and Technology

Submitted to the Department of Marine Technology
in partial fulfillment of the requirements for the degree of

International Masters of Science in Marine Technology (Marine Structures)

September 2010, Trondheim

THIS PAGE INTENTIONALLY LEFT BLANK.

Abstract

In this thesis, an Inertia-Capacitance (IC) beam substructure formulation based on bond graph terminology is developed. The IC beam is formulated in the centre of mass body fixed coordinate system which allows for easy interfacing of the IC beam in a multibody system setting. This multibody floating frame approach is also computationally cheaper than nonlinear finite element methods. Elastic deformations in the IC beam are assumed to be small and described by modal superposition. The formulation couples rigid body motions and elastic deformations in a nonlinear fashion. Detailed derivations for a two-dimensional planar IC beam with bending modes are presented. Brief derivations are also presented for the two-dimensional IC beam with both bending and axial modes and for the three-dimensional IC beam with bending modes. A modal acceleration method via the decoupling of modes is developed for use in the IC beam. The Karnopp-Margolis method is used in the model set-ups to ensure complete integral causality. This results in an efficient numerical system.

The large deflection cantilevered beam and the rotating beam spin-up maneuver problems are solved. Convergence studies of various model parameters are performed. The effects of axial modes in the spin-up maneuver problem are also investigated. Investigations are also made on the hinges used for the substructure interconnections. The IC beam is shown to be capable of solving these problems accurately and efficiently. Lastly, the methodology to apply the IC beam formulation to the wind turbine rotor blades is presented.

THIS PAGE INTENTIONALLY LEFT BLANK.

Acknowledgements

This thesis was performed under the joint supervision of Professor Torgeir Moan and Associate Professor Eilif Pedersen. I would like to thank them for their guidance.

This thesis also concludes the MSc portion of my integrated MSc-PhD study in the Department of Marine Technology. This portion was kindly supported by the Centre of Ships and Ocean Structures (CeSOS). I would like to thank Professor Moan, director for CeSOS for giving me the opportunity to be in this integrated study program. It has been an enriching and rewarding experience studying at the department for the last two years.

THIS PAGE INTENTIONALLY LEFT BLANK.

Contents

List of Figures

List of Tables

1. Introduction

1.1. Background

There has been interest in the design of very large wind turbines in the 10 MW range in recent years. These wind turbines will have large rotor diameters of approximately 175m which employ long slender blades. These long slender blades will exhibit large geometric deformations behavior and thus geometric nonlinear effects should not be ignored. Most of today’s existing commercial wind turbine simulation software use relatively simplified linear structural models and cannot model geometric nonlinearity. There are some software codes that are based on nonlinear finite element methods and can model geometric nonlinear effects. However, finite element methods are slow in solving wind turbine structural dynamics problems which consists of large rigid body motions. Efficiency is particularly important in wind turbines simulations when a large number of load cases are to be simulated, for example when performing fatigue assessments.

1.2. Problem Formulation

In this thesis, the motivation is to develop accurate and efficient flexible beam models that can model the nonlinear dynamics of wind turbine blades. Note that the flexible beam is essentially the basic template model for building wind turbine structural dynamics models.

Efficiency is a key decision making factor in the model development. The beam formulation will be based on the inertia-capacitance (IC) field representation from the bond graph method and thus named the IC beam. The IC field representation provides a compact formulation in integral causality. Integral causality ensures an efficient numerical system. The formulation will describe both rigid body motions and elastic deformations in a coupled fashion. The multibody floating frame approach will be used as this approach is computationally cheaper than the finite element methods. The method of assumed mode shapes will be adopted to provide reduced order descriptions of the elastic deformations. To further increase the efficiency, a specifically developed modal acceleration method will also be proposed. The IC beam will be used in combination with the geometric substructuring technique (discussed in subsection 2.5) to model geometric nonlinear effects. The Karnopp-Margolis method [1] which enforces complete integral causality will be used at the substructure interconnections.

Special focus will be placed on solving the rotating beam problem which is essentially a simplification of the wind turbine rotor problem. Extensive and detailed numerical studies will be performed solving the transient spin-up maneuver problem. Methods to apply the IC beam to the wind turbine rotor blade problem will also be proposed.

1.3. Main Contributions

The main contributions in this thesis are:

i. The formulation of an IC beam substructure based on bond graph terminology.
ii. Proposed and tested a modal acceleration method specifically for the IC beam.
iii. Rigorous testing of IC beam for two-dimensional planar problems. The tests include static bending of a cantilevered beam and the rotating beam spin-up maneuver problem.
iv. Detailed investigations into the hinges used at the IC beam substructure interconnections.
v. Proposed the methodology to apply the IC beam for wind turbine rotor blades.

1.4. Outline of Thesis

In chapter 2, the literature review of this thesis is presented.

In chapter 3, a two-dimensional planar IC beam substructure is derived in detail for an IC beam with two bending modes. The method to include structural damping and modal acceleration is also discussed.

In chapter 4, the procedure of setting up the model including its solution process for the rotating beam problem is presented. Each individual component model that makes up the complete model is also discussed in detail.

In chapter 5, static small and large deflection convergence studies of a cantilevered beam modeled using the IC beam is performed. The large deflection tests include bending of the beam into a complete circle by a tip moment.

In chapter 6, a cantilevered beam modeled using the IC beam is loaded with a time varying point force at its fixed end. The purpose is to highlight the elastic modes coupling feature of the IC beam formulations.

In chapter 7, the rotating beam spin-up maneuver problem is solved using the IC beam. Detailed convergence studies of the model parameters are carried out. These include important parameters such as number of substructures and number of modes prescribed. The modal acceleration technique introduced in this thesis is also applied.

In chapter 8, the IC beam is extended to include axial modes. The spin-up maneuver problem is solved again using the new IC beam and compared against the previous IC beam without axial modes included.

In chapter 9, the effects when using dampers in place of springs and a combination of dampers and springs at the interconnecting hinges are investigated.

In chapter 10, the methodology to apply the IC beam to wind turbine rotor blades is discussed.

In chapter 11, the conclusions of this thesis are made and possible future work proposed.

THIS PAGE INTENTIONALLY LEFT BLANK.

2. Literature Review

Wind turbine structural dynamics involve solving a nonlinear flexible multibody problem. Blade dynamics is essentially a rotating beam problem. Also, modeling the blade flexibility correctly is particularly important. As such, the literature study in this thesis is targeted mainly at these issues. A brief overview of the bond graph method and its application to flexible body modeling is also presented.

2.1. Importance of Blade Model Flexibility

Modeling the blade flexibility correctly is important in wind turbine dynamics problem. The effect of blade model flexibility on the dynamics of the 5MW NREL baseline wind turbine [2] was investigated in Xing [3]. In this investigation, the wind turbine research software HAWC2 [4] was used. The capability of the blade model to capture geometric nonlinearity was controlled by varying the number of blade bodies within the blade model. Within each blade body, the deflections are linear. Prescribing more than one blade body allows the blade to model geometric nonlinear effects. It was found out that it is extremely important to correctly represent the blade model flexibility. A rigid blade assumption produces erroneous solutions of as much as 20% errors for both the local and global responses. A linear elastic blade achieves below 5% error for the global responses however there will still be more than 10% errors in the local blade responses. Finally, it was shown that below 5% errors will be achieved when just three blade bodies are prescribed. In Ahlstrom [5], the influence of wind turbine flexibility on the loads and power productions were investigated. The wind turbine blade stiffness and mass were proportionally scaled together to vary its slenderness while keeping the natural frequencies intact. It was found out that large blade deflections have a significant influence on both the power production and the resulting structural loads. These influences are as much as 50% in some cases.

2.2. Nonlinear Dynamics of Wind Turbine

In Larsen, *et.al.* [6], the nonlinear couplings between the fundamental flapwise and edgewise modes of wind turbine blades were identified and investigated. Internal resonances between these modes have also been studied. In another of their work [7], the numerical stability of the wind turbine blade based on a nonlinear model was investigated through the Lyapunov exponent approach. In Holm-Jørgensen's PhD thesis [8], the nonlinear dynamics of wind turbines were investigated. Model reductions based on component mode synthesis were also performed on a nonlinear model of the wind turbine.

2.3. The Rotating Beam Problem

The rotating beam problem has been investigated by a number of researchers. In linear structural theory, the transverse vibrations of the beam are not coupled to the axial forces. However, the presence of centrifugal forces in a rotating beam gives rise to geometric or stress stiffening effect. This makes the beam stiffer in bending as would be predicted by linear theory. In Ryu, *et.al.* [9], a criterion on inclusion of stress stiffening effects in flexible multibody systems was presented. This criterion is based on the eigenvalue variation of the total modal stiffness. If the variation is large, then stress stiffening effects must be included. The coupling of the bending stiffness of the beam to the axial forces makes the rotating beam a nonlinear problem.

In Yang, Jiang and Chen [10], the complete set of ordinary differential equations for a rotating Euler-Bernoulli beam was derived and presented. There are also other various works [11], [12], [13], [14] that focus on analysis of the rotating cantilevered beam problem.

2.4. Nonlinear Flexible Multibody Modeling

There has been extensive research into modeling of nonlinear flexible multibody dynamics over the last few decades. Wasfy and Noor [15] performed a review of the status and progress in the research of flexible multibody dynamics. In their paper, they classified and compared three types of reference frames approach: floating frame, corotational frame and inertia frame.

Pierre, Jiang, Shaw, Pesheck and Legrand used the method of nonlinear modes based on the invariant manifold approach to perform a series of nonlinear structural dynamics modeling. This included the modeling of flexible multibody systems. Their various works can be found in [16], [17], [18], [19], [20], [21], [22], [23]. An overview of nonlinear modes and their applications in vibration problems can be found in Vakakis [24].

2.5. Geometric Substructuring Technique

In this technique, each body is divided into a number of substructures. In each substructure, the displacements are small and thus linear theory can be applied. The substructures together allow the body to model large deflections. This technique allows the use of modal reduction and floating reference frames to model large deflection problems. This technique is discussed in Wu and Hang [25], [26] and Liu and Liew [27] and applied in HAWC2 [4].

2.6. Mode Superposition Method

Mode superposition in structural dynamic analysis can be applied in two forms: the modal displacement method and the modal acceleration method.

The modal displacement method is the widely known classical method for mode superposition. In this method, the structural displacements are calculated based on the response from a selected group of modal coordinates; the rest are truncated. These can be based on eigenmodes, Ritz modes or any other types of assumed mode shapes. In general, satisfactory accuracy is obtained for the displacements if only a few modal coordinates are selected. More modes must be used in order to attain the same accuracy for internal forces and stress [28]. In general, it is recommended that modes are retained up to a frequency of at least a factor of 2 but not more than 5 higher than the highest frequency of interest, section 10.3 Karnopp, Margolis and Rosenberg [29].

This process of mode truncation introduces error in the responses. This is particularly true if the response of the structure is stiffness controlled. This error can be minimized by the modal acceleration method where the static responses of the truncated modes are considered in the total responses instead of being totally eliminated. This was introduced by Williams [30] and Bisplinghoff, *et.al.* [31]. In Soriano, *et.al.* [28], three mathematically equivalent versions of the modal acceleration method were presented. These are the Maddox [32], Hanstenn and Bell [33] and Cornweel, Craig and Johnson [34] versions. Modal acceleration was also applied in Ryu, *et.al.* [35] to improve the dynamic solutions of flexible multibody dynamics.

The Maddox [32] version of modal acceleration is presented here. First, the total response ***v*** and the force vector ***F*** are divided into two portions:

$$\begin{aligned}\vec{v} &= \vec{v}_{MDM} + \vec{v}_{MAM} \\ &= \vec{\phi}_{MDM}\vec{q}_{MDM} + \vec{\phi}_{MAM}\vec{q}_{MAM}\end{aligned} \tag{2.1}$$

$$\begin{aligned}\vec{F} &= \vec{F}_{MDM} + \vec{F}_{MAM} \\ &= \vec{\phi}_{MDM}\vec{Q}_{MDM} + \vec{\phi}_{MAM}\vec{Q}_{MAM}\end{aligned} \tag{2.2}$$

The vectors subscripts *MDM* and *MAM* in equations (2.1) and (2.2) denote vectors associated with the mode displacement method and mode acceleration method respectively. Here, mode displacement method is applied on modes *i = 1, m* and mode acceleration method is applied on the remaining higher modes *i = m+1, N*. The equations to solve for are:

$$\begin{aligned}\bar{m}_j\ddot{q}_j + \bar{c}_j\dot{q}_j + \bar{k}_j q_j = Q_j \qquad &, j = 1,\dots,m \qquad (MDM) \\ \bar{k}_j q_j = Q_j \qquad &, j = m+1,\dots,N \quad (MAM)\end{aligned} \tag{2.3}$$

2.7. The Bond Graph Method

The bond graph method is an intuitive representation of the physical system. It consists of an energy-conserving network of bonds (represented by lines) and lumped parameter elements of resistance, capacitance and inductance (represented by symbols). Energy is exchanged between the elements through the bonds as a combination of effort (force) and flow (velocity). The system equations are then derived automatically from the bond graph representation and then used for the simulation process. Some fundamental aspects of the bond graph method are presented in this subsection. For an extensive and detailed overview of this method, see Karnopp, Margolis and Rosenberg [29] and Pedersen and Engja [36].

The energy is interchanged via the power conjugate of effort and flow variables. There is a pair of power conjugate variables in every engineering domain; refer to Table 1.

Table 1: Power Conjugate Variables of Some Engineering Domains

Domain	Effort	Flow
Electric	Voltage	Current
Translational Mechanics	Force	Velocity
Rotational Mechanics	Torque	Angular velocity
Hydraulics	Pressure	Volumetric flow rate
Thermal	Temperate	Entropy flow

The bond graph method utilizes nine basic elements. They are listed in Table 2. Energy is supplied to a system by efforts and flow sources. The capacitor and inductor elements perform energy storage. Resistor elements dissipate energy away from the system. The transformer and gyrator elements perform energy transmission. The relationships between the efforts and flows in the system are represented by the 0- and 1-junctions. All elements except the junctions can represent nonlinearity.

The computational causality in bond graphs is indicated by causal strokes. A casual stroke is added to one end of a power bond to indicate that the effort/flow signal is directed towards/away from this end. For the energy storage elements, the causality can be integral or differential. Integral causality means that the output of the element is obtained from the integration of the input. And, differential causality means that the output of the element is obtained from the differentiation of the input. Differential causalities often lead to inefficient numerical systems. Therefore complete integral causality is preferred. The causality of all the elements in a bond graph model must also be assignable. The causal strokes associated with the nine basic elements are presented in Table 2. Differential causality strokes are denoted in red.

Table 2: Basic Bond Graph Elements

Element	**Symbol**	**Equation**
Effort source	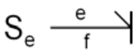	$e=e(t)$
Flow source	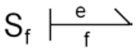	$f=f(t)$
Capacitor	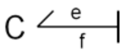 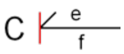	$e=\Phi_C^{-1}\left(\int_t f\,dt\right)$ $f=\frac{d}{dt}\Phi_C(e)$
Inductor	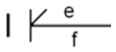 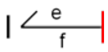	$f=\Phi_I^{-1}\left(\int_t e\,dt\right)$ $e=\frac{d}{dt}\Phi_I(f)$
Resistor	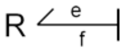 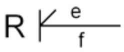	$e=\Phi_R(f)$ $f=\Phi_R^{-1}(e)$
Transformer	 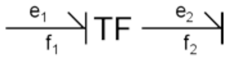	$e_1=me_2,\quad f_2=mf_1$ $f_1=f_2/m,\quad e_2=e_1/m$
Gyrator	 	$e_1=rf_2,\quad e_2=rf_1$ $f_1=e_2/r,\quad f_2=e_1/r$
0-junction	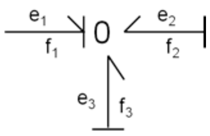	$e_2=e_1$ $e_3=e_1$ $f_1=-(f_2+f_3)$
1-junction	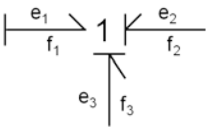	$f_2=f_1$ $f_3=f_1$ $e_1=-(e_2+e_3)$

2.7.1. The Bond Graph Force-Free Beam Model

The force-free beam bond graph model refers to the formulations discussed in section 10.2, Karnopp, Margolis and Rosenberg [29] and Margolis [37]. The motion of the beam is described by the superposition of decoupled rigid body motions and elastic deformations. Also, the elastic deformations are represented by the sum of assumed mode shapes. The force-free beam has been applied in a number of cases, for example, the bond graph models of a wind turbine rotor in Xing [38] and vehicle A-frame structure in Margolis [37].

A bond graph force-free beam model with two elastic modes is presented in Figure 1. Inductor elements represent the masses (translational, rotational and modal). Capacitor elements represent the modal stiffness and resistor elements represent the modal damping. The transformer elements represent the calculations of the contributions from the point forces to the generalized forces to the rigid body and elastic modes.

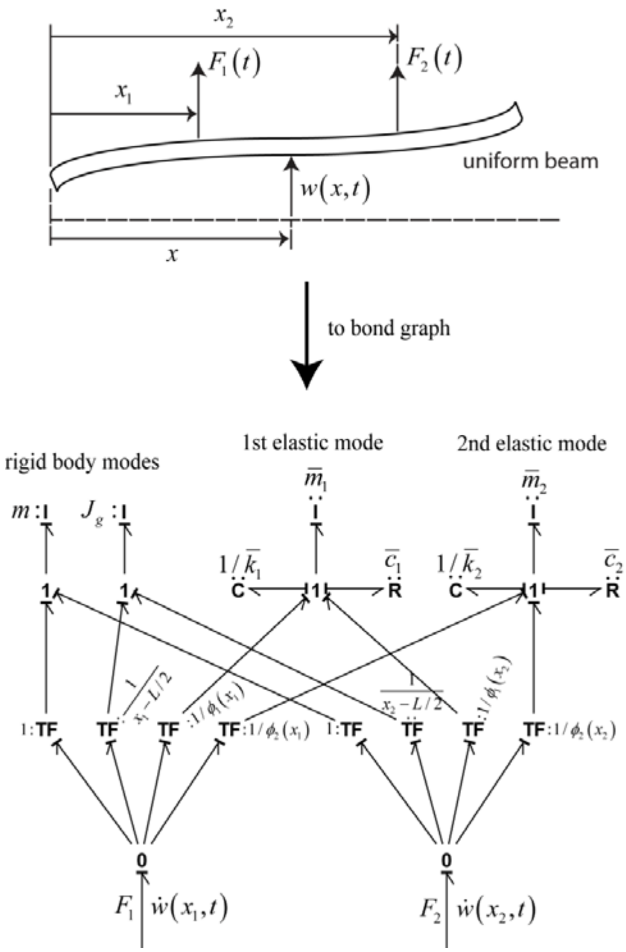

Figure 1: The Bond Graph Force-Free Beam Model

The mode shape deflection and slope must nonzero at a connection point to have nonzero generalized force contributions to the elastic modes from forces and/or moments at that point. This means that the mode shape deflection and slope at the fixed end of the rotating beam must be nonzero. Otherwise, there is no energy transfer from the forces and/or moments from the fixed end to the elastic modes. This represents a serious drawback for this formulation. This is because the force-free mode shapes which are non optimum mode shapes would have to be employed. This leads to slow modal convergence.

3. The Inertia-Capacitance Beam Substructure

In this section, the proposed Inertia-Capacitance (IC) beam substructure formulation will be derived. Details of the IC-field formulation procedure is discussed in section 9.2.3 Karnopp, Margolis and Rosenberg [29] and Karnopp [39]. This procedure was also used in Xing [38] for a single blade wind turbine rotor system.

Axial deformation is assumed to be small and thus neglected, i.e. the beam exhibits only lateral deformations. The validity of this assumption will be investigated in section 8, where the IC beam will be extended to include axial modes, and numerical studies performed to investigate the effect when axial modes are included for the rotating beam problem.

The elastic deformations within the IC beam substructure are assumed to be small. Thus linear theory is valid and modal superposition is used. The total motion of the IC beam substructure will be the sum of the rigid body motions and the elastic vibrations. The centre of mass body fixed coordinate system is used. The rotational inertial properties remain invariant and the products of inertia are zero in this coordinate system. Also, a body fixed coordinate system allows for easy mating of the IC beam to other bodies in a multibody system setting. For the ease of understanding, the IC beam will be formulated for two-dimensional planar motions, i.e. translations in the X-Y plane and rotations about the Z-axis. The formulation presented herein can be easily further extended to account for full three-dimensional motions. The IC beam formulation uses displacements and momentums as state variables. It is also a model in complete integral causality which means that its numerical system is efficient and easy to solve for.

First, the generalized form of the equations for the IC beam will be derived. Next, the full set of equations will be further developed for an example of the IC beam with two elastic modes. Lastly, a modal acceleration technique relating specifically to the IC beam will be introduced.

3.1. Derivation of the Equations for the 2D Planar IC Beam

3.1.1. Preliminaries

Consider a vibrating two-dimensional planar beam translating and rotating in space as illustrated in Figure 2. The coordinate system a_1–a_2 is fixed to the centre of mass. Note that all formulations refer to this body-fixed coordinate system. Notice that a point P_0 on the beam in the un-deformed state will move to point P after deformation.

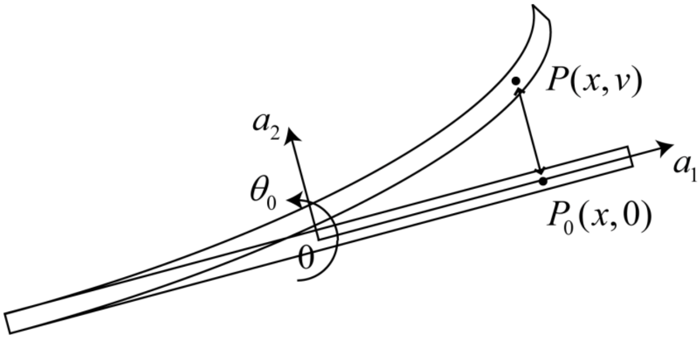

Figure 2: 2D Planar IC Beam Substructure

Expression for velocities along the beam

Velocity of point P:

$$\vec{V}_P = \vec{V}_0 + \left(-v\dot{\theta}_0\right)\vec{a}_1 + \left(x\dot{\theta}_0 + \dot{v}\right)\vec{a}_2 \tag{3.1}$$

Velocity of centre of mass:

$$\vec{V}_0 = \dot{x}_0\vec{a}_1 + \dot{y}_0\vec{a}_2 \tag{3.2}$$

Therefore velocity of point P:

$$\vec{V}_P = \left(\dot{x}_0 - v\dot{\theta}_0\right)\vec{a}_1 + \left(\dot{y}_0 + x\dot{\theta}_0 + \dot{v}\right)\vec{a}_2 \tag{3.3}$$

3.1.2. Expressions for Kinetic and Potential Energies

Expression for kinetic energy

Kinetic energy of the IC beam:

$$\begin{aligned} T &= \frac{1}{2}\int_{-\frac{L}{2}}^{\frac{L}{2}} m\left|\vec{V}_P\right|^2 dx \\ &= \frac{1}{2}\int_{-\frac{L}{2}}^{\frac{L}{2}} m\left(\dot{x}_0^2 + \dot{y}_0^2 + x^2\dot{\theta}_0^2 + 2x\dot{y}_0\dot{\theta}_0\right)dx \\ &+ \frac{1}{2}\int_{-\frac{L}{2}}^{\frac{L}{2}} m\left(-2v\dot{x}_0\dot{\theta}_0 + v^2\dot{\theta}_0^2 + \dot{v}^2 + 2\dot{v}\dot{y}_0 + 2x\dot{v}\dot{\theta}_0\right)dx \end{aligned} \tag{3.4}$$

The first group of terms on the RHS of equation (3.4) is associated to the rigid body motions. The second group of terms is associated to both the rigid body motions and the elastic vibrations.

The first group of terms:

$$\begin{aligned} \frac{1}{2}\int_{-\frac{L}{2}}^{\frac{L}{2}} m\left(\dot{x}_0^2 + \dot{y}_0^2 + x^2\dot{\theta}_0^2\right)d \ &= \frac{1}{2}M\left(\dot{x}_0^2 + \dot{y}_0^2\right) + \frac{1}{2}J_0\dot{\theta}_0^2 \\ \frac{1}{2}\int_{-\frac{L}{2}}^{\frac{L}{2}} m\left(2x\dot{y}_0\dot{\theta}_0\right)dx &= 0 \end{aligned} \tag{3.5}$$

The result in the second line in equation (3.5) is zero due to the fact that the coordinate system is fixed at the centre of mass. This term relates to the cross products of inertia which are zero in a centre of mass body fixed coordinate system.

The elastic deformations are then described using the method of assumed modes:

$$\begin{aligned} v &= \sum_{j=1}^{N} Y_j v_j \\ \dot{v} &= \sum_{j=1}^{N} Y_j \dot{v}_j \end{aligned} \tag{3.6}$$

Using equation (3.6) in the second group of terms in equation (3.4):

$$\begin{aligned}\frac{1}{2}\int_{-\frac{L}{2}}^{\frac{L}{2}} m\left(-2v\dot{x}_0\dot{\theta}_0\right)dx &= -\left[\int_{-\frac{L}{2}}^{\frac{L}{2}} m\sum_{j=1}^{N} Y_j v_j\,dx\right]\dot{x}_0\dot{\theta}_0\\ &= -\sum_{j=1}^{N}\left[\int_{-\frac{L}{2}}^{\frac{L}{2}} mY_j\,dx\right]v_j\dot{x}_0\dot{\theta}_0\\ &= -\sum_{j=1}^{N}\bar{m}_{v,j}v_j\dot{x}_0\dot{\theta}_0\end{aligned}\tag{3.7}$$

$$\begin{aligned}\frac{1}{2}\int_{-\frac{L}{2}}^{\frac{L}{2}} m\left(v^2\dot{\theta}_0^2\right)dx &= \frac{1}{2}\left[\int_{-\frac{L}{2}}^{\frac{L}{2}} m\sum_{j=1}^{N}\sum_{k=1}^{N} Y_jY_kv_jv_k\,dx\right]\dot{\theta}_0^2\\ &= \frac{1}{2}\left[\sum_{j=1}^{N}\int_{-\frac{L}{2}}^{\frac{L}{2}} mY_j^2\,dx\right]v_j^2\dot{\theta}_0^2\\ &= \frac{1}{2}\sum_{j=1}^{N}\bar{m}_{vv,j}v_j^2\dot{\theta}_0^2\end{aligned}\tag{3.8}$$

$$\begin{aligned}\frac{1}{2}\int_{-\frac{L}{2}}^{\frac{L}{2}} m\left(\dot{v}^2\right)dx &= \frac{1}{2}\left[\int_{-\frac{L}{2}}^{\frac{L}{2}} m\sum_{j=1}^{N}\sum_{k=1}^{N} Y_jY_k\dot{v}_j\dot{v}_k\,dx\right]\\ &= \frac{1}{2}\left[\sum_{j=1}^{N}\int_{-\frac{L}{2}}^{\frac{L}{2}} mY_j^2\,dx\right]\dot{v}_j^2\\ &= \frac{1}{2}\sum_{j=1}^{N}\bar{m}_{vv,j}\dot{v}_j^2\end{aligned}\tag{3.9}$$

$$\begin{aligned}\frac{1}{2}\int_{-\frac{L}{2}}^{\frac{L}{2}} m\left(2\dot{v}\dot{y}_0\right)dx &= \left[\int_{-\frac{L}{2}}^{\frac{L}{2}} m\sum_{j=1}^{N} Y_j\dot{v}_j\,dx\right]\dot{y}_0\\ &= \left[\sum_{j=1}^{N}\int_{-\frac{L}{2}}^{\frac{L}{2}} mY_j\,dx\right]\dot{v}_j\dot{y}_0\\ &= \sum_{j=1}^{N}\bar{m}_{v,j}\dot{v}_j\dot{y}_0\end{aligned}\tag{3.10}$$

$$\begin{aligned}\frac{1}{2}\int_{-\frac{L}{2}}^{\frac{L}{2}} m\left(2x\dot{v}\dot{\theta}_0\right)dx &= \left[\int_{-\frac{L}{2}}^{\frac{L}{2}} mx\sum_{j=1}^{N} Y_j\dot{v}_j\,dx\right]\dot{\theta}_0\\ &= \left[\sum_{j=1}^{N}\int_{-\frac{L}{2}}^{\frac{L}{2}} mxY_j\,dx\right]\dot{v}_j\dot{\theta}_0\\ &= \sum_{j=1}^{N}\bar{m}_{xv,j}\dot{v}_j\dot{\theta}_0\end{aligned}\tag{3.11}$$

Re-expressing equation (3.4) using equations (3.7) to (3.11):

$$\begin{aligned} T &= \frac{1}{2}M\dot{x}_0^2 + \frac{1}{2}M\dot{y}_0^2 + \frac{1}{2}J_0\dot{\theta}_0^2 \\ &\quad -\sum_{j=1}^{N}\bar{m}_{v,j}v_j\dot{x}_0\dot{\theta}_0 + \frac{1}{2}\sum_{j=1}^{N}\bar{m}_{vv,j}v_j^2\dot{\theta}_0^2 + \frac{1}{2}\sum_{j=1}^{N}\bar{m}_{vv,j}\dot{v}_j^2 + \sum_{j=1}^{N}\bar{m}_{v,j}\dot{v}_j\dot{y}_0 + \sum_{j=1}^{N}\bar{m}_{xv,j}\dot{v}_j\dot{\theta}_0 \end{aligned} \tag{3.12}$$

Where,

$$\begin{aligned} \bar{m}_{v,j} &= \int_{-\frac{L}{2}}^{\frac{L}{2}} mY_j dx \\ \bar{m}_{vv,j} &= \int_{-\frac{L}{2}}^{\frac{L}{2}} mY_j^2 dx \\ \bar{m}_{xv,j} &= \int_{-\frac{L}{2}}^{\frac{L}{2}} mxY_j dx \end{aligned} \tag{3.13}$$

A quick inspection into the second line of equation (3.12) reveals that the elastic kinetic energy is a combination of coupled energy contributions from both rigid body motions and elastic deformations. Obviously, this is physically correct.

This is different from the bond graph model of the force-free beam described in section 10.2, Karnopp, Margolis and Rosenberg [29] and Margolis [37] where the rigid body motions are completely decoupled from the elastic vibrations. This formulation and its disadvantages were discussed in subsection 2.7.1.

Expression for potential energy

Potential energy of the IC beam:

$$\begin{aligned} V &= \frac{1}{2}\int_{-\frac{L}{2}}^{\frac{L}{2}} EI\left(\frac{\partial^2 v}{\partial x^2}\right)^2 dx \\ &= \frac{1}{2}\left[\int_{-\frac{L}{2}}^{\frac{L}{2}} EI\sum_{j=1}^{N}\sum_{k=1}^{N} Y_j'' Y_k'' v_j v_k\right] dx \\ &= \frac{1}{2}\left[\sum_{j=1}^{N}\int_{-\frac{L}{2}}^{\frac{L}{2}} EI\left(Y_j''\right)^2 dx\right] v_j^2 \\ &= \frac{1}{2}\sum_{j=1}^{N}\bar{k}_{v,j}v_j^2 \end{aligned} \tag{3.14}$$

Where,

$$\bar{k}_{v,j} = \int_{-\frac{L}{2}}^{\frac{L}{2}} EI\left(Y_j''\right)^2 dx \tag{3.15}$$

Unlike the elastic kinetic energy, the elastic potential energy depends solely on the elastic deformations.

3.1.3. Applying the Lagrange equations

The Lagrange equations in quasi-coordinates as described in Meriovitch [40], [41] will be applied for the rigid body motion variables. This is because the IC beam is formulated in the body fixed coordinate system. These equations have also been applied for the bond graph model for rotor dynamics problems in Pedersen [42]. On the other hand, the usual generalized form of Lagrange equations will be applied for the elastic deformation variables as they are described in the local body-fixed coordinates.

The Lagrange equations in quasi-coordinates:

$$\begin{gathered} \frac{d}{dt}\left(\frac{\partial T}{\partial \dot{\vec{x}}}\right) + \dot{\vec{\theta}} \times \frac{\partial T}{\partial \dot{\vec{x}}} = \vec{F}_x \\ \frac{d}{dt}\left(\frac{\partial T}{\partial \dot{\vec{\theta}}}\right) + \dot{\vec{\theta}} \times \frac{\partial T}{\partial \dot{\vec{\theta}}} + \vec{r}_c \times \frac{\partial T}{\partial \dot{\vec{x}}} = \vec{F}_\theta \end{gathered} \tag{3.16}$$

The usual generalized form of Lagrange equations:

$$\frac{d}{dt}\left(\frac{\partial L}{\partial \dot{q}_k}\right) - \frac{\partial L}{\partial q_k} = Q_k \tag{3.17}$$

Where the Lagrangian is given by:

$$L = T - V \tag{3.18}$$

From equation (3.14), as the potential energy V is only a function of the generalized displacements related to the elastic deformations of the beam, this means that:

$$\begin{aligned} \frac{\partial V}{\partial \dot{\vec{x}}} &= 0 \\ \frac{\partial V}{\partial \dot{\vec{\theta}}} &= 0 \\ \frac{\partial V}{\partial \dot{q}_k} &= 0 \end{aligned} \tag{3.19}$$

Therefore, equations (3.16) and (3.17) can be simplified to:

$$\begin{aligned} \frac{d}{dt}\left(\frac{\partial T}{\partial \dot{\vec{x}}}\right) + \dot{\vec{\theta}} \times \frac{\partial T}{\partial \dot{\vec{x}}} &= \vec{F}_x \\ \frac{d}{dt}\left(\frac{\partial T}{\partial \dot{\vec{\theta}}}\right) + \dot{\vec{\theta}} \times \frac{\partial T}{\partial \dot{\vec{\theta}}} + \vec{r}_c \times \frac{\partial T}{\partial \dot{\vec{x}}} &= \vec{F}_\theta \end{aligned} \tag{3.20}$$

$$\frac{d}{dt}\left(\frac{\partial T}{\partial \dot{q}_k}\right) - \frac{\partial T}{\partial q_k} + \frac{\partial V}{\partial q_k} = Q_k \tag{3.21}$$

Furthermore as this is a two-dimensional planar beam with its coordinate system fixed to the centre of mass, equations (3.20) and (3.21) can be further simplified to:

$$\begin{aligned} \frac{d}{dt}\left(\frac{\partial T}{\partial \dot{x}_0}\right) - \dot{\theta}_0 \frac{\partial T}{\partial \dot{y}_0} &= F_{x_0} \\ \frac{d}{dt}\left(\frac{\partial T}{\partial \dot{y}_0}\right) + \dot{\theta}_0 \frac{\partial T}{\partial \dot{x}_0} &= F_{y_0} \\ \frac{d}{dt}\left(\frac{\partial T}{\partial \dot{\theta}_0}\right) &= F_\theta \\ \frac{d}{dt}\left(\frac{\partial T}{\partial \dot{v}_j}\right) - \frac{\partial T}{\partial v_j} + \frac{\partial V}{\partial v_j} &= F_{v_j} \end{aligned} \tag{3.22}$$

The first three lines in equation (3.22) correspond to the rigid body motions while the last line corresponds to the elastic deformation.

Equation (3.22) is then re-written in the form suitable for the IC-field implementation:

$$\begin{aligned}
\frac{d}{dt}\left(\frac{\partial T}{\partial \dot{x}_0}\right) &= F_{x_0} + \dot{\theta}_0 \frac{\partial T}{\partial \dot{y}_0} = F_x + e'_{x_0} \\
\frac{d}{dt}\left(\frac{\partial T}{\partial \dot{y}_0}\right) &= F_{y_0} - \dot{\theta}_0 \frac{\partial T}{\partial \dot{x}_0} = F_y + e'_{y_0} \\
\frac{d}{dt}\left(\frac{\partial T}{\partial \dot{\theta}_0}\right) &= F_{\theta_0} = F_{\theta_0} + e'_{\theta_0} \\
\frac{d}{dt}\left(\frac{\partial T}{\partial \dot{v}_j}\right) &= F_{q_j} + \frac{\partial T}{\partial v_j} - \frac{\partial V}{\partial v_j} = F_{v_j} + e'_{v_j}
\end{aligned} \tag{3.23}$$

Where,

$$\begin{aligned}
e'_{x_0} &= \dot{\theta}_0 \frac{\partial T}{\partial \dot{y}_0} \\
e'_{y_0} &= -\dot{\theta}_0 \frac{\partial T}{\partial \dot{x}_0} \\
e'_{\theta_0} &= 0 \\
e'_{v_j} &= \frac{\partial T}{\partial v_j} - \frac{\partial V}{\partial v_j}
\end{aligned} \tag{3.24}$$

Recognize that the LHS of equation (3.23) are the time derivatives of the generalized momentums, thus the equation can be further simplified to:

$$\begin{aligned}
\dot{P}_{x_0} &= F_x + e'_{x_0} \\
\dot{P}_{y_0} &= F_y + e'_{y_0} \\
\dot{P}_{\theta_0} &= F_{\theta_0} + e'_{\theta_0} \\
\dot{P}_{v_j} &= F_{v_j} + e'_{v_j}
\end{aligned} \tag{3.25}$$

3.2. Derivation of IC beam Equations using Two Elastic Modes

The derivation in subsection 3.1 is further developed here using only two elastic modes. This is for the ease of presenting and understanding the subsequent derivations of the equations. It will be straight forward to extend the derived formulations presented here to incorporate any additional number of modes desired.

Expressions for the kinetic and potential energies

$$\begin{aligned} T = {} & \frac{1}{2}M\dot{x}_0^2 + \frac{1}{2}M\dot{y}_0^2 + \frac{1}{2}J_0\dot{\theta}_0^2 \\ & -\overline{m}_{v,1}v_1\dot{x}_0\dot{\theta}_0 + \frac{1}{2}\overline{m}_{vv,1}v_1^2\dot{\theta}_0^2 + \frac{1}{2}\overline{m}_{vv,1}\dot{v}_1^2 + \overline{m}_{v,1}\dot{v}_1\dot{y}_0 + \overline{m}_{xv,1}\dot{v}_1\dot{\theta}_0 \\ & -\overline{m}_{v,2}v_2\dot{x}_0\dot{\theta}_0 + \frac{1}{2}\overline{m}_{vv,2}v_2^2\dot{\theta}_0^2 + \frac{1}{2}\overline{m}_{vv,2}\dot{v}_2^2 + \overline{m}_{v,2}\dot{v}_2\dot{y}_0 + \overline{m}_{xv,2}\dot{v}_2\dot{\theta}_0 \end{aligned} \tag{3.26}$$

$$V = \frac{1}{2}\overline{k}_{v,1}v_1^2 + \frac{1}{2}\overline{k}_{v,2}v_2^2 \tag{3.27}$$

Rigid body terms in equation (3.23)

$$\begin{aligned} \frac{\partial T}{\partial \dot{x}_0} &= M\dot{x}_0 - \overline{m}_{v,1}v_1\dot{\theta}_0 - \overline{m}_{v,2}v_2\dot{\theta}_0 \\ \frac{\partial T}{\partial \dot{y}_0} &= M\dot{y}_0 + \overline{m}_{v,1}\dot{v}_1 + \overline{m}_{v,2}\dot{v}_2 \\ \frac{\partial T}{\partial \dot{\theta}_0} &= J_0\dot{\theta}_0 - \overline{m}_{v,1}v_1\dot{x}_0 + \overline{m}_{vv,1}v_1^2\dot{\theta}_0 + \overline{m}_{xv,1}\dot{v}_1^2 \\ & \quad -\overline{m}_{v,2}v_2\dot{x}_0 + \overline{m}_{vv,2}v_2^2\dot{\theta}_0 + \overline{m}_{xv,2}\dot{v}_2^2 \end{aligned} \tag{3.28}$$

Elastic deformation terms in equation (3.23)

$$\begin{aligned} \frac{\partial T}{\partial \dot{v}_j} &= \overline{m}_{vv,j}\dot{v}_j + \overline{m}_{v,j}\dot{y}_0 + \overline{m}_{xv,j}\dot{\theta}_0 \qquad ; j = 1,2 \\ \frac{\partial T}{\partial v_j} &= -\overline{m}_{v,j}\dot{x}_0\dot{\theta}_0 + \overline{m}_{vv,j}v_j\dot{\theta}_0^2 \\ \frac{\partial V}{\partial v_j} &= \overline{k}_{v,j}v_j \end{aligned} \tag{3.29}$$

Equations for IC-field implementation

Momentums are related to the kinetic energies by:

$$\begin{bmatrix} \dfrac{\partial T}{\partial \dot{x}_0} & \dfrac{\partial T}{\partial \dot{y}_0} & \dfrac{\partial T}{\partial \dot{\theta}_0} & \dfrac{\partial T}{\partial \dot{v}_1} & \dfrac{\partial T}{\partial \dot{v}_2} \end{bmatrix}^T = \begin{bmatrix} P_{x_0} & P_{y_0} & P_{\theta_0} & P_{v_1} & P_{v_2} \end{bmatrix}^T \tag{3.30}$$

Therefore the momentum of the IC beam can be expressed by the following matrix equation:

$$\begin{bmatrix} P_{x_0} \\ P_{y_0} \\ P_{\theta_0} \\ P_{v_1} \\ P_{v_2} \end{bmatrix} = \begin{bmatrix} M & 0 & -\left(\bar{m}_{v,1}v_1 + \bar{m}_{v,2}v_2\right) & 0 & 0 \\ 0 & M & 0 & \bar{m}_{v,1} & \bar{m}_{v,2} \\ -\left(\bar{m}_{v,1}v_1 + \bar{m}_{v,2}v_2\right) & 0 & \left(J_0 + \bar{m}_{vv,1}v_1^2 + \bar{m}_{vv,2}v_2^2\right) & \bar{m}_{xv,1} & \bar{m}_{xv,2} \\ 0 & \bar{m}_{v,1} & \bar{m}_{xv,1} & \bar{m}_{vv,1} & 0 \\ 0 & \bar{m}_{v,2} & \bar{m}_{xv,2} & 0 & \bar{m}_{vv,2} \end{bmatrix} \begin{bmatrix} \dot{x}_0 \\ \dot{y}_0 \\ \dot{\theta}_0 \\ \dot{v}_1 \\ \dot{v}_2 \end{bmatrix} \qquad \textbf{(3.31)}$$

The velocities can then be calculated by the product of the momentum and the inverse of the square matrix.

Representing this in matrix form,

$$\dot{\vec{q}} = \vec{A}^{-1}\left(\vec{q}\right)\cdot\vec{P} \qquad \textbf{(3.32)}$$

The remaining terms necessary to establish the IC-field representations:

$$\begin{aligned} e'_{x_0} &= M\dot{y}_0\dot{\theta}_0 + \left(\bar{m}_{v,1}\dot{v}_1 + \bar{m}_{v,2}\dot{v}_2\right)\dot{\theta}_0 \\ e'_{y_0} &= -M\dot{x}_0\dot{\theta}_0 + \left(\bar{m}_{v,1}v_1 + \bar{m}_{v,2}v_2\right)\dot{\theta}_0^2 \\ e'_{\theta} &= 0 \\ e'_{v_j} &= -\bar{m}_{v,j}\dot{x}_0\dot{\theta}_0 + \bar{m}_{vv,j}v_j\dot{\theta}_0^2 - \bar{k}_{v,j}v_j \qquad ; j = 1,2 \end{aligned} \qquad \textbf{(3.33)}$$

Notice that the elastic deformations are nonlinearly coupled to the rigid body motions in both equations (3.31) and (3.33).

From equation (3.25),

$$\begin{aligned} \dot{P}_{x_0} &= F_{x_0} + e'_{x_0} \\ \dot{P}_{y_0} &= F_{y_0} + e'_{y_0} \\ \dot{P}_{\theta_0} &= F_{\theta_0} + e'_{\theta_0} \\ \dot{P}_{v_j} &= F_{v_j} + e'_{v_j} \qquad ; j = 1,2 \end{aligned} \qquad \textbf{(3.34)}$$

This can be re-written in matrix form:

$$\dot{\vec{P}} = \vec{F} + \vec{e}'\left(\vec{q},\dot{\vec{q}}\right) \qquad \textbf{(3.35)}$$

At this point, it is mentioned again that the state variables for the IC beam are displacements and momentums. Therefore equations (3.32) and (3.35) are the two sets of equations required to describe the IC beam. Writing them together here:

$$\begin{aligned}\dot{\vec{q}} &= \vec{A}^{-1}\left(\vec{q}\right)\cdot\vec{P} \\ \dot{\vec{P}} &= \vec{F} + \vec{e}'\left(\vec{q},\dot{\vec{q}}\right)\end{aligned} \qquad \textbf{(3.36)}$$

Equation (3.36) represents the final complete set of nonlinear coupled equations of the IC beam substructure. The elastic deformations terms are nonlinearly coupled to the rigid body motion terms, while the elastic deformations within the substructure are linear.

It is interesting to note that the time derivatives of the momentum depend on the velocities. This means that the velocities need to be computed first before the time derivatives of the momentum can be computed. This requirement will be highlighted further in subsection 4.2.2 where the solution process for the rotating beam problem is presented.

The resulting bond graph model representation of the IC beam is illustrated in Figure 3.

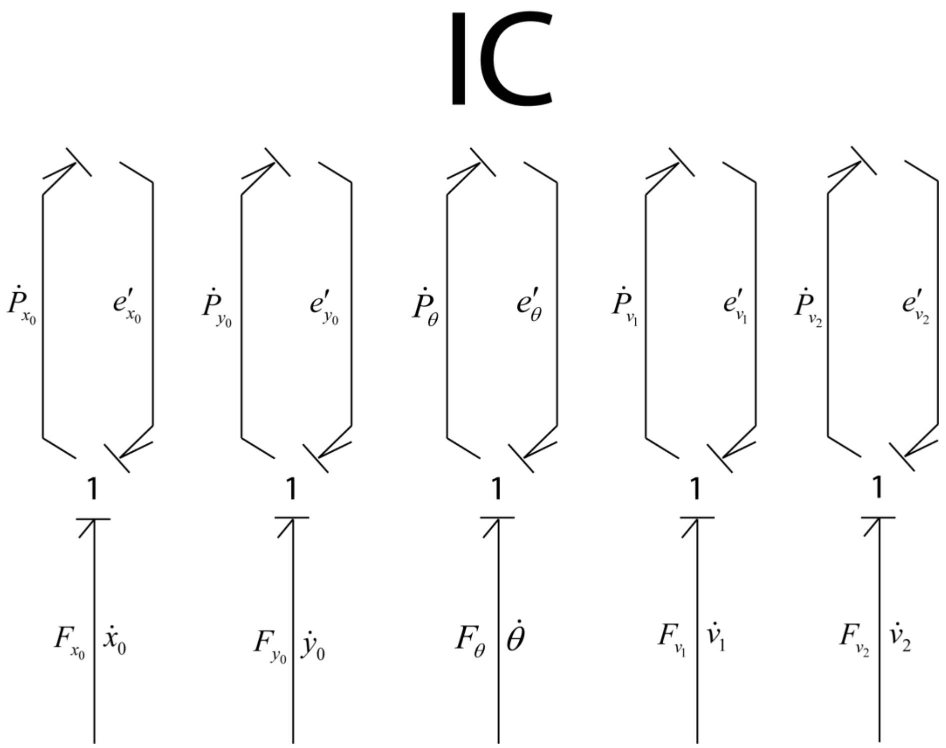

Figure 3: Bond Graph Model of the IC Beam with Two Elastic Modes

3.3. Structural Damping

Structural damping of the IC beam can be included in the form of modal damping. In modal damping, the modal damping coefficient is related to the modal damping ratio, modal stiffness and modal mass by the following formula:

$$\bar{c}_j = 2\zeta_j \sqrt{\bar{k}_{v,j}\bar{m}_{vv,j}} \qquad ; j = 1,2 \tag{3.37}$$

The modal damping force for mode *j* is then given by:

$$F_{damping,j} = -\bar{c}_j \dot{v}_j \qquad ; j = 1,2 \tag{3.38}$$

The modal damping force is implemented as a modification in the fourth line of equation (3.33):

$$e'_{v_j} = -\bar{m}_{v,j}\dot{x}_0\dot{\theta}_0 + \bar{m}_{vv,j}v_j\dot{\theta}_0^2 - \bar{k}_{v,j}v_j - \bar{c}_j\dot{v}_j \qquad ; j = 1,2 \tag{3.39}$$

The effect of modal damping on the solution of the IC beam in the rotating beam problem will be investigated and discussed in greater detail in subsection 7.8.

3.4. Difficulties in Introducing Conventional Modal Acceleration

The conventional modal acceleration discussed in subsection 2.6 gives rise to numerical difficulties in the equation system even though it can be easily introduced in the IC beam formulations. Instead, modal acceleration will be performed by decoupling a portion of the highest modes away from the rigid body motions. This will be presented in subsection 3.5. In this subsection, the modification to the IC beam formulation using conventional modal acceleration will be presented and the corresponding numerical difficulties discussed.

In conventional modal acceleration, the static responses of truncated modes are considered in the total response instead of being totally eliminated. These modes are termed here as ‘static correction modes’. In order to add additional static correction modes in the IC beam, additional generalized variables need to be defined; one additional variable for each additional mode.

The modification of the IC beam from subsection 3.2 to include one additional static correction mode is illustrated here. It is straight forward to further extend this to include more static correction modes. The additional static correction mode, i.e. mode 3, has no dynamics and thus does not have any kinetic energy and momentum.

$$\begin{aligned} P_{v_3} &= 0 \\ \dot{P}_{v_3} &= 0 \end{aligned} \tag{3.40}$$

The first line in equation (3.36) remains unmodified and stays as a 5 by 5 matrix system. Therefore the computational effort required to do the matrix inversions stay the same. The second line of the equation needs to be modified to incorporate the generalized variable for the additional static correction mode. From the expansion of the second line in equation (3.36), the corresponding equation for mode 3 would be:

$$\dot{P}_{v_3} = 0 = F_{v_3} + e'_{v_3} \tag{3.41}$$

And using the fourth line of equation (3.33) in equation (3.41),

$$F_{v_3} - \overline{m}_{v,3}\dot{x}_0\dot{\theta}_0 + \overline{m}_{vv,3}v_3\dot{\theta}_0^2 - \overline{k}_{v,3}v_3 = 0 \tag{3.42}$$

Re-writing equation (3.42),

$$v_3 = \frac{\overline{m}_{v,3}\dot{x}_0\dot{\theta}_0 - F_{v_3}}{\overline{m}_{vv,3}\dot{\theta}_0^2 - \overline{k}_{v,3}} \tag{3.43}$$

The velocity output will be:

$$\dot{v}_3 = \frac{d}{dt}\left(\frac{\overline{m}_{v,3}\dot{x}_0\dot{\theta}_0 - F_{v_3}}{\overline{m}_{vv,3}\dot{\theta}_0^2 - \overline{k}_{v,3}}\right) \tag{3.44}$$

The resulting bond graph model is presented in Figure 4.

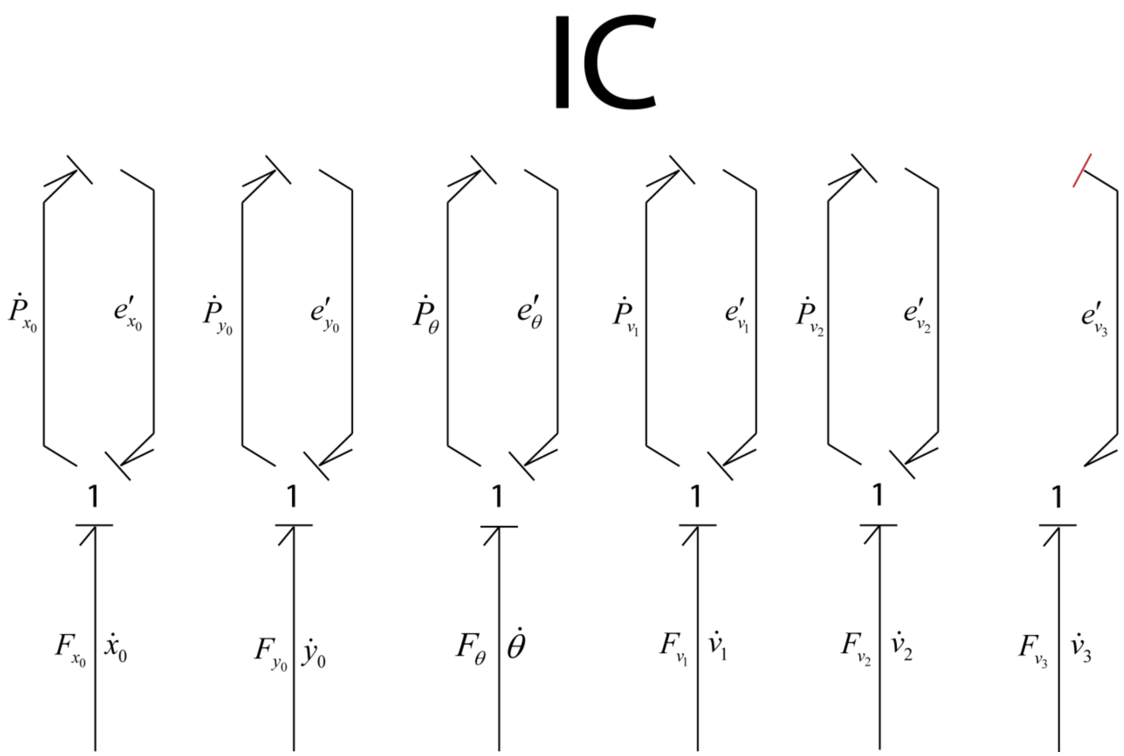

Figure 4: Bond Graph Model of IC Beam with Two Elastic Modes and One Static Correction Mode

From equation (3.43), it is observed that the solution of the response for mode 3 is a direct algebraic representation of the rigid body velocities and its generalized force. Therefore, the response at a time step is calculated based on the velocities and its generalized force at the same time step. It might seem that this is extremely simple to solve for. However, notice the differential causality assignment (denoted as a red line) at the last port corresponding to mode 3 at the IC element in Figure 4. The output of this port is the generalized velocity of mode 3 which is calculated by equation (3.44), i.e. derivative of some variables. This means that conventional modal acceleration introduces differential causality into the system. Differential causalities give rise to inefficient numerical systems. This is especially true for nonlinear models such as the IC beam. The approach in this thesis is to keep the models in complete integral causality for efficient numerical systems. Therefore, the conventional modal acceleration method will not be applied in the IC beam formulation.

3.5. Modal Acceleration by Decoupling Modes

As discussed in subsection 3.4, conventional modal acceleration results in numerical difficulties. Instead, modal acceleration will be introduced in the IC beam by decoupling a portion of the highest modes away from the rigid body motions. The assumption is that the highest modes do not transfer significant amounts of energy between the rigid body motions. Complete integral causality will still be maintained. An example of an IC beam with two fully coupled modes and one decoupled mode will be illustrated here.

Consider the expansion of equation (3.31) for the addition of one decoupled mode:

$$\begin{bmatrix} P_{x_0} \\ P_{y_0} \\ P_{\theta_0} \\ P_{v_1} \\ P_{v_2} \end{bmatrix} = \begin{bmatrix} M & 0 & -\left(\bar{m}_{v,1}v_1 + \bar{m}_{v,2}v_2\right) & 0 & 0 \\ 0 & M & 0 & \bar{m}_{v,1} & \bar{m}_{v,2} \\ -\left(\bar{m}_{v,1}v_1 + \bar{m}_{v,2}v_2\right) & 0 & \left(J_0 + \bar{m}_{vv,1}v_1^2 + \bar{m}_{vv,2}v_2^2\right) & \bar{m}_{xv,1} & \bar{m}_{xv,2} \\ 0 & \bar{m}_{v,1} & \bar{m}_{xv,1} & \bar{m}_{vv,1} & 0 \\ 0 & \bar{m}_{v,2} & \bar{m}_{xv,2} & 0 & \bar{m}_{vv,2} \end{bmatrix} \begin{bmatrix} \dot{x}_0 \\ \dot{y}_0 \\ \dot{\theta}_0 \\ \dot{v}_1 \\ \dot{v}_2 \end{bmatrix} \qquad \textbf{(3.45)}$$

$$P_{v_3} = \bar{m}_{vv,3}\dot{v}_3$$

Observe that the third generalized mode velocity is decoupled from the rigid body momentums. Also the size of the square matrix remains the same. Therefore, the computational efforts required to perform the matrix inversions stay the same. This is the computational savings of the modal acceleration method presented herein.

The remaining modifications are to equation (3.33) where the contributions from the rigid body motions to the third mode's generalized force are removed:

$$\begin{aligned} e'_{x_0} &= M\dot{y}_0\dot{\theta}_0 + \left(\bar{m}_{v,1}\dot{v}_1 + \bar{m}_{v,2}\dot{v}_2\right)\dot{\theta}_0 \\ e'_{y_0} &= -M\dot{x}_0\dot{\theta}_0 + \left(\bar{m}_{v,1}\dot{v}_1^2 + \bar{m}_{v,2}\dot{v}_2^2\right)\dot{\theta}_0^2 \\ e'_{\theta} &= 0 \\ e'_{v_j} &= -\bar{m}_{v,j}\dot{x}_0\dot{\theta}_0 + \bar{m}_{vv,j}v_j\dot{\theta}_0^2 - \bar{k}_{v,j}v_j \qquad ; j = 1,2 \\ e'_{v_3} &= -\bar{k}_{v,3}v_3 \end{aligned} \qquad \textbf{(3.46)}$$

The structure of the bond graph model for the resulting IC beam will remain the same as in Figure 3 with the exception of an additional mode, i.e. mode 3.

This modal acceleration method will be applied and investigated in greater detail for the rotating beam problem in subsection 7.9.

4. Models for Numerical Tests

4.1. Problem Description

The rotating beam problem as described in Wu and Haug [25] will be used here for numerical tests of the IC beam substructure. This is a beam that is fixed onto a rotating rigid shaft. This is illustrated in Figure 5. The beam properties are listed in Table 3.

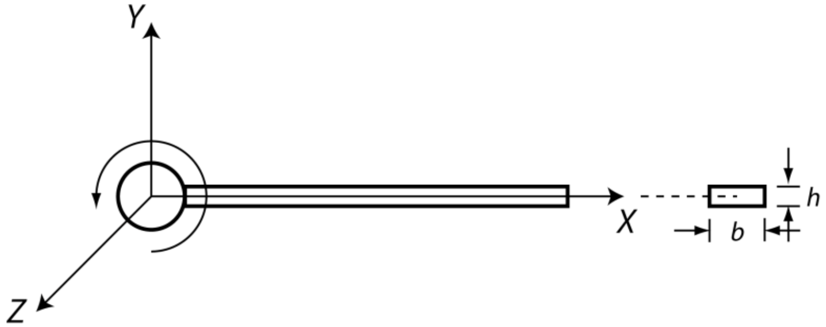

Figure 5: The Rotating Beam Problem

Table 3: Rotating Beam Properties

Length	8.0 m
Material density	2766.67 kg/m^3
Material elastic modulus	68.95 MPa
Width, b	0.03675m
Height, h	0.001986m

The rigid shaft is given an angular displacement *θ* about the *z*-axis which is defined as:

$$\theta = \begin{cases} \dfrac{\omega_s}{T_s}\left[\dfrac{1}{2}t^2 + \left(\dfrac{T_s}{2\pi}\right)^2 \left(\cos\left(\dfrac{2\pi t}{T_s}\right) - 1\right)\right] & , t < T_s \\ \omega_s \left(t - \dfrac{T_s}{2}\right) & , t \geq T_s \end{cases} \tag{4.1}$$

The rotating beam problem is chosen as a basis for numerical tests of the IC beam as the ultimate purpose of the IC beam is to model wind turbine rotor blades, which by themselves are non-uniform rotating beams.

4.2. Bond Graph Models for Numerical Tests

4.2.1. Bond Graph Component Models Required

The schematic of the rotating beam problem as would be solved by a two substructure IC beam model is presented in Figure 6. Note that multi substructures IC beam models are capable of modeling geometric nonlinearity. On the other hand, single substructure IC beam models are inherently geometrically linear models.

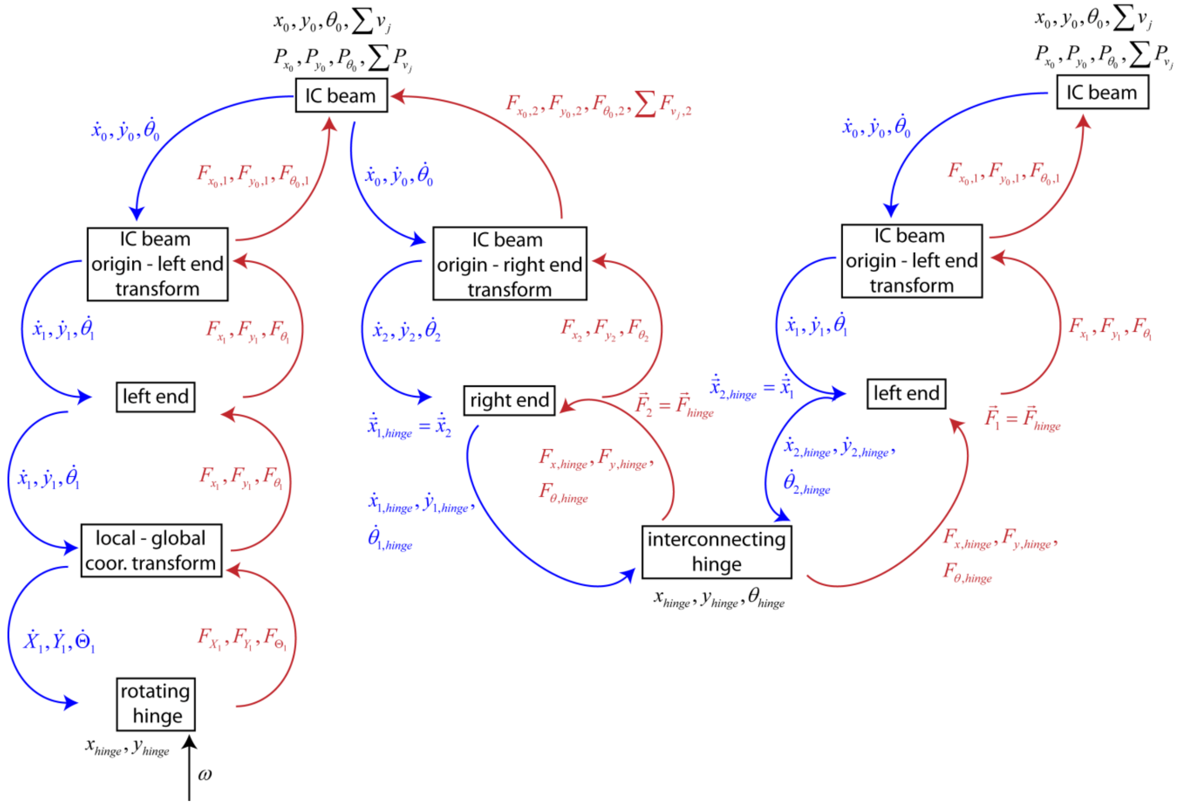

Figure 6: Schematic of the Rotating Beam Bond Graph Model

Four types of component models, namely, IC beam, coordinate transformation, rotating hinge and interconnecting hinge, are required to model the rotating beam problem. They will be presented individually in subsections 4.2.1.1 to 0. These are illustrated in Figure 6 as boxes with the corresponding component model names. The flow of the power variables, i.e. velocities and forces are also presented in the figure. The output paths and variables are denoted in blue, while the input paths and variables are denoted in red. These paths illustrate the variables flow between the individual component models in the solution process. The solution process will be presented in subsection 4.2.2. The state variables are denoted in black and written next to the models that possess them, i.e. IC beam and hinges. The input into the system, i.e. the prescribed rotational velocity, is directed into the rotating hinge component model.

4.2.1.1. IC Beam Model

The IC beam model was presented in section 3. The bond graph model where two elastic modes were considered was presented in Figure 3. It is straight forward to further extend this model to include additional elastic modes. One additional mode being considered would mean an extra generalized variable in the equation system. The mode shapes used for most of the numerical tests performed in this thesis are the fixed-free mode shapes; fixed on the left end and free on the right end. It is obvious that fixed-fixed mode shapes are the best choice here. Other types of mode shapes, for example the free-free mode shapes can be used. However, as will be shown in the static analysis results of the tip load on a cantilevered beam presented in subsection 5.1, the free-free mode shapes will lead to slow modal convergence.

Note that the IC beam formulation, given in equation (3.36), accepts forces as inputs and provides velocities as outputs. This presents modeling difficulties when using the IC beam for the rotating beam problem, for example, the input into the system is prescribed rotational velocity of the beam. This difficulty can be overcome by passing the prescribed velocity through a rotational damper/spring that in turn provides the necessary force as input into the IC beam. This will be further discussed in subsection 4.2.1.3. Note that in principle, it is possible to force the IC beam to accept velocities as inputs. However, this will lead to differential causalities and results in an inefficient numerical system.

4.2.1.2. Coordinate Transformations Models

There are two types of coordinate transformation models required for the rotating beam problem. The first is the transformation from the IC beam origin to the left or right end of the beam. The second is the transformation of local coordinates at the left end of the first substructure to the global coordinate system.

Transformation from IC Beam Origin to Left or Right End

The transformations of the IC beam with fixed-free modes will be presented as these are the modes mostly applied in this thesis. This means that the transformations to the left and right end are different. There are no power connections at the left end to the elastic modes as deflections and slopes of the mode shapes at this end is zero.

The bond graph model of the transformations to the left end and its corresponding equations are presented in Figure 7 and equations (4.2) and (4.3) respectively. And, the bond graph model and equations of the transformation to the right end are presented in Figure 8 and equations (4.4) and (4.5) respectively. For ease of presentation, this bond graph model will only use one elastic mode. Once again, it is straight forward to further extend the models to add more modes.

It is to be noted that, the subscripts ‘0’, ‘1’, and ‘2’ denote the IC beam origin, the left and right ends respectively.

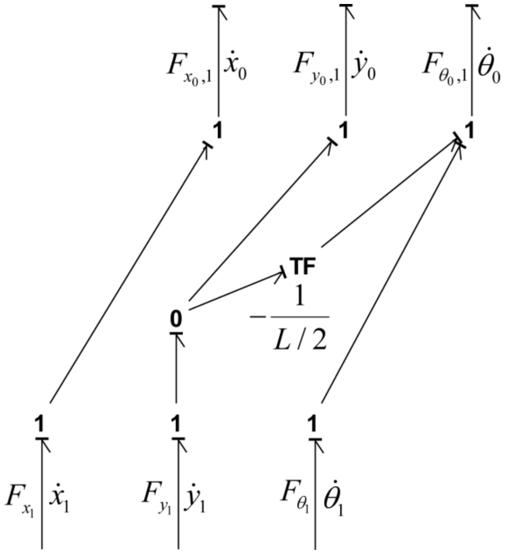

Figure 7: Bond Graph Model of the Coordinate Transformation from the IC Beam Origin to the Left End

$$\begin{aligned} \dot{x}_1 &= \dot{x}_0 \\ \dot{y}_1 &= \dot{y}_0 - \frac{L}{2}\dot{\theta}_0 \\ \dot{\theta}_1 &= \dot{\theta}_0 \end{aligned} \tag{4.2}$$

$$\begin{aligned} F_{x_0,1} &= F_{x_1} \\ F_{y_0,1} &= F_{y_1} \\ F_{\theta_0,1} &= F_{\theta_1} - \frac{L}{2}F_{y_1} \end{aligned} \tag{4.3}$$

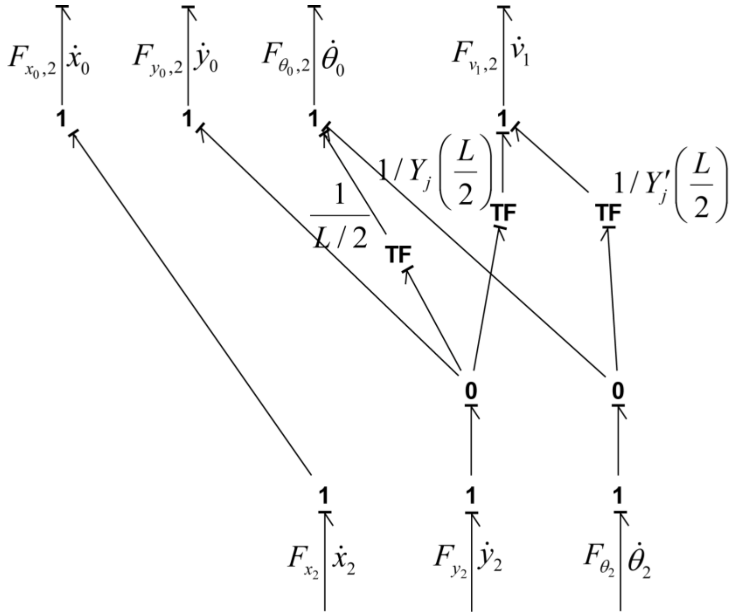

Figure 8: Bond Graph Model of the Coordinate Transformation from the IC Beam Origin to the Right End

$$\begin{aligned} \dot{x}_2 &= \dot{x}_0 \\ \dot{y}_2 &= \dot{y}_0 + \frac{L}{2}\dot{\theta}_0 + \sum_{j=1}^{N} Y_j\left(\frac{L}{2}\right)\dot{v}_j \\ \dot{\theta}_2 &= \dot{\theta}_0 + \sum_{j=1}^{N} Y_j'\left(\frac{L}{2}\right)\dot{v}_j \end{aligned} \tag{4.4}$$

$$\begin{aligned} F_{x_0,2} &= F_{x_2} \\ F_{y_0,2} &= F_{y_2} \\ F_{\theta_0,2} &= F_{\theta_2} + \frac{L}{2}F_{y_2} \\ F_{v_j,2} &= Y_j\left(\frac{L}{2}\right)F_{y_2} + Y_j'\left(\frac{L}{2}\right)F_{\theta_2} \qquad , j = 1,\ldots,N \end{aligned} \tag{4.5}$$

The total forces to the IC beam will then be the sum of forces at the IC beam origin equations transformed from both the left and right ends.

$$\begin{aligned} F_{x_0} &= F_{x_0,1} + F_{x_0,2} \\ F_{y_0} &= F_{y_0,1} + F_{y_0,2} \\ F_{\theta_0} &= F_{\theta_1,1} + F_{\theta_1,2} \\ F_{v_j} &= F_{v_j,2} \qquad , j = 1, \ldots, N \end{aligned} \tag{4.6}$$

Transformation from Local Coordinates of Left End of First Substructure to Global Coordinate System

The rotating hinge model is formulated in the global coordinate system; therefore a coordinate transformation from local to global coordinates of the left end of the first substructure (where the rotating hinge is located) is required. The bond graph model of this transformation is presented in Figure 9. The corresponding equations are presented in equation (4.7). Note that small letters represent local coordinates and large letters represent global coordinates. Also, the subscript '1' represents the left end of the substructure.

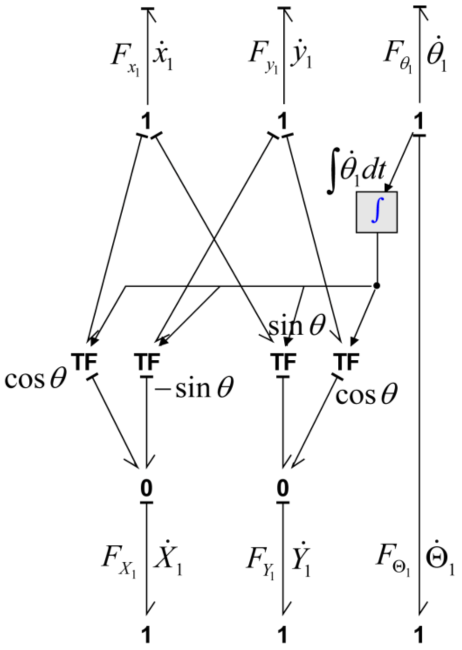

Figure 9: Bond Graph Model of the Coordinate Transformation of Left End of First Substructure to Global Coordinate System

$$\begin{bmatrix} \dot{X}_1 \\ \dot{Y}_1 \\ \dot{\Theta}_1 \end{bmatrix} = \begin{bmatrix} \cos\theta & -\sin\theta & 0 \\ \sin\theta & \cos\theta & 0 \\ 0 & 0 & 1 \end{bmatrix} \begin{bmatrix} \dot{x}_1 \\ \dot{y}_1 \\ \dot{\theta}_1 \end{bmatrix} \tag{4.7}$$

$$\begin{bmatrix} F_{x_1} \\ F_{y_1} \\ F_{\theta_1} \end{bmatrix} = \begin{bmatrix} \cos\theta & -\sin\theta & 0 \\ \sin\theta & \cos\theta & 0 \\ 0 & 0 & 1 \end{bmatrix}^T \begin{bmatrix} F_{X_1} \\ F_{Y_1} \\ F_{\Theta_1} \end{bmatrix}$$

4.2.1.3. Rotating Hinge Model

The bond graph model and its corresponding equations of the rotating hinge are presented in Figure 10 and equation (4.8) respectively. This model is formulated in the global coordinate system.

It was mentioned in subsection 4.2.1.1 that the IC beam model accepts forces as inputs and provides velocities as outputs. However, the input to the rotating beam problem is prescribed rotational velocity. Therefore, a resistor element (damper) is placed together with the flow source (prescribed rotational velocity) at a zero junction. This resistor accepts the difference between the actual and prescribed rotational velocity at the rotating hinge as input and provides a torque as output. This output torque is then used as input for the IC beam. The resistance of the resistor must be large to minimize the energy flow into it. An alternative way to argue is that the resistance value must be large to ensure a small difference between the actual and prescribed rotational velocity. This introduces a very small error as energy flowing into the resistor will be dissipated.

Direct connection of the left end of the beam to the ground will introduce differential causalities into the system. Therefore, springs are used for this connection. This is also known as the Karnopp-Margolis method [1]. These springs accept velocities as inputs and provide forces as outputs. These outputs are the inputs to the IC beam. Introducing springs will add additional state variables which are the displacements of the springs. The stiffness of these springs must be large to ensure negligible relative motions between the left end of the beam and the ground.

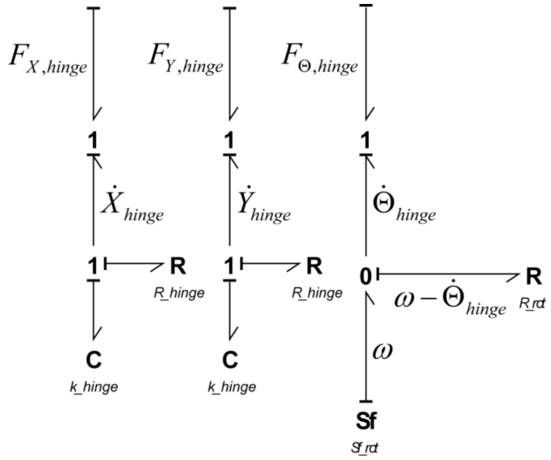

Figure 10: Bond Graph Model of the Rotating Hinge

The equations for the forces calculated by the rotating hinge model are:

$$\begin{aligned} F_{X,hinge} &= -\left(k_{hinge}X_{hinge} + R_{hinge}\dot{X}_{hinge}\right) \\ F_{Y,hinge} &= -\left(k_{hinge}Y_{hinge} + R_{hinge}\dot{Y}_{hinge}\right) \\ F_{\Theta,hinge} &= R_{rot}\left(\omega - \dot{\Theta}_{hinge}\right) \end{aligned} \tag{4.8}$$

4.2.1.4. Interconnecting Hinge Model

The bond graph model and its corresponding equations of the interconnecting hinge are presented in Figure 11 and equations (4.9) and (4.10) respectively. This model is formulated in the local IC beam coordinate system.

To ensure complete integral causality, springs are used to interconnect the IC beam substructures, i.e. the Karnopp-Margolis method [1]. The interconnecting hinge model accepts velocities as inputs and provides forces as outputs. The relative displacements between the two interconnected IC beam substructures are the state variables. Once again, the stiffness values must be large to ensure negligible relative displacements between the two interconnected IC beam substructures. Note that subscripts ‘1’ and ‘2’ denote the velocities at the left and right sides of the hinge respectively. The left side of the hinge is connected to the right end of the previous IC beam substructure and the right side of the hinge is connected to the left end of the next adjacent IC beam substructure.

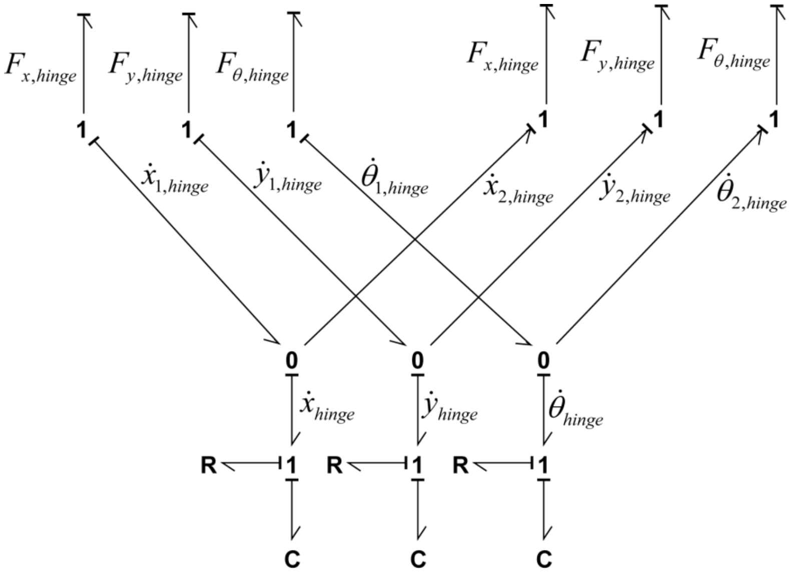

Figure 11: Bond Graph Model of Interconnecting Hinge

$$\begin{aligned} F_{x,hinge} &= -\left(k_{hinge} x_{hinge} + R_{hinge} \dot{x}_{hinge}\right) \\ F_{y,hinge} &= -\left(k_{hinge} y_{hinge} + R_{hinge} \dot{y}_{hinge}\right) \\ F_{\theta,hinge} &= -\left(k_{hinge} \theta_{hinge} + R_{hinge} \dot{\theta}_{hinge}\right) \end{aligned} \quad \textbf{(4.9)}$$

$$\begin{aligned} \dot{x}_{hinge} &= \dot{x}_{1,hinge} - \dot{x}_{2,hinge} \\ \dot{y}_{hinge} &= \dot{y}_{1,hinge} - \dot{y}_{2,hinge} \\ \dot{\theta}_{hinge} &= \dot{\theta}_{1,hinge} - \dot{\theta}_{2,hinge} \end{aligned} \quad \textbf{(4.10)}$$

4.2.2. Solution Process

The equation system, equation (4.11), consists of three sets of first order nonlinear ordinary differential equations that must be solved together.

$$\begin{aligned} \dot{\vec{q}} &= \vec{A}^{-1}\left(\vec{q}\right)\vec{P} \\ \dot{\vec{x}}_{hinge} &= \varphi\left(\vec{q}, \dot{\vec{q}}\right) \\ \dot{\vec{P}} &= \vec{F}\left(\omega, \vec{x}_{hinge}, \dot{\vec{x}}_{hinge}\right) + \vec{e}'\left(\vec{q}, \dot{\vec{q}}\right) \end{aligned} \quad \textbf{(4.11)}$$

The first line in equation (4.11) is the equation for the velocities of all IC beams. The second line is the equation for the velocities at all hinges. It is the various coordinate transformations presented in subsection 4.2.1.2. Also, it requires the velocities calculated from the first line as inputs. The third line is the equation for the time derivatives of momentum of all IC beams. It requires velocities calculated from both the first and second lines as inputs. Note that the first and the third lines were also presented in subsection 3.2.

The process of calculating the time derivatives is:

i. Calculate the velocities at the IC beams using the first line.
ii. Transform velocities at IC beams to the corresponding velocities at the hinges using the second line.
iii. Calculate forces at the hinges.
iv. Transform the forces at the hinges to the corresponding forces at the IC beams.
v. Calculate the time derivatives of the momentum at the IC beams using the third line.

Equation (4.11) is programmed into Matlab and solved using the ODE15s function. This is an implicit variable order solver based on the numerical differential formulas (NDFs) [43], [44]. The reason for choosing an integration method based on NDFs is that the numerical system is stiff and thus difficult to integrate using explicit integrators such as the Runga-Kutta methods. The experience using explicit methods on the IC beam model has revealed that the numerical system will break down unless extremely small step sizes in the order of 1e-8 were specified.

5. Static Deflection of Cantilevered Beam

In this section, static analysis of the rotating beam described in subsection 4.1 will be performed. The beam will be cantilevered at one end. The modal parameters used in this section are calculated from an eigenvalue analysis of a finite element model of the IC beam substructure using 20 planar two-node linear beam elements. There is one lateral and one rotational degree of freedom at each node. This means that there is a total of 40 eigenmodes calculated.

5.1. Linear Case – Small Deflection by a Tip Load

The cantilevered beam will be subjected to a 1 N tip load. This is a small load that results in a small displacement. A single IC beam substructure will be used to construct the beam model, i.e. the resulting beam model is geometrically linear. The analytical solution is:

$$v_{tip} = \frac{PL^3}{3EI} \tag{5.1}$$

Two different sets of mode shapes will be used: free-free and fixed-free. Obviously, since the beam is cantilevered, the optimum mode shapes will be the fixed-free ones. The purpose is to illustrate the importance of selecting the optimum mode shapes. The modal convergence of the tip deflection and slope are plotted in Figure 12 and Figure 13 respectively.

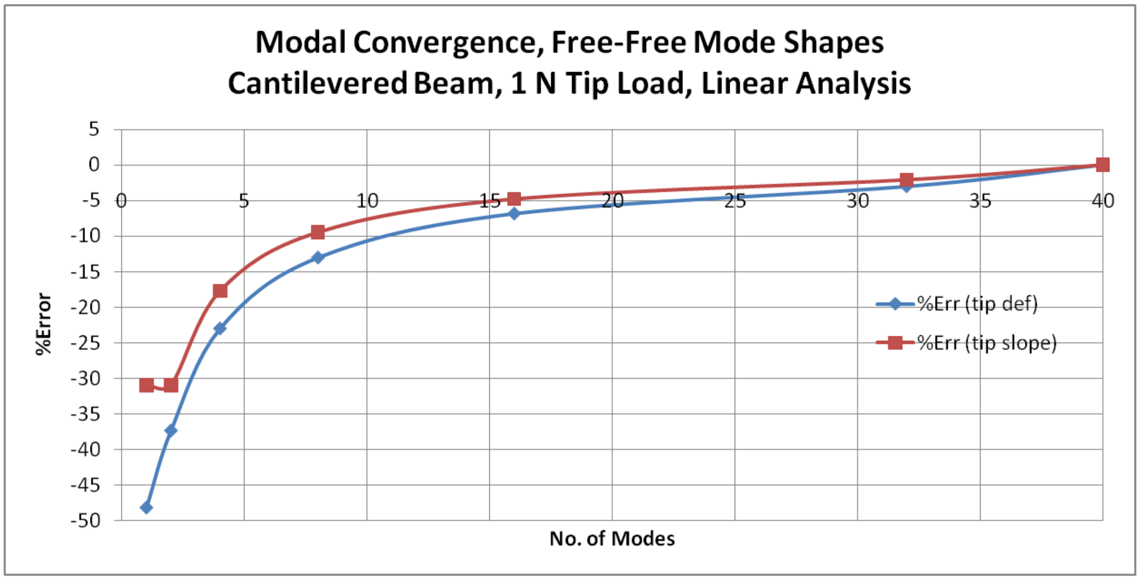

Figure 12: Modal Convergence, Free-Free Mode Shapes, Cantilevered Beam, 1 N Tip Load, Linear Analysis

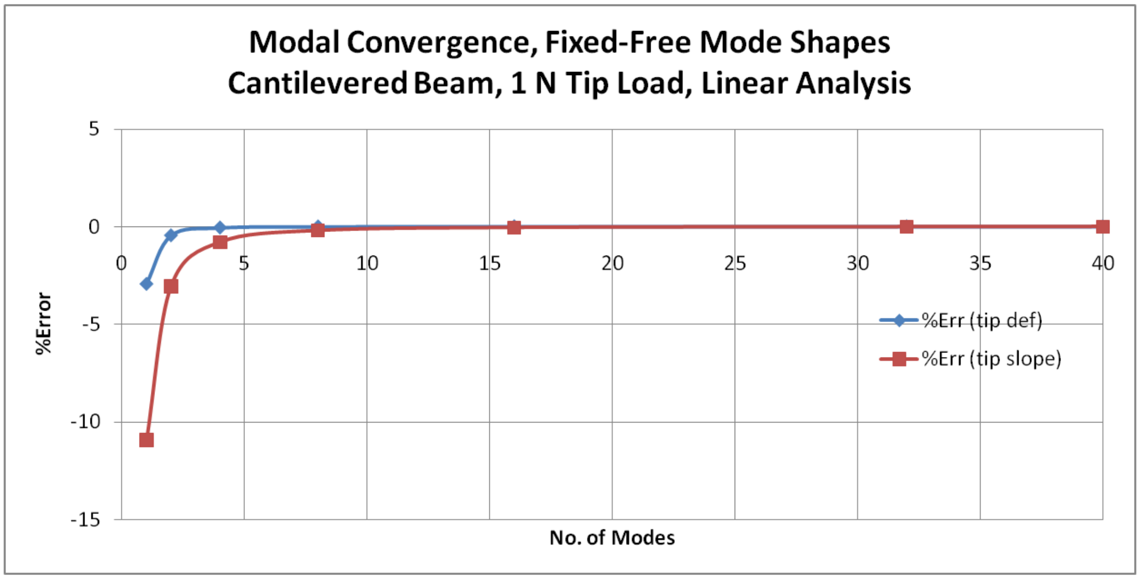

Figure 13: Modal Convergence, Fixed-Free Mode Shapes, Cantilevered Beam, 1 N Tip Load, Linear Analysis

The modal convergence of the free-free modes is significantly slower than the fixed-free modes. It is observed that just a couple of fixed-free modes will be sufficient to achieve errors below 5% while as many as 20 to 25 free-free modes are required to achieve similar accuracy. This highlights the importance of selecting the optimum mode shapes. Similarly, the bond graph model of the force-free beam described in section 10.2, Karnopp, Margolis and Rosenberg [29] and Margolis [37] will lead to slow modal convergence if one end of the beam is fixed.

It is also observed that the modal convergence of the tip slope for the fixed-free modes is slower than the modal convergence for the tip deflection. Accurate rotational displacement is important when multi substructures are used. This is because the tip slope of one substructure will affect the global tip deflection of the adjacent substructure that it connects to.

5.2. Nonlinear Cases

In this subsection, the multi IC beam substructures will be used for some nonlinear test cases. The purpose is to investigate the performance of the IC beam in solving geometric nonlinear problems.

5.2.1. Models Used

Five different models constructed using 2, 4, 8, 16 and 32 IC beam substructures respectively are used in this study. In addition, the number of modes was varied individually for each of these five models. The purpose is to observe the number of substructures and modes required to describe the various nonlinear problems. Fixed-free mode shapes are employed.

5.2.2. Nonlinear Case – Large Deflection by a Tip Moment

In this subsection, the beam is subjected to a tip moment of 100 Nm, large enough to result in a large deflection.

The analytical solution of the tip deflection of a linear cantilevered beam is given by:

$$v_{tip} = \frac{ML^2}{2EI} \tag{5.2}$$

The exact nonlinear solution is calculated via a nonlinear finite beam element model consisting of 20 linear beam elements in ABAQUS. The exact solutions of the tip deflection and slope of both the linear and nonlinear analysis are presented in Table 4.

Table 4: Exact Solutions of Cantilevered Beam Subjected to a Tip Moment of 100 Nm

	Linear	Nonlinear
Tip deflection (m)	5.650	4.772
Tip slope (rad)	1.412	1.412

Observe in Table 4 that the tip deflection calculated from linear analysis is significantly larger (about 18.4%) than the tip deflection calculated from nonlinear analysis. However, the calculated tip slopes are the same for both analyses. This is because the tip slope is a linear function of the concentrated tip moment. Figure 14 and Figure 15 plots the modal convergence of the tip deflection and slope respectively.

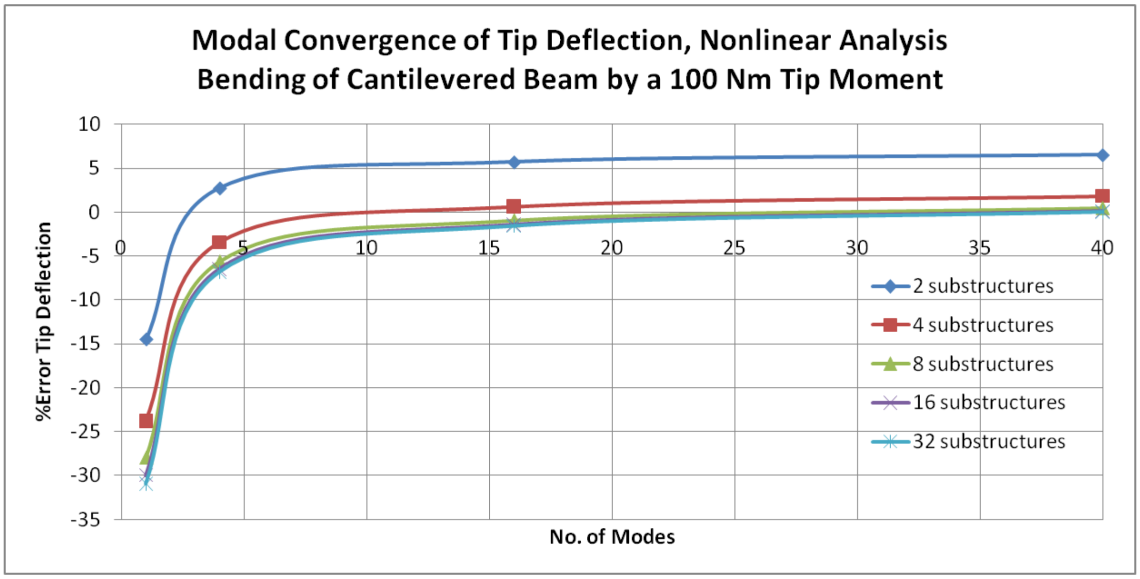

Figure 14: Modal Convergence of Tip Deflection, Nonlinear Analysis, Bending of Cantilevered Beam by a 100 Nm Tip Moment

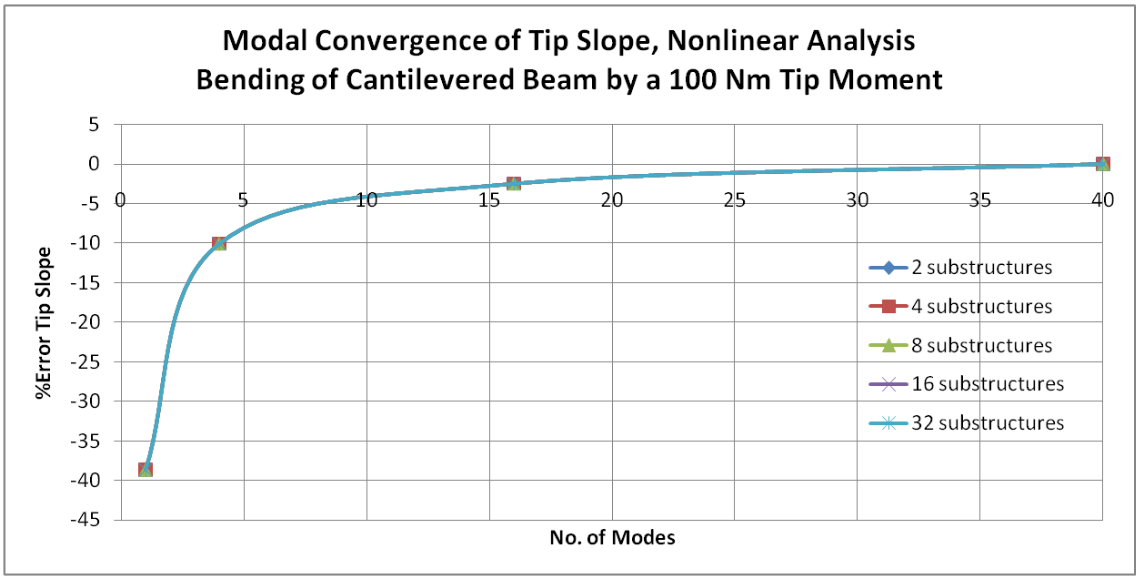

Figure 15: Modal Convergence of Tip Slope, Nonlinear Analysis, Bending of Cantilevered Beam by a 100 Nm Tip Moment

Prescribing too few substructures will result in the wrong converged solution. For example, in the two substructure case, the tip deflection converges to a value about 6-7% higher than the exact solution. Prescribing at least four substructures is sufficient to achieve less than 5% error. It is also observed that the modal convergence of the tip slope is not affected by the number of substructures prescribed. This is because the tip slope is a linear function of the concentrated tip moment.

It is important to prescribe a sufficient number of modes. Prescribing at least 5 modes achieves less than 5% and 10% errors for the tip deflection and slope respectively for all models with at least four substructures. Prescribing at least 10 modes achieves less than 5% errors for both tip deflection and slope for all models. Similar to subsection 5.1, the modal convergence of the tip slope is slower than the tip deflection.

Figure 16 and Figure 17 illustrate the deflection shapes of some of the models used.

The following notations are used:

- s – no. of substructures
- m – no. of modes

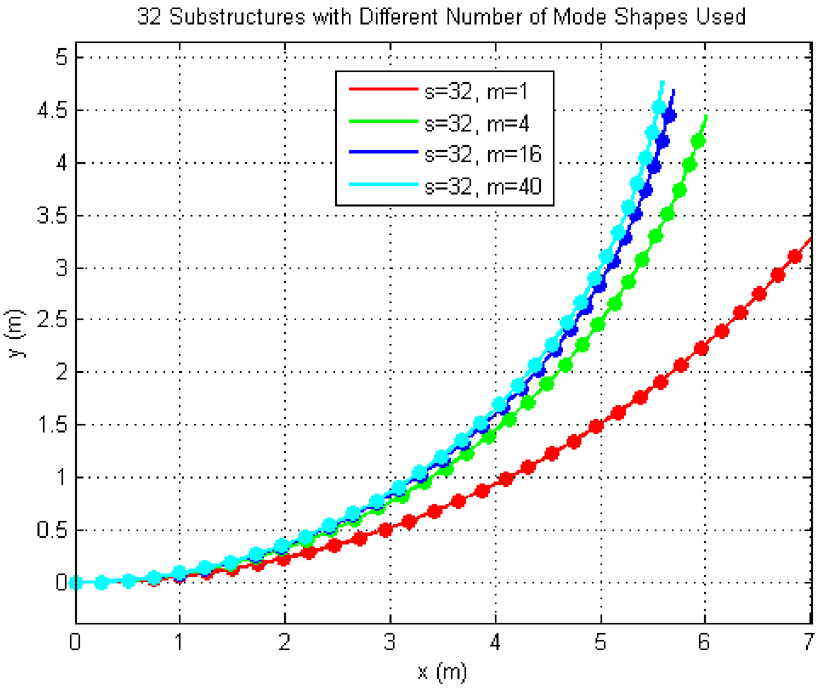

Figure 16: Bending of Cantilevered Beam by a 100 Nm Tip Moment, 32 Substructures with Different Number of Mode Shapes Used

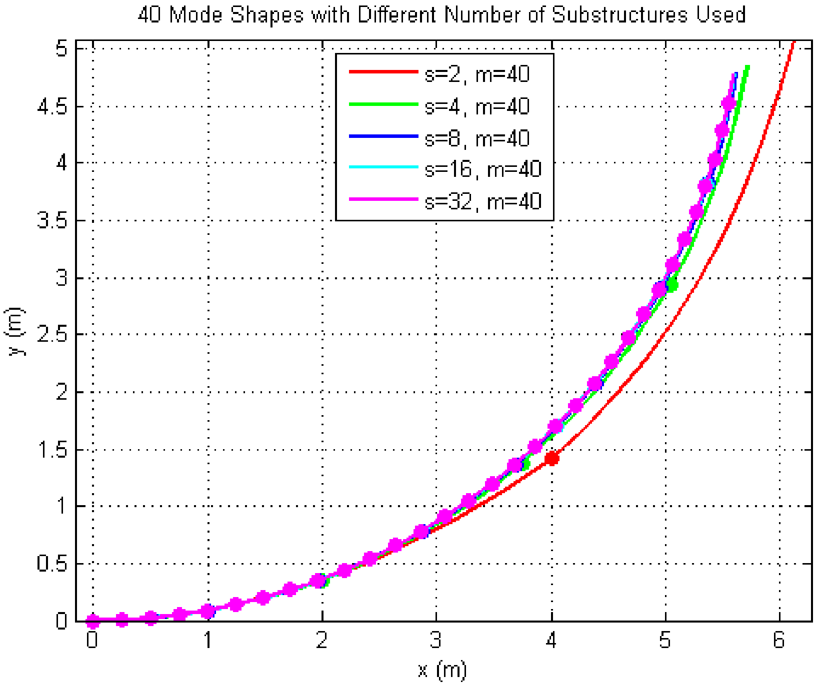

Figure 17: Bending of Cantilevered Beam by a 100 Nm Tip Moment, 40 Mode Shapes with Different Number of Substructures Used

5.3. Extremely Nonlinear Case – Bending of Cantilevered Beam into Complete Circle by a Tip Moment

In this subsection, the ability of the IC beam substructure to handle extreme geometric nonlinearity is investigated. The classical test case of bending the beam into a complete circle by a concentrated tip moment is used for this investigation.

The analytical solution

For a cantilevered beam with a uniform cross-section, flexural rigidity *EI* and length *L* subjected to a tip moment *M*, the Euler-Bernoulli beam theory [45] states that:

$$\frac{1}{R}=\frac{M}{EI} \tag{5.3}$$

Where *R* is the radius of the resulting circle due to the tip moment.

For bending into a complete circle, the radius *R* must be:

$$R=\frac{L}{2\pi} \tag{5.4}$$

Therefore, the tip moment required to bend the beam into a complete circle is:

$$M=\frac{2\pi EI}{L} \tag{5.5}$$

For the rotating beam described in subsection 4.1, this will correspond to a concentrated tip moment of 444.83 Nm.

Figure 18 to Figure 23 plot the deflection shapes of the various different models. The circular points represent the left end of each individual substructure. Figure 24 plots the modal convergences of the circular radius at the deflected state of the various models presented.

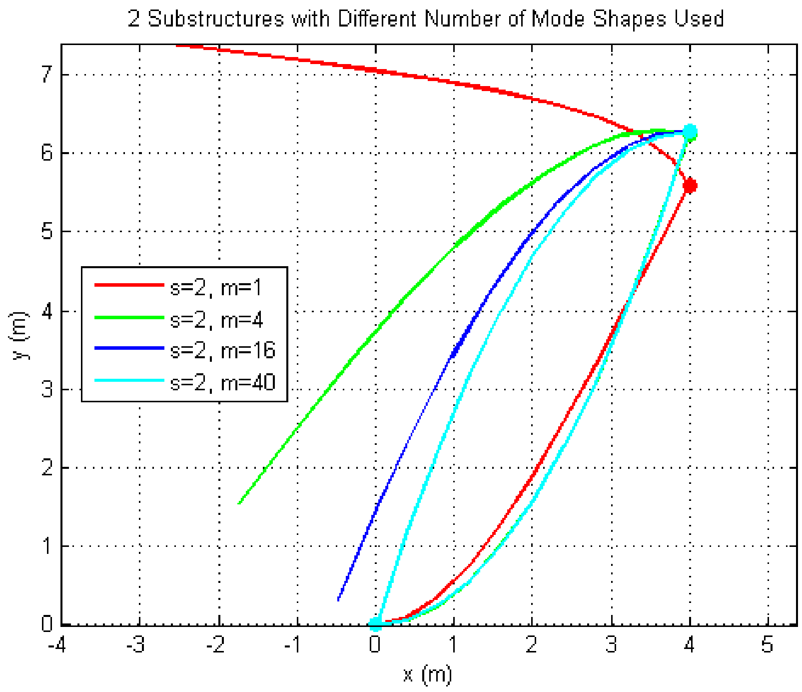

Figure 18: Bending of Cantilevered Beam into Complete Circle by a Tip Moment, 2 Substructures with Different Number of Mode Shapes Used

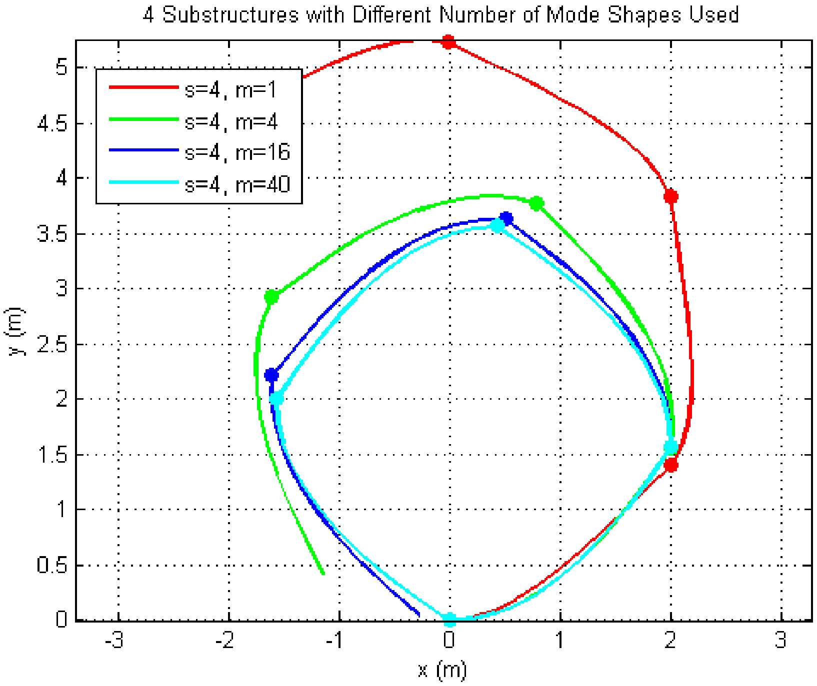

Figure 19: Bending of Cantilevered Beam into Complete Circle by a Tip Moment, 4 Substructures with Different Number of Mode Shapes Used

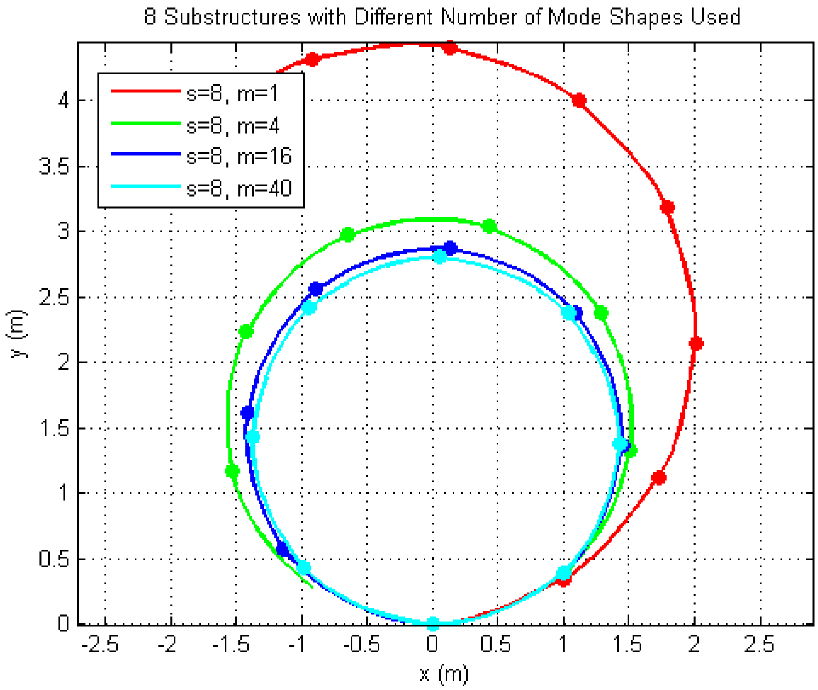

Figure 20: Bending of Cantilevered Beam into Complete Circle by a Tip Moment, 8 Substructures with Different Number of Mode Shapes Used

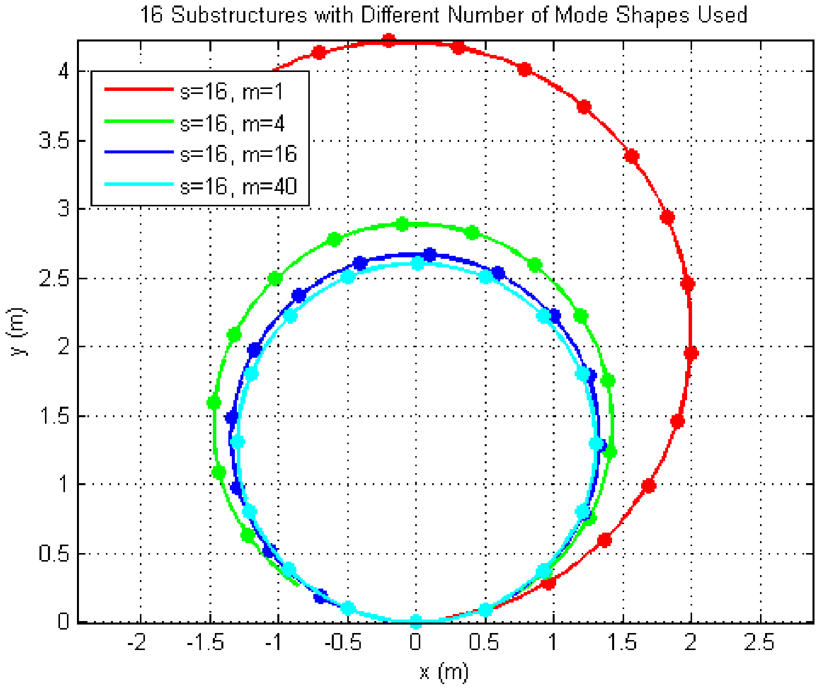

Figure 21: Bending of Cantilevered Beam into Complete Circle by a Tip Moment, 16 Substructures with Different Number of Mode Shapes Used

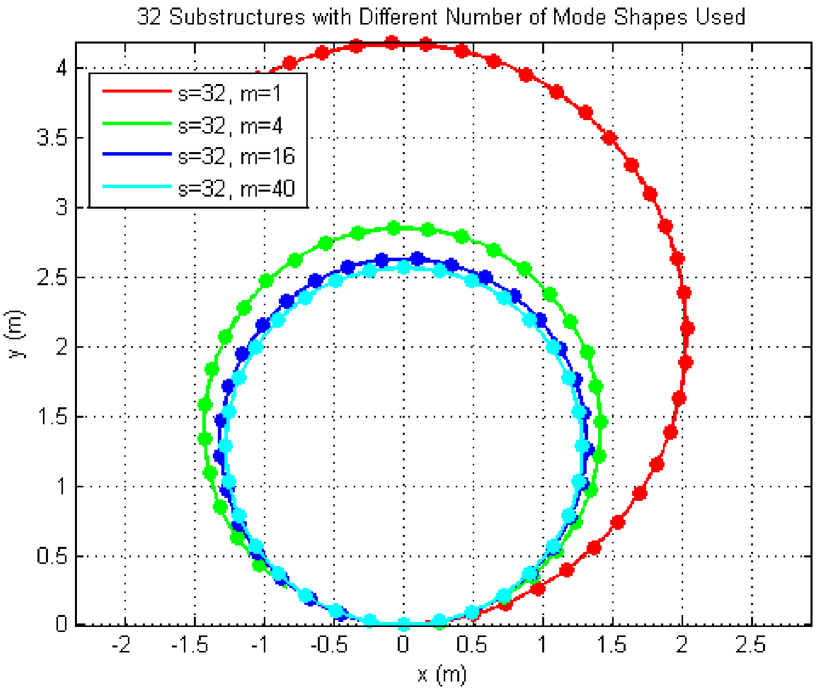

Figure 22: Bending of Cantilevered Beam into Complete Circle by a Tip Moment, 32 Substructures with Different Number of Mode Shapes Used

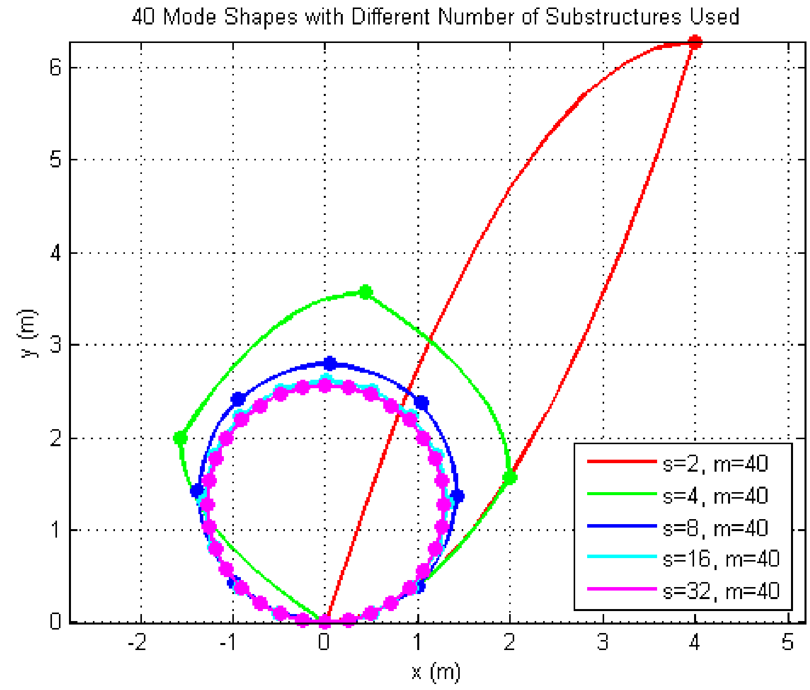

Figure 23: Bending of Cantilevered Beam into Complete Circle by a Tip Moment, 40 Mode Shapes with Different Number of Substructures Used

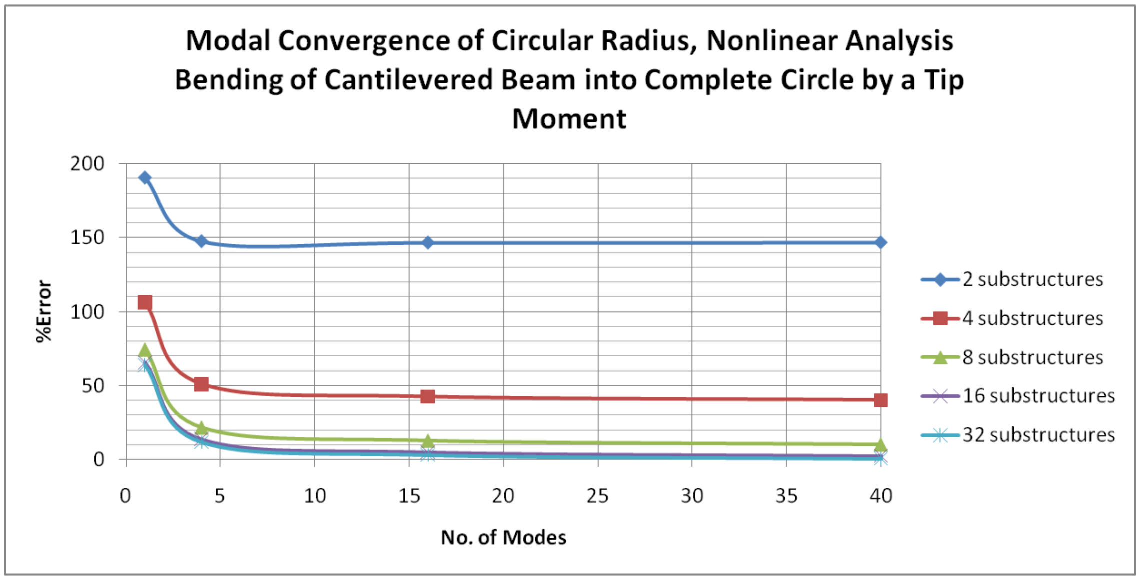

Figure 24: Modal Convergence of Circular Radius, Nonlinear Analysis, Bending of Cantilevered Beam into Complete Circle by Tip Moment

At least 8 substructures are needed to describe a circular deflected shape. Prescribing too little number of substructures will result in a noncircular deflected shape. This was observed for the models with 2 and 4 substructures (Figure 18, Figure 19 and Figure 23). It is further observed that in the modal convergence plot of the circular radius (Figure 24) that the results of 2 and 4 substructures will not converge even if all the modes i.e. all 40 modes were used.

The deflections also depend significantly on the number of modes used. Prescribing too little modes will result in a severe underestimation of the deflections. It is interesting to note that prescribing all the 40 modes will result in the tip of the beam returning to the origin, no matter how many substructures are used. The tip returning to the origin is the exact solution for this nonlinear bending problem. Prescribing lesser number of modes results in the tip going further away from the origin. When a sufficient number of substructures are already employed, insufficient number of modes will result in a larger circular radius. Also, the number of modes used does not significantly affect the deflected shape, i.e. prescribing insufficient number of modes will not cause the circle to be out of shape.

It is observed that prescribing at least 16 substructures with at least 5 modes will be sufficient to achieve less than 10% error in the circular radius. Increasing the number of modes to 10 further reduces the error to less than 5%.

THIS PAGE INTENTIONALLY LEFT BLANK.

6. Dynamic Analysis – Time Varying Point Excitation of Cantilevered Beam

In this section, the rigid body-elastic modes coupling feature of the IC beam will highlighted. This is illustrated using a cantilevered beam subjected to a unit time varying sinusoidal point excitation at its fixed end; refer to Figure 25.

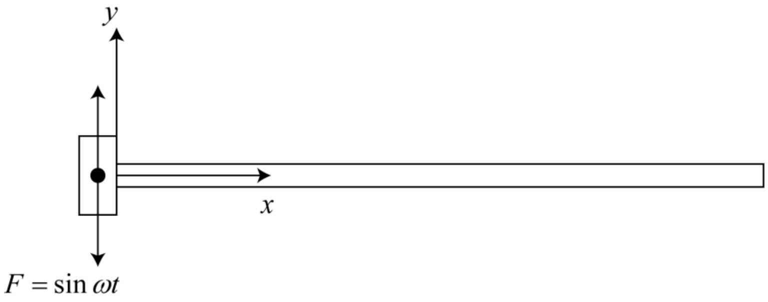

Figure 25: Cantilevered Beam Subjected to a Unit Time Varying Sinusoidal Point Excitation at Fixed End

A single IC beam substructure with two modes will be employed. This is simple enough to highlight the essential elastic mode couplings but not refined enough to calculate an accurate result. The construction of the model is similar to the rotating beam model presented in subsection 4.2. The exception is that the rotating hinge component model is replaced by a model that provides the point excitation at the fixed end of the beam. This replacement model is illustrated in Figure 26.

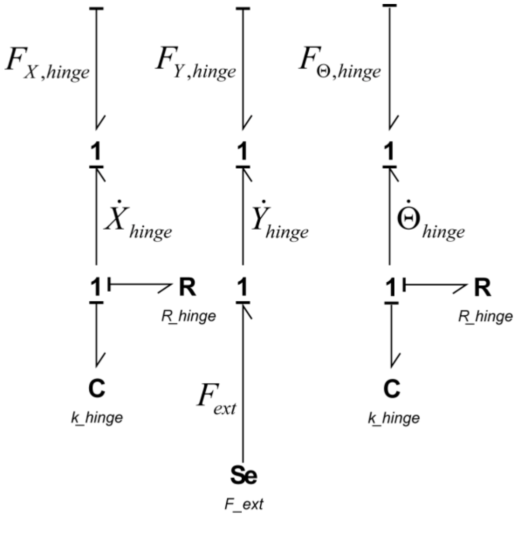

Figure 26: Bond Graph Model of Point Excitation at Fixed End of Beam

The corresponding equations are:

$$F_{X,hinge} = -\left(k_{hinge} X_{hinge} + R_{hinge} \dot{X}_{hinge}\right) \tag{6.1}$$
$$F_{Y,hinge} = F_{ext} = \sin \omega t$$
$$F_{\Theta,hinge} = -\left(k_{hinge} \Theta_{hinge} + R_{hinge} \dot{\Theta}_{hinge}\right)$$

The beam is excited at a frequency of *10 rad/s*. This frequency falls in between the first and second natural frequencies of the beam which is *4.6 rad/s* and *25 rad/s* respectively. The modal damping ratio is 0.01. The simulation run time is *50 s* with zero initial conditions. The solution will contain both transient and steady state responses. Other important model parameters are hinge stiffness value of 10e10, relative tolerance of 1e-3 and absolute tolerance of 5e-5. The frequency spectrums of the elastic modes responses, i.e. v_1 & v_2 are plotted in Figure 27.

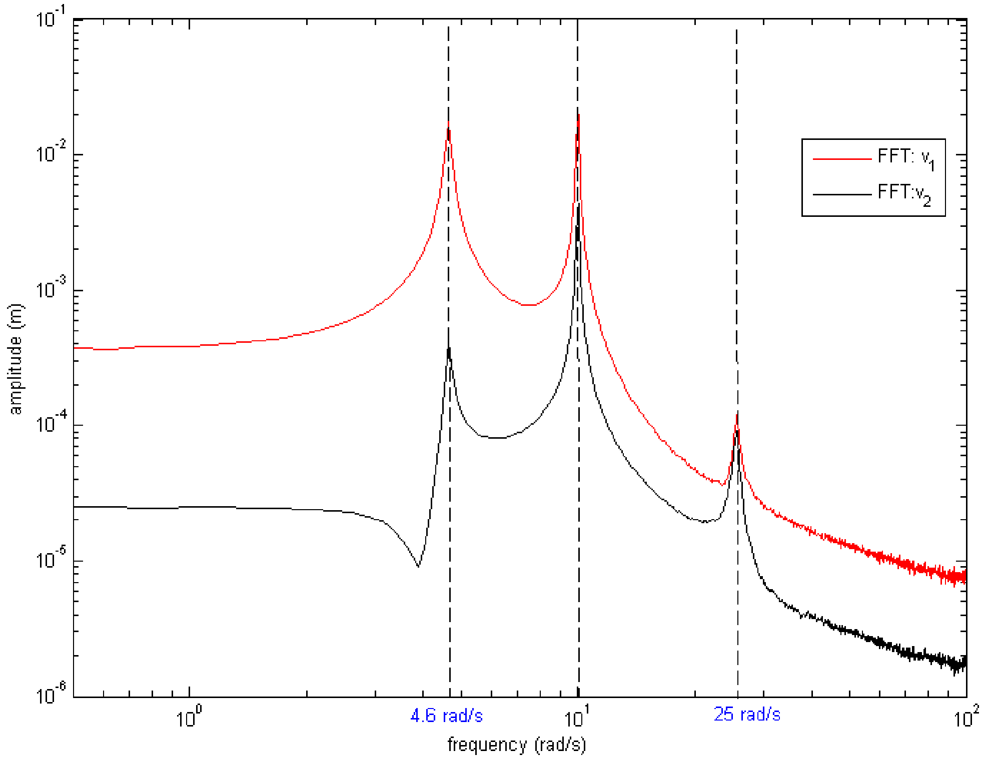

Figure 27: Frequency Spectrums of v_1 & v_2

The frequency spectrums of both the elastic modes peak at three distinct frequencies, namely the excitation frequency and the first two eigenfrequencies. The fact that the second mode's frequency spectrum peaks at the first mode's eigenfrequency means that there is energy transfer from the first mode to the second mode and vice versa. This highlights the elastic mode couplings in the IC beam. In a fully decoupled model such as the force-free beam bond graph model discussed in section 10.2, Karnopp, Margolis and

Rosenberg [29] and Margolis [37], the frequency spectrum for elastic mode response will only peak at two distinct frequencies, namely the excitation frequency and its own eigenfrequency. It is impossible for energy transfer between the modes to occur.

7. Dynamic Analysis – Spin-up Maneuver of Rotating Beam

In this section, the dynamics analysis of the spin-up maneuver is performed. The problem description was presented in subsection 4.1. Similar to section 5, the modal parameters in this section are also calculated from an eigenvalue analysis of a finite element model of the IC beam substructure using 20 planar two-node linear beam elements. The axial shortening, tip deflection and tip slope are used as basis for comparison throughout this section.

First, in subsection 7.1, the IC beam will be verified against the numerical results presented in Wu, *et.al.* [25].

Second, from subsections 7.2 to 7.7, detailed convergence studies are performed. The following important model parameters were studied:

- Resistance value of resistor at rotating hinge, *R_rot*
- Stiffness value of all hinges, *k_hinge*
- Absolute error tolerance, *AbsTol*
- Relative error tolerance, *RelTol*
- Number of substructures
- Number of modes

Third, in subsection 7.8, the effect of structural damping on the solutions is investigated.

Fourth, in subsection 7.9, the modal acceleration method proposed in subsection 3.5 will be applied and its benefits evaluated.

Otherwise specified, the following default model parameters will be used: *k_hinge = 1e10*, *R_rot = 1e3*, *RelTol = 1e3*, *AbsTol = 5e5*. The simulations were performed in Matlab 7.8.0.347, 64 bit version on an Intel Core 2 Duo T9400 2.53 GHz machine with 8 GB of memory.

7.1. Results Verification

The IC beam is verified against the results presented in table 1 in Wu, *et.al.* [25]. The results comparisons are presented in Table 5. The time histories of the tip deflection are plotted in Figure 28 and Figure 29. 10 modes are employed.

The following notations are used:

- Wu – results from Wu, *et.al.* [25]
- IC – results from IC beam
- 1S, 4S, 6S – 2, 4, 6 substructures respectively

The results from IC beam generally agree very well with the results presented in Wu, *et.al.* [25]. However, notice the small discrepancies in the results of the $\omega_s = 4\ rad/s$ case. This is a more nonlinear load case. Therefore, the results are more sensitive to the differences in modeling techniques and model parameters. It is accepted that the below 3% maximum difference in the $\omega_s = 4\ rad/s$ and 6 substructure case is sufficient for verification. These slight differences in results will not be further investigated.

Table 5: Verification of IC Beam against Results from Table 1 in Wu, *et.al.* [25]

$\omega_s = 1\ rad/s$			
No. Substructures	Wu, *et.al.* (28) {a}	IC beam {b}	({b} – {a}) / {a} x 100%
1	-0.148	-0.148	0.0000
4	-0.143	-0.1424	-0.4196
6	-0.1425	-0.1422	-0.2105
$\omega_s = 2\ rad/s$			
No. Substructures	Wu, *et.al.* (28) {a}	IC beam {b}	({b} – {a}) / {a} x 100%
1	-0.345	-0.3423	-0.7826
4	-0.284	-0.2817	-0.8099
6	-0.282	-0.2818	-0.0709
$\omega_s = 4\ rad/s$			
No. Substructures	Wu, *et.al.* (28) {a}	IC beam {b}	({b} – {a}) / {a} x 100%
1	∞	∞	-
4	-0.556	-0.5632	1.2950
6	-0.543	-0.5586	2.8729

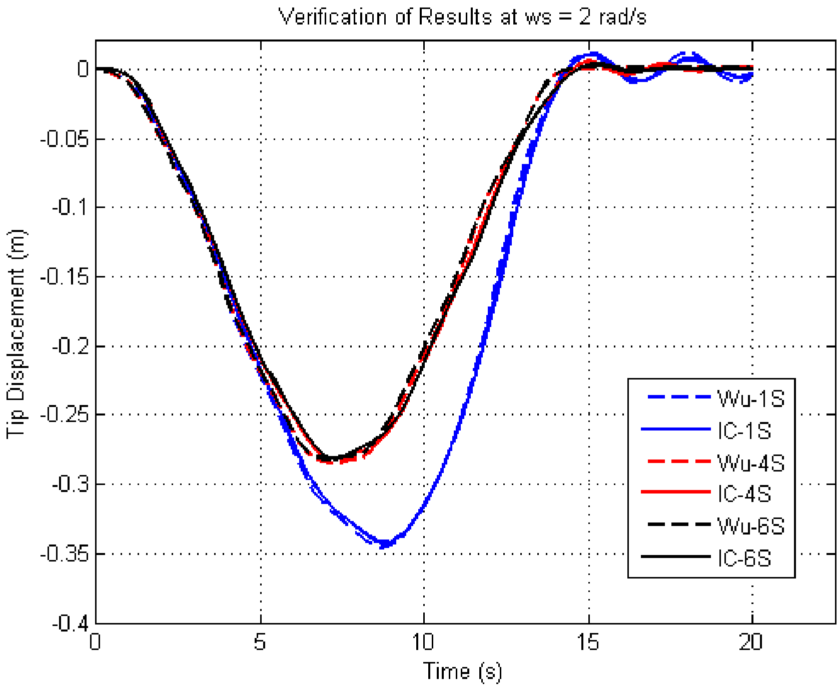

Figure 28: Time History of Tip Deflection: Verification at *ω_s = 2 rad/s*

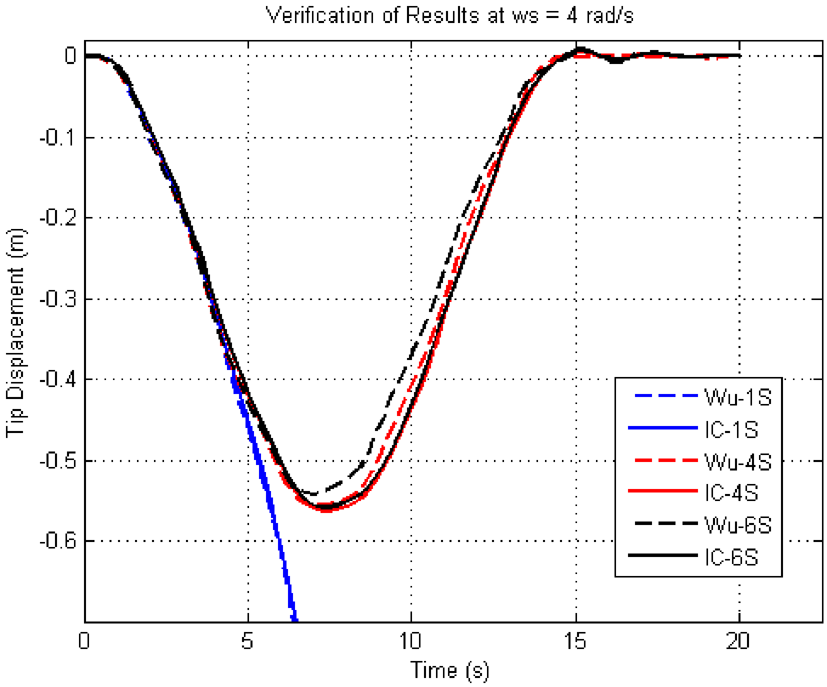

Figure 29: Time History of Tip Deflection: Verification at *ω_s = 4 rad/s*

7.2. Resistance Value of Resistor at the Rotating Hinge

In this subsection, a convergence study of the resistance value of the resistor at the rotating hinge (denoted '*R_rot'*) is performed. Refer to subsection 4.2.1.3 for the definition of this resistor. As previously mentioned, the purpose of this resistor is to ensure that the model remains in complete integral causality. A large *R_rot* value is preferred to ensure a small difference in the actual and prescribed rotational velocities (third line of equation (4.8)). This minimizes error in the solution.

The six substructure, 10 modes, $\omega_s = 4$ *rad/s* case will be discussed. The time histories of the axial shortening, tip deflection and tip slope are plotted in Figure 30, Figure 31 and Figure 32 respectively. The percentage errors of the minimum tip displacements for the different *R_rot* values used are plotted in Figure 33. Figure 34 plots the computation times required for the different *R_rot* values used.

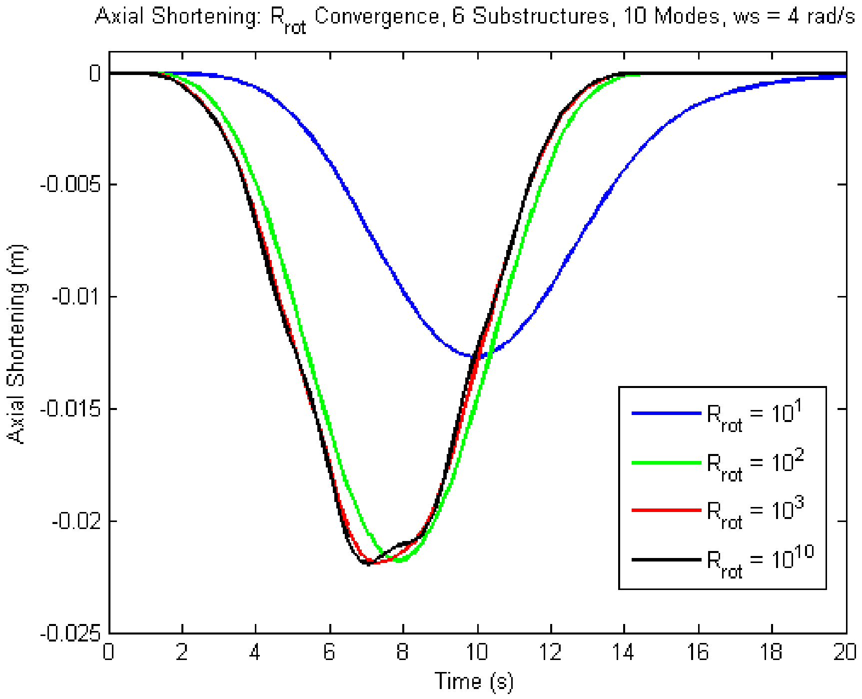

Figure 30: Time History of Axial Shortening, *R_rot* Convergence, 6 Substructures, 10 Modes, $\omega_s = 4$ *rad/s*

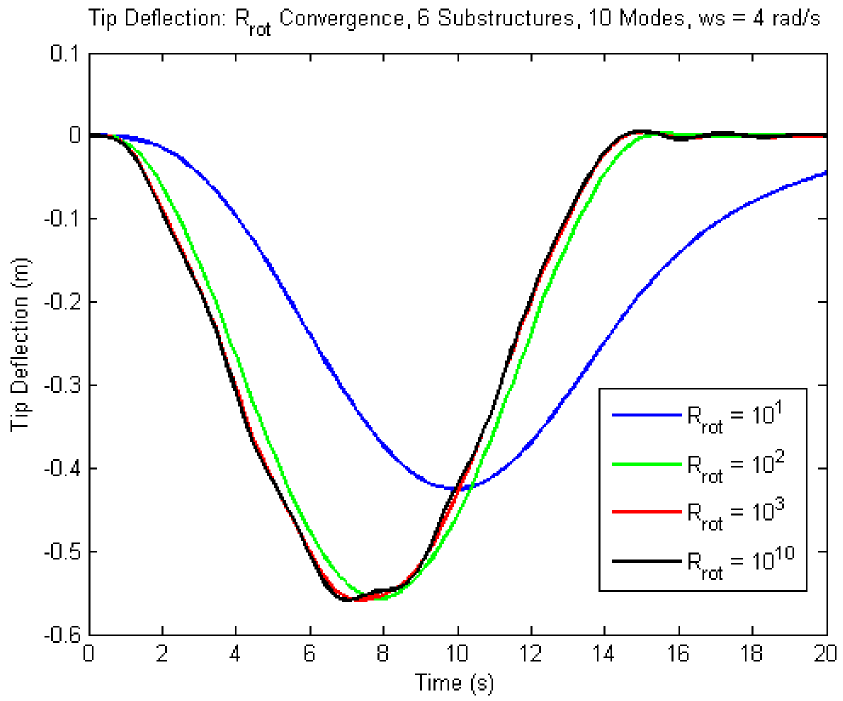

Figure 31: Time History of Tip Deflection, *R_rot* Convergence, 6 Substructures, 10 Modes, ω_s = *4 rad/s*

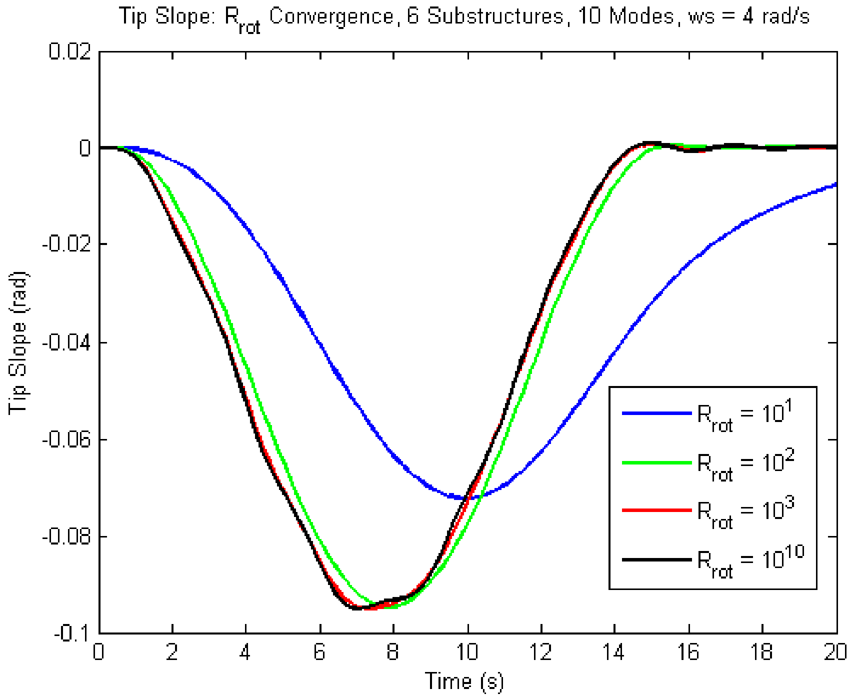

Figure 32: Time History of Tip Slope, *R_rot* Convergence, 6 Substructures, 10 Modes, ω_s = *4 rad/s*

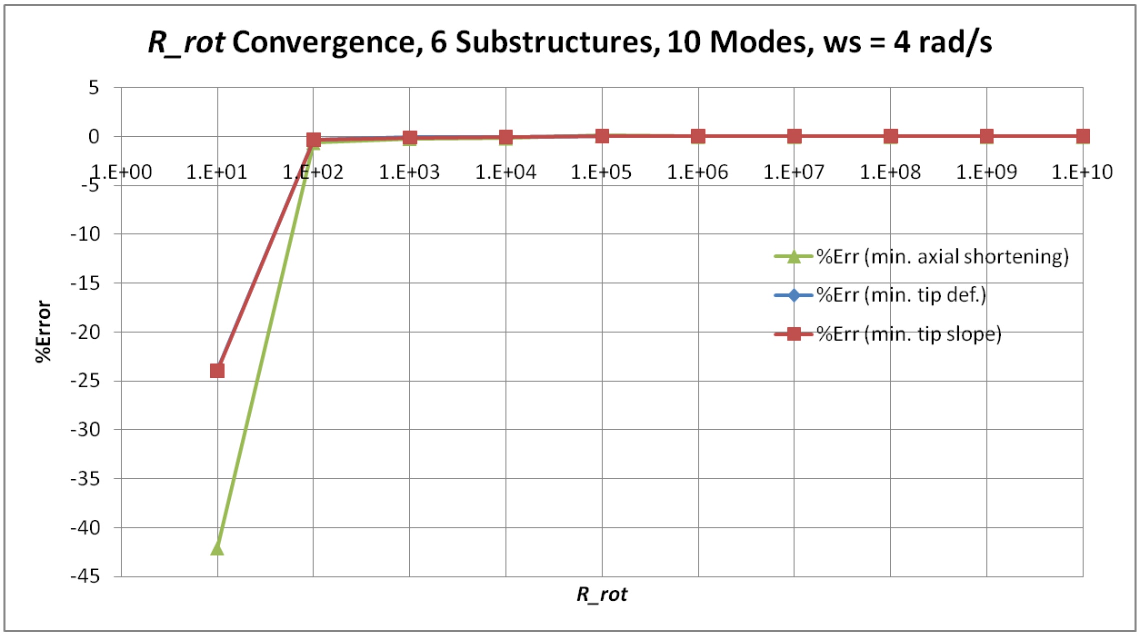

Figure 33: *R_rot* Convergence, 6 Substructures, 10 Modes ω_s = *4 rad/s*

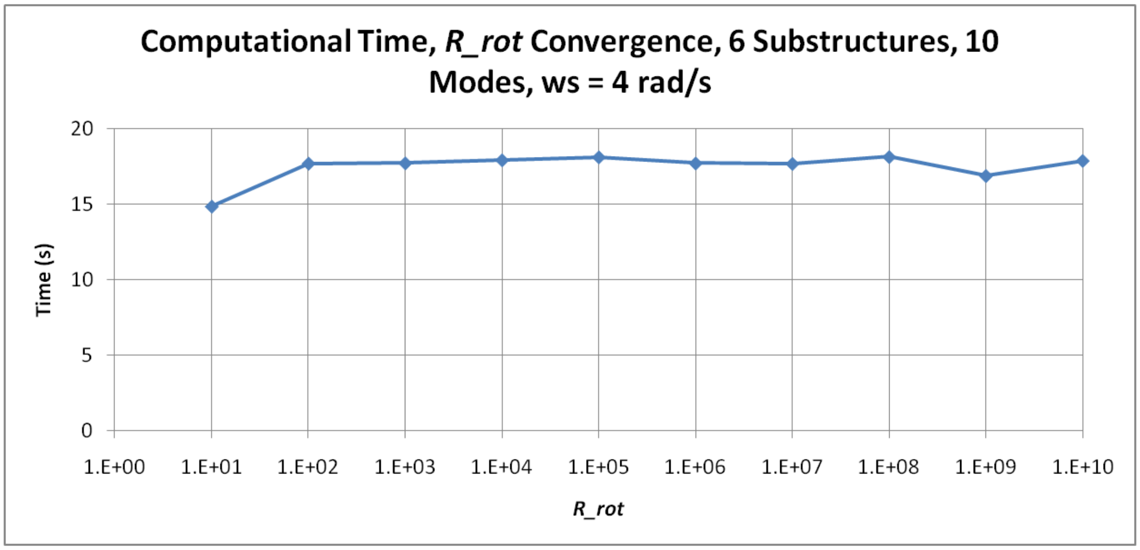

Figure 34: Computational Time, *R_rot* Convergence, 6 Substructures, 10 Modes, ω_s = *4 rad/s*

Using *R_rot = 1e1* results in erroneous solutions. There will be errors of approximately -42% for the minimum axial shortening and approximately -24% for the minimum tip deflection and slope. Using *R_rot >= 1e2* is sufficient to achieve errors below 5% for all minimum tip displacements. However, using *R_rot = 1e-2* would still result in a small error in the form of a leading phase difference (Figure 30, Figure 31 and Figure 32). On the other hand, using *R_rot = 1e-3* will yield solutions of virtually no errors. In general, using different *R_rot* values do not significantly affect the computational times required.

7.3. Stiffness Value of Springs at All Hinges

In this subsection, a convergence study of the stiffness value of the springs at all hinges (denoted '*k_hinge*') is performed. Refer to subsections 4.2.1.3 and 0 for the definition of this spring. As previously mentioned, the purpose of this spring is to ensure that the model remains in complete integral causality. A large *k_hinge* value is preferred to ensure small relative displacements between two interconnecting IC beams substructures and small translational displacements at the rotating hinge. This minimizes error in the solution.

The six substructure, 10 modes, $\omega_s = 4\ rad/s$ case is discussed. The errors are measured as the percentage difference between the solutions at the current *k_hinge* value and *k_hinge = 1e15*. The percentage errors of the minimum tip displacements for the different *k_hinge* values used are plotted in Figure 35. Figure 36 plots the computation times required for the different *k_hinge* values used.

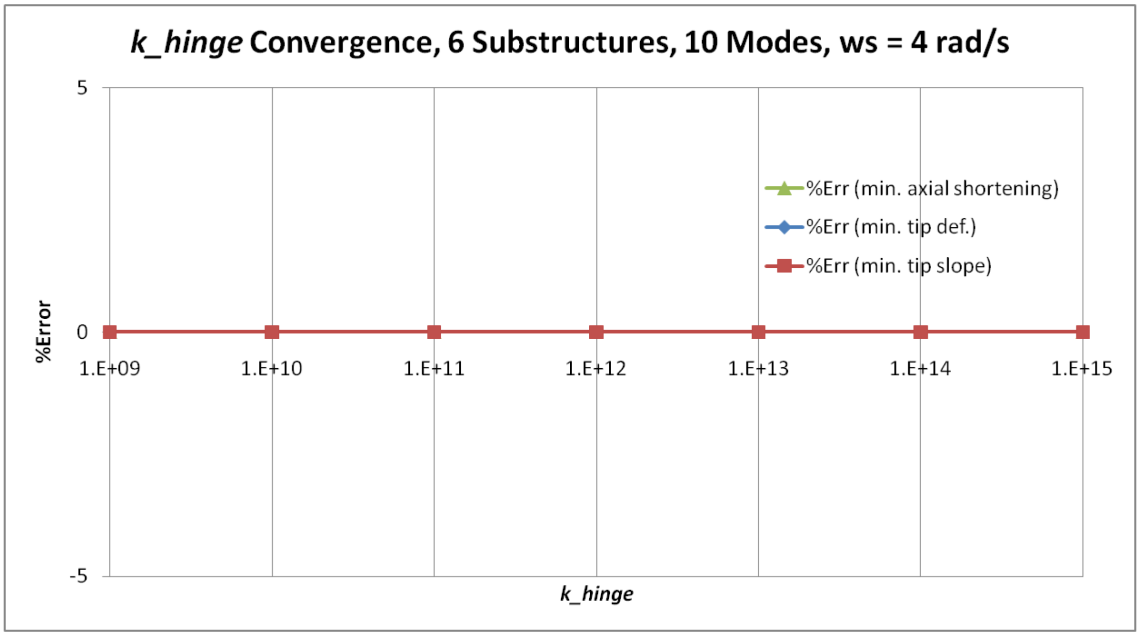

Figure 35: *k_hinge* Convergence, 6 Substructures, $\omega_s = 4\ rad/s$

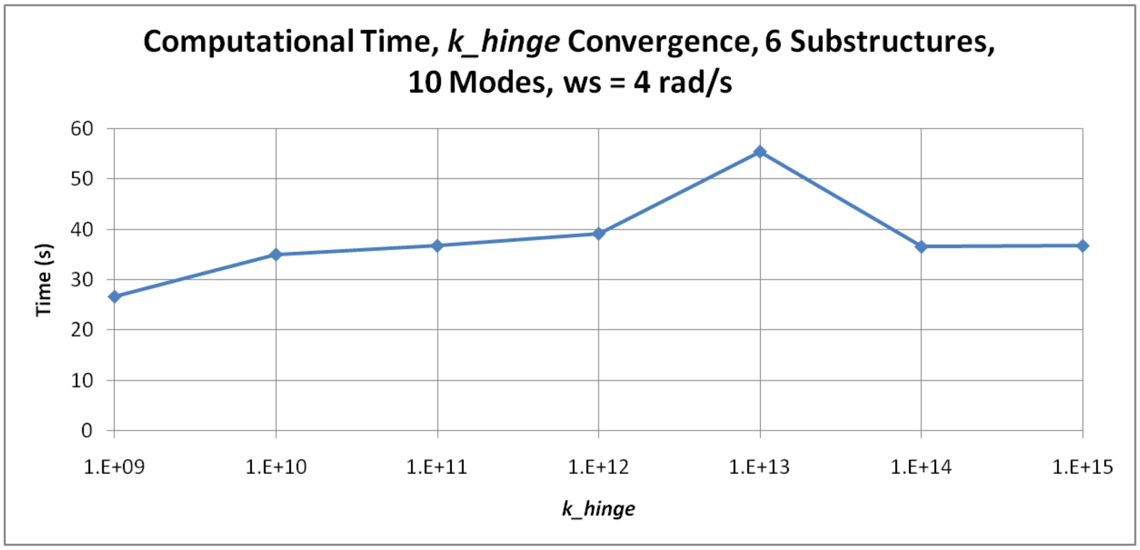

Figure 36: Computational Time, *k_hinge* Convergence, 6 Substructures, ω_s = *4 rad/s*

The solutions take too long to converge for *k_hinge* < *1e9* and thus discarded here. The reason might be that insufficiently large *k_hinge* values result in large relative motions between the interconnected substructures and require extremely small times steps to solve for. There are virtually no differences in the solutions for the rest of the *k_hinge* values. This is because these *k_hinge* values are large enough to ensure accurate solutions. In general, increasing *k_hinge* increases the computational time required. However, this increase is not significant.

7.4. Absolute Error Tolerance

In this subsection, a convergence study of the absolute error tolerance value (denoted '*AbsTol*') is performed. *AbsTol* is a threshold below which the *i-th* solution component is unimportant. For more details, refer to help on 'odeset' in Matlab. A small *AbsTol* value results in higher accuracy.

The six substructures, 10 modes, ω_s = *4 rad/s* case is discussed. The errors are measured as the percentage difference between the solutions at the current *AbsTol* value and *AbsTol* = *1e-6*. Note that the solutions are in the order of 0.1 m. The time histories of the axial shortening, tip deflection and tip slope are plotted in Figure 37, Figure 38 and Figure 39 respectively. The percentage errors of the minimum tip displacements for the different *AbsTol* values used are plotted in Figure 40. Figure 41 plots the computation times required for the different *AbsTol* values used.

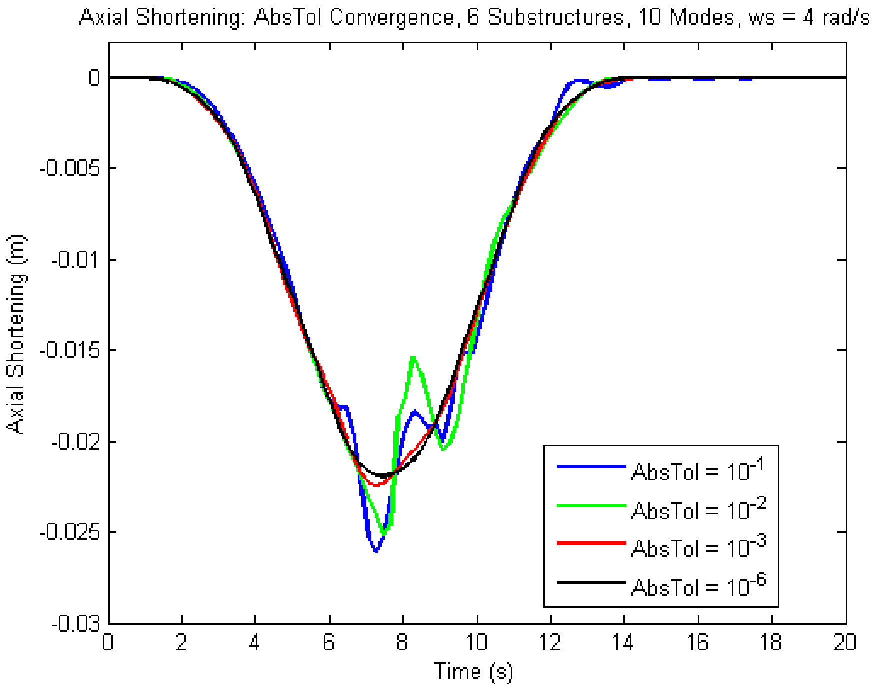

Figure 37: Time History of Axial Shortening, *AbsTol* Convergence, 6 Substructures, 10 Modes, ω_s = *4 rad/s*

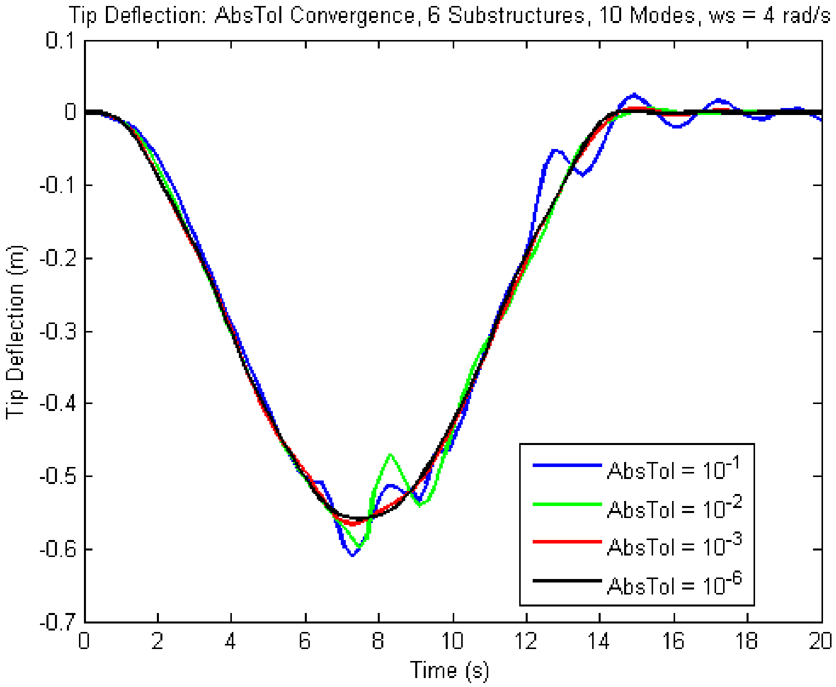

Figure 38: Time History of Tip Deflection, *AbsTol* Convergence, 6 Substructures, 10 Modes, ω_s = *4 rad/s*

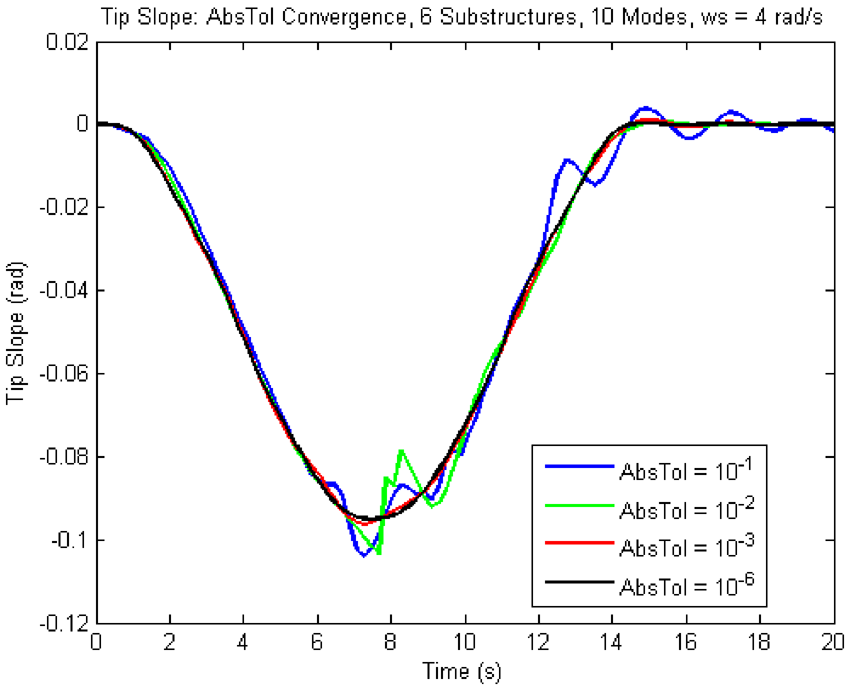

Figure 39: Time History of Tip Slope, *AbsTol* Convergence, 6 Substructures, 10 Modes, ω_s = *4 rad/s*

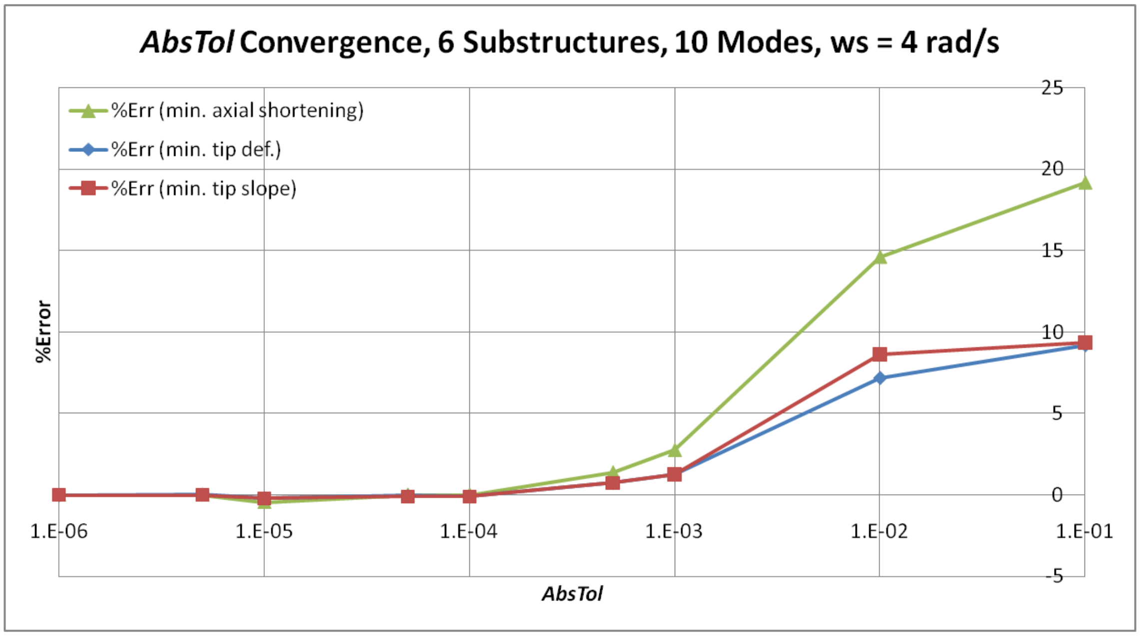

Figure 40: *AbsTol* Convergence, 6 Substructures, 10 Modes, ω_s = *4 rad/s*

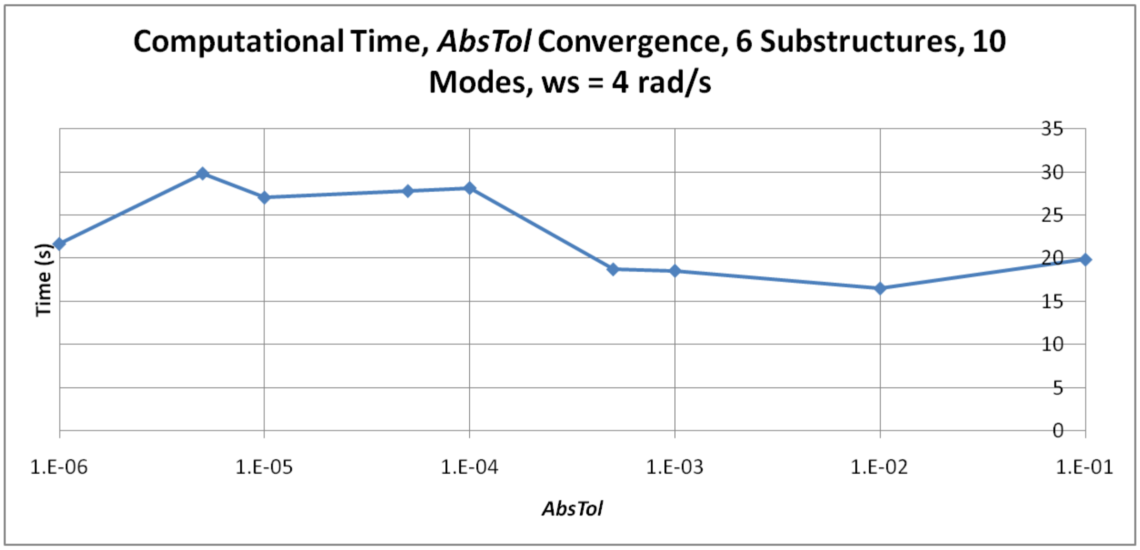

Figure 41: Computational Time, *AbsTol* Convergence, 6 Substructures, 10 Modes, ω_s = *4 rad/s*

Using *AbsTol <= 1e-2* result in erroneous solutions. Incorrect high frequency oscillations will appear in the tip displacement time histories. The errors for the minimum axial shortening will be more than 15% and the errors for the minimum tip deflection and slope will be more than 5%. Using *AbsTol = 1e-3* achieves less than 3% errors for all minimum tip displacements. Using *AbsTol >= 1e4* will virtually eliminate all errors. It is also observed that the convergence rate for minimum axial shortening is slower than the minimum tip deflection and slope. In general, there are no significant differences in the computational times required when different *AbsTol* values are used. This means that specifying smaller *AbsTol* values will not increase the computational times required. This indifference in computational times is also mentioned in the 'odeset' help documentation in Matlab.

7.5. Relative Error Tolerance

In this subsection, a convergence study of the relative error tolerance value (denoted '*RelTol*') is performed. This is a measure of the error relative to the size of each solution component. It controls the number of correct digits in all solution components, except those which are smaller than the thresholds *AbsTol*. *RelTol = 1e-3* means 0.01% accuracy. For more details, refer to help on 'odeset' in Matlab. A smaller *RelTol* value results in higher accuracy.

The six substructures, 10 modes case, ω_s = *4 rad/s* case is discussed. Also, *AbsTol = 1e3* is chosen as it is small enough to ensure a sufficiently accurate solution (refer to subsection 7.4) and yet not too small to result in too many of the solution components not being controlled by *RelTol*. This is to better observe the effect of the *RelTol* value. The errors are measured as the percentage difference between the solutions at the current *RelTol* value and *RelTol = 1e-6*. Once again, note that the solutions are in the order of 0.1 m. The time histories of the axial shortening, tip deflection and tip slope are plotted in Figure 42, Figure 43 and Figure 44 respectively. The percentage errors of the minimum tip displacements for the different *RelTol* values used are plotted in Figure 45. Figure 46 plots the computation times required for the different *RelTol* values used.

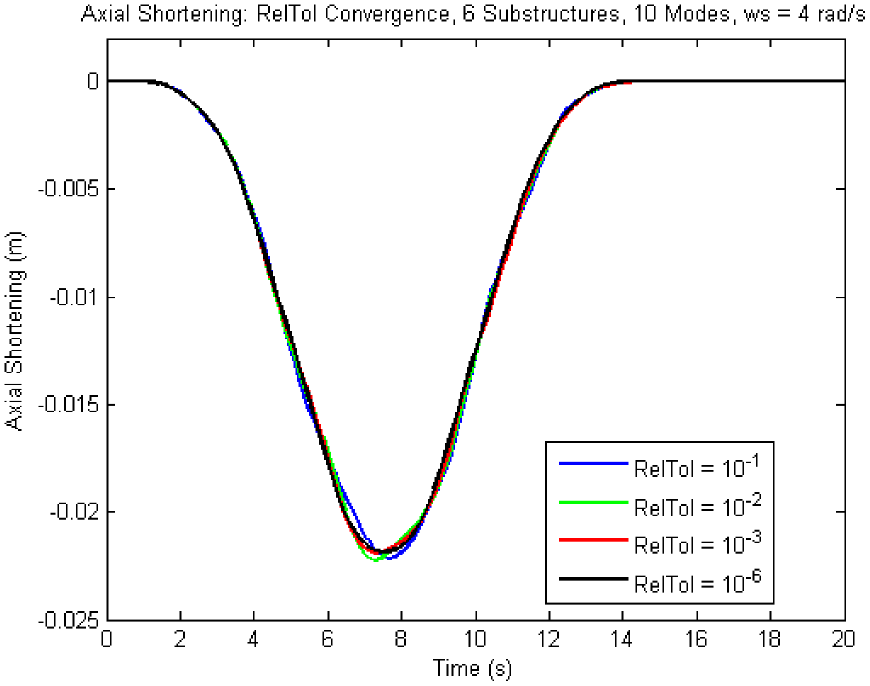

Figure 42: Time History of Axial Shortening, *RelTol* Convergence, 6 Substructures, 10 Modes, ω_s = *4 rad/s*

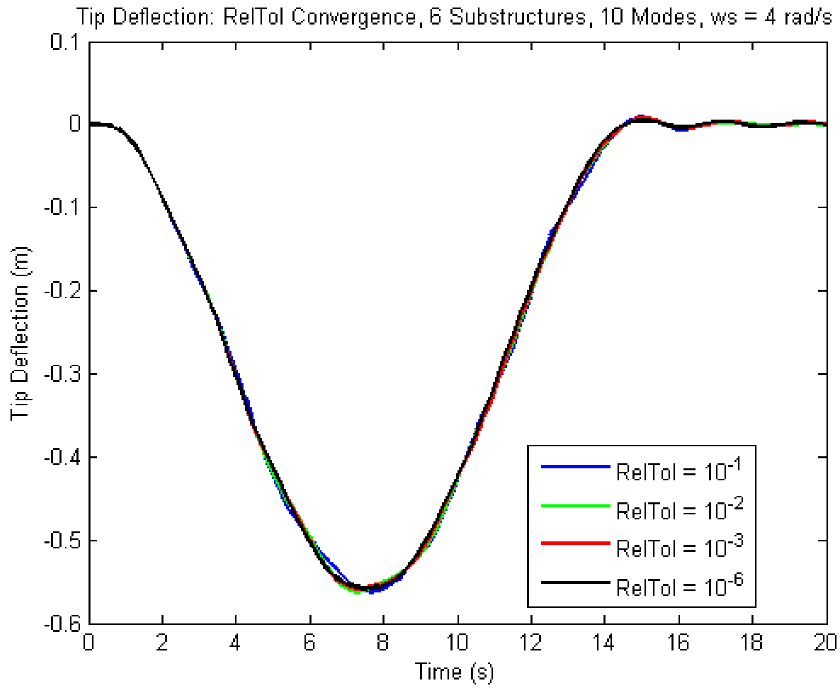

Figure 43: Time History of Tip Deflection, *RelTol* Convergence, 6 Substructures, 10 Modes, ω_s = *4 rad/s*

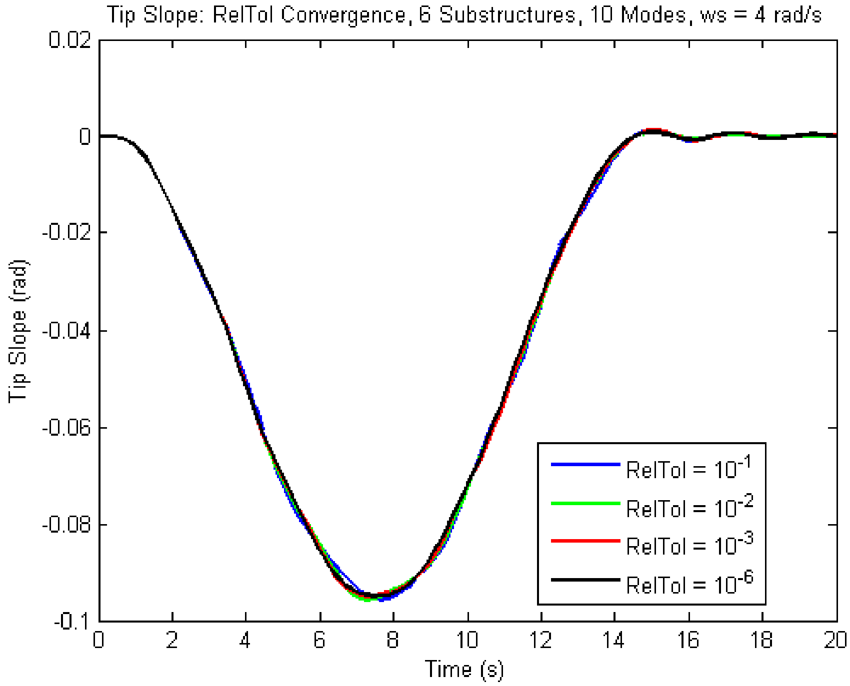

Figure 44: Time History of Tip Slope, *RelTol* Convergence, 6 Substructures, 10 Modes, ω_s = *4 rad/s*

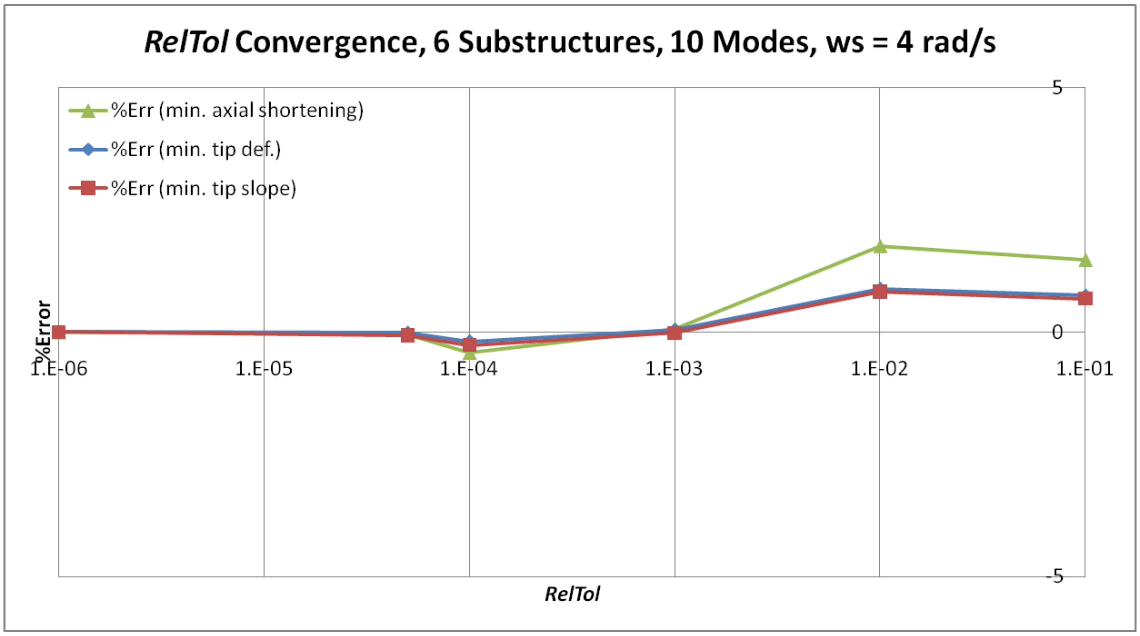

Figure 45: *RelTol* Convergence, 6 Substructures, 10 Modes, ω_s = *4 rad/s*

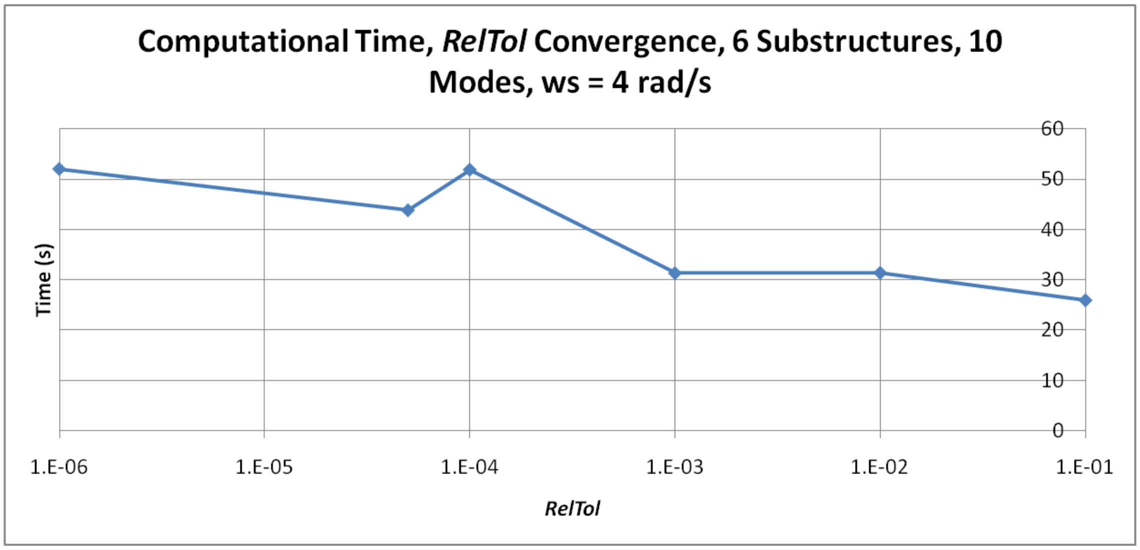

Figure 46: Computational Time, *RelTol* Convergence, 6 Substructures, 10 Modes, ω_s = *4 rad/s*

The *RelTol* value does not significantly affect the solution. This suggests that the *AbsTol* control dominates the accuracy control of the solution. It is also observed that specifying a smaller value of *RelTol* increases the computational time required. This is in contrast to *AbsTol* where using different *AbsTol* values do not affect the computational time required.

7.6. Number of Substructures

In this subsection, a convergence study of the number of substructures is performed. 10 modes are employed. The errors are measured as the percentage difference between the solutions at the current number of substructures used and eight substructures. Figure 47 plots the substructure convergence for the various ω_s cases and Figure 48 plots the computational times required. Only the time history plots for the $\omega_s = 8\ rad/s$ case will be presented.

The following notations are used:

- min. AS – minimum axial shortening
- min. TD – minimum tip deflection
- min. TS – minimum tip slope
- The rotational velocity after AD, TD or TS specifies the ω_s used.
- 1S, 2S, 4S, 8S – 1, 2, 4 and 8 substructures respectively.

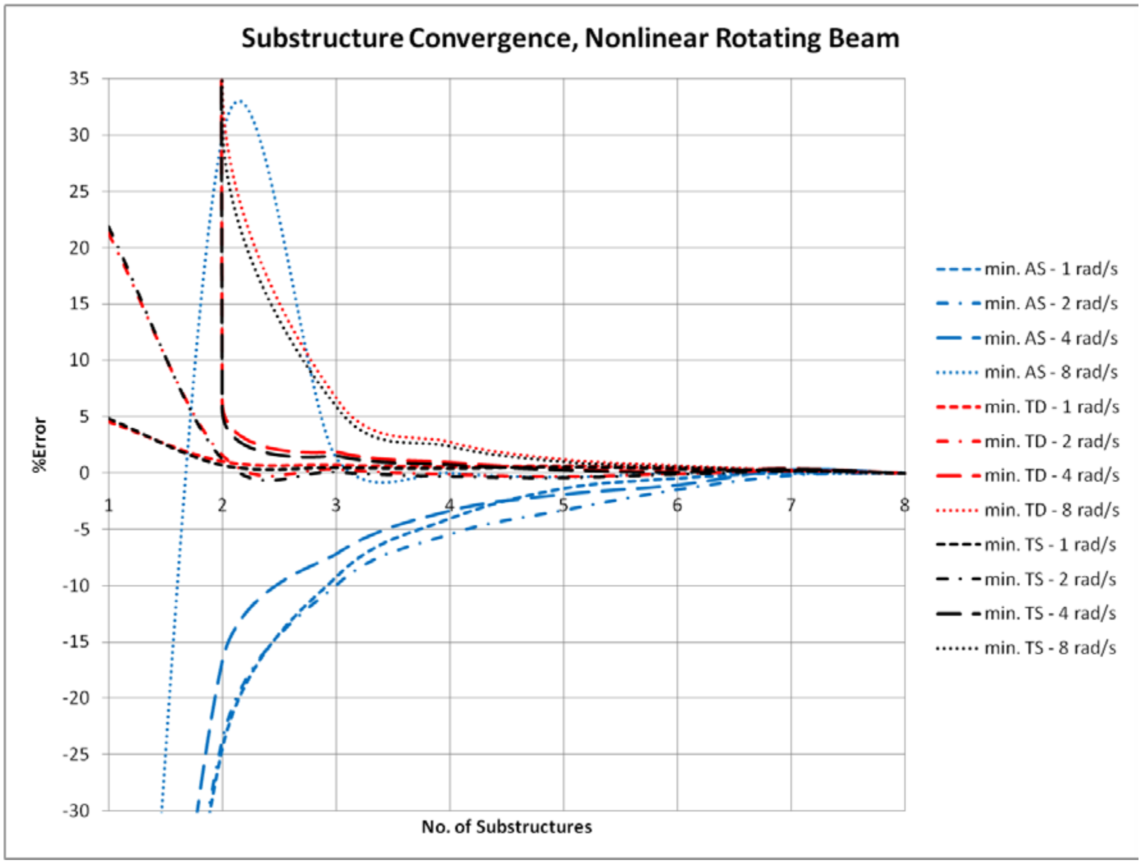

Figure 47: Substructure Convergence, Nonlinear Rotating Beam

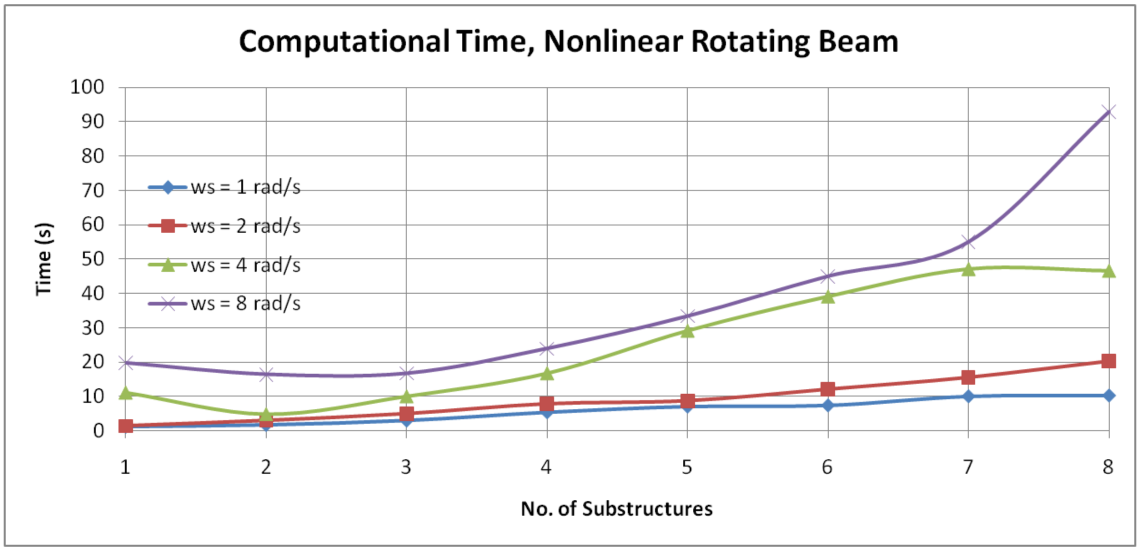

Figure 48: Computational Time, Nonlinear Rotating Beam

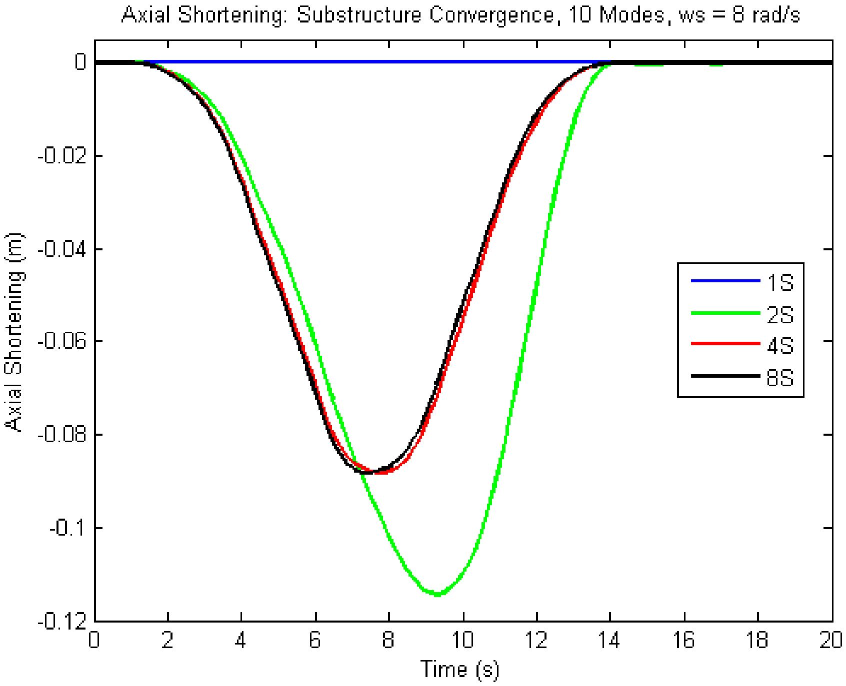

Figure 49: Time History of Axial Shortening, Substructure Convergence, 10 Modes, $\omega_s = 8$ *rad/s*

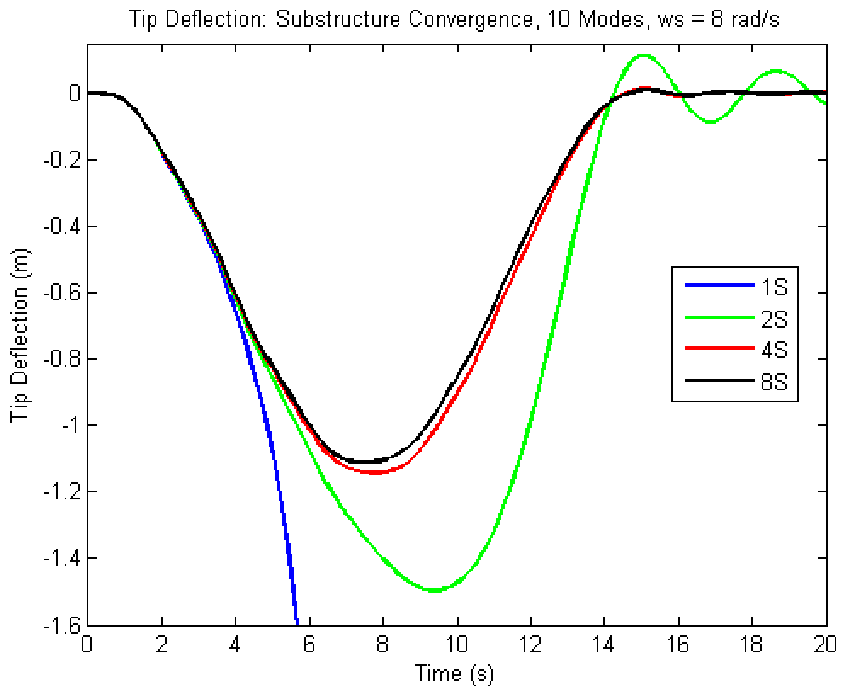

Figure 50: Time History of Tip Deflection, Substructure Convergence, 10 Modes, ω_s = 8 rad/s

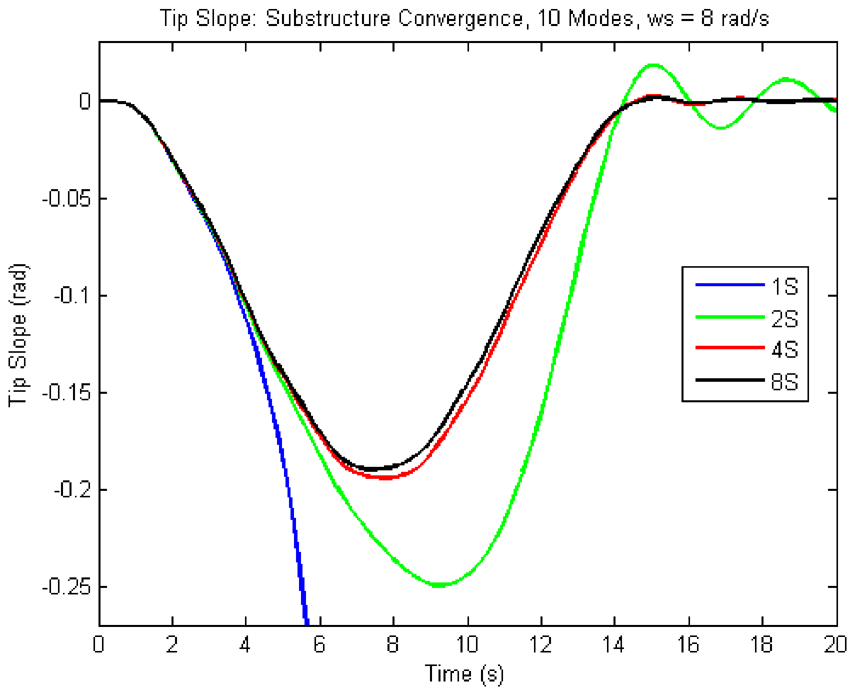

Figure 51: Time History of Tip Slope, Substructure Convergence, 10 Modes, ω_s = 8 rad/s

The $\omega_s = 1$ *rad/s* is a relatively linear case. Using just one substructure, i.e. linear beam is sufficient to achieve accurate results with less than 5% errors for minimum tip deflection and slope. However, there is no axial shortening when one substructure is used. This explains the asymptotic behavior of the axial shortening convergence curves. Multi substructure models must be used to account for axial shortening. For the slightly nonlinear case of $\omega_s = 2\ rad/s$, the linear model will give rise to errors of about 22% in the minimum tip deflection and slope. The tip displacements will be unbounded if just one substructure is employed for the high nonlinearity cases, i.e. $\omega_s = 4\ \&\ 8\ rad/s$. This explains the asymptotic behavior of the minimum tip deflection and slope convergence curves. In general, with the exception of the $\omega_s = 8\ rad/s$ case, specifying at least two substructures is sufficient achieve below 5% errors for the minimum tip deflection and slope.

The convergence rate for the minimum axial shortening is significantly slower than the minimum tip deflection and slope. In general, with the exception of the $\omega_s = 8\ rad/s$ case, at least 5 substructures are required to achieve below 5% error for the minimum axial shortening for all ω_s. The convergence rates for all deflections are not adversely affected when different ω_s values are specified.

The convergence rates for the $\omega_s = 8\ rad/s$ case are significantly different from the rest of the ω_s cases. For the minimum tip deflection and slope, the convergence is significant slower than the $\omega_s = 1, 2\ \&\ 4\ rad/s$ cases, requiring at least four substructures to achieve below 5% errors. For the minimum axial shortening, the trend of the convergence curve is significantly different. The value of the minimum axial shortening computed is larger than the converged value when insufficient numbers of substructures are used. This is opposite to the trends observed for the $\omega_s = 1, 2\ \&\ 4\ rad/s$ cases. It will be interesting to investigate the trend for even higher rotational speeds. However, this will not be performed as the IC beam is targeted specifically at wind turbine rotor blades. Wind turbine rotors do not spin at extremely high rotational speeds. Therefore, the behavior of the IC beam at extremely high rotational speeds is out of the scope of this thesis.

The computational time required increases with the number of substructures specified. This increase is more pronounced at higher values of ω_s and larger numbers of substructures. Also, notice that more computational time is required for a one substructure model as compared to a two substructure model for the $\omega_s = 4\ rad/s$ case. This might be due to that the solution of this case is unbounded for the one substructure model and thus require more efforts to solve for.

7.7. Modal Convergence

In this subsection, a convergence study of the number of modes is performed. The errors are measured as the percentage difference between the solutions at the current number of modes used and the maximum number of modes, i.e. 40 modes. The notations used in this subsection follow from subsection 7.6.

Modal Convergence of Linear Model

The linear cases are dominated by the first mode. There are virtually no improvements in the solution when more modes are used. This has also been observed in Wu, *et.al.* [25]. The ω_s = *2 rad/s* case requires more computational efforts. Employing more modes will also increase the computational times required. This increase is more pronounced for the ω_s = *2 rad/s* case. However, these are very little amounts of computational times as compared to the nonlinear cases (presented later). The solution for the ω_s = *4 rad/s* case is unbounded and this discarded here. Once again, note that there is no axial shortening for the linear model.

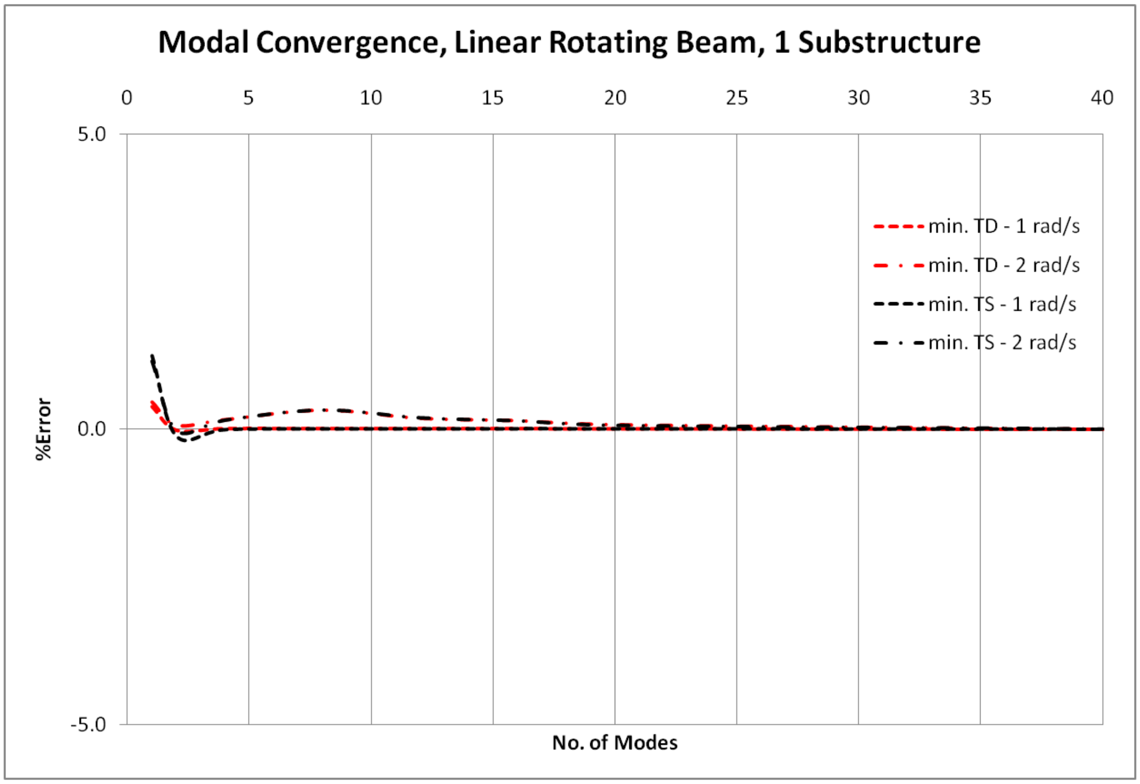

Figure 52: Modal Convergence, Linear Rotating Beam, 1 Substructure

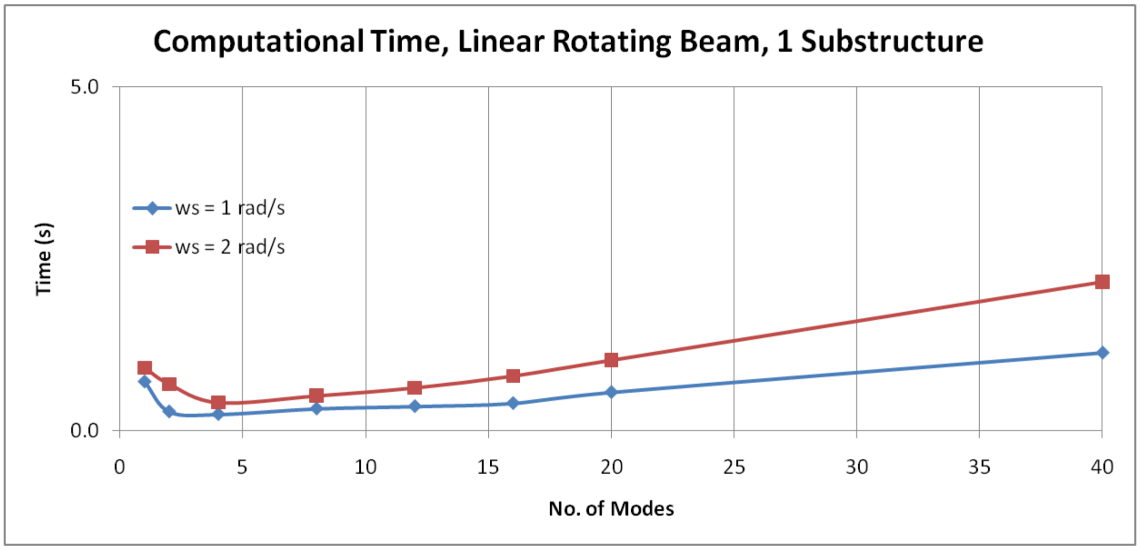

Figure 53: Computational Time, Linear Rotating Beam, 1 Substructure

Modal Convergence of Nonlinear Models at Different Number of Substructures

Modal convergence is slower when more substructures are employed. More modes are required to attain the same accuracy when more substructures are employed. Using too little modes in the multi substructure cases lead to erroneous solutions. The deflections will be significantly smaller than the converged solution. Modal convergence is slower for the minimum axial shortening as compared to the minimum tip deflection and slope. In general, using 10 modes will be sufficient to achieve below 5% errors for the minimum tip deflection and slope. For the minimum axial shortening, 15 modes are required for 5% accuracy.

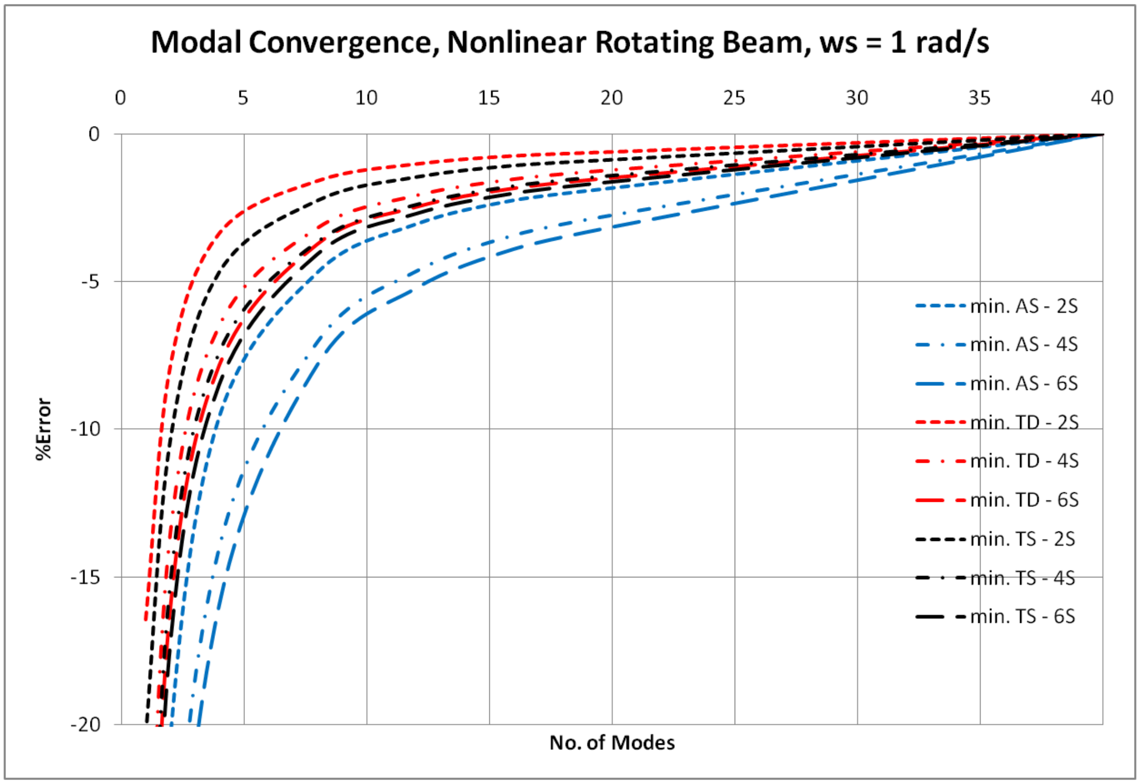

Figure 54: Modal Convergence, Nonlinear Rotating Beam, $\omega_s = 1$ rad/s

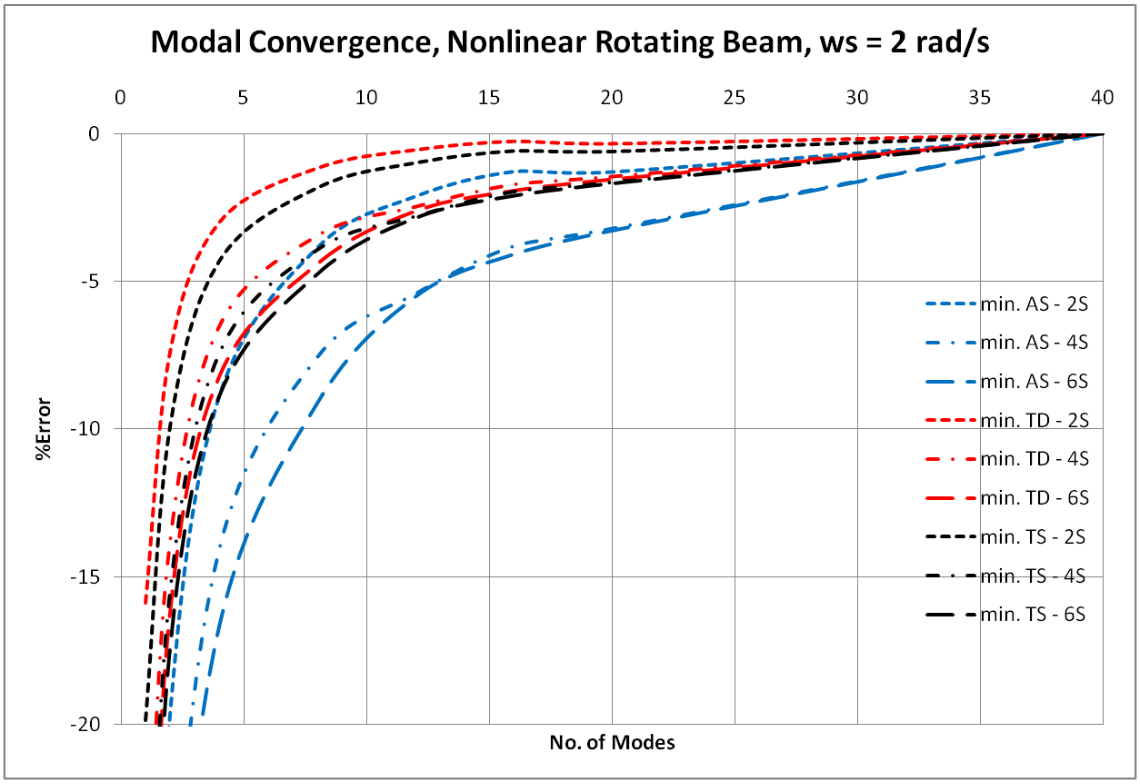

Figure 55: Modal Convergence, Nonlinear Rotating Beam, ω_s = *2 rad/s*

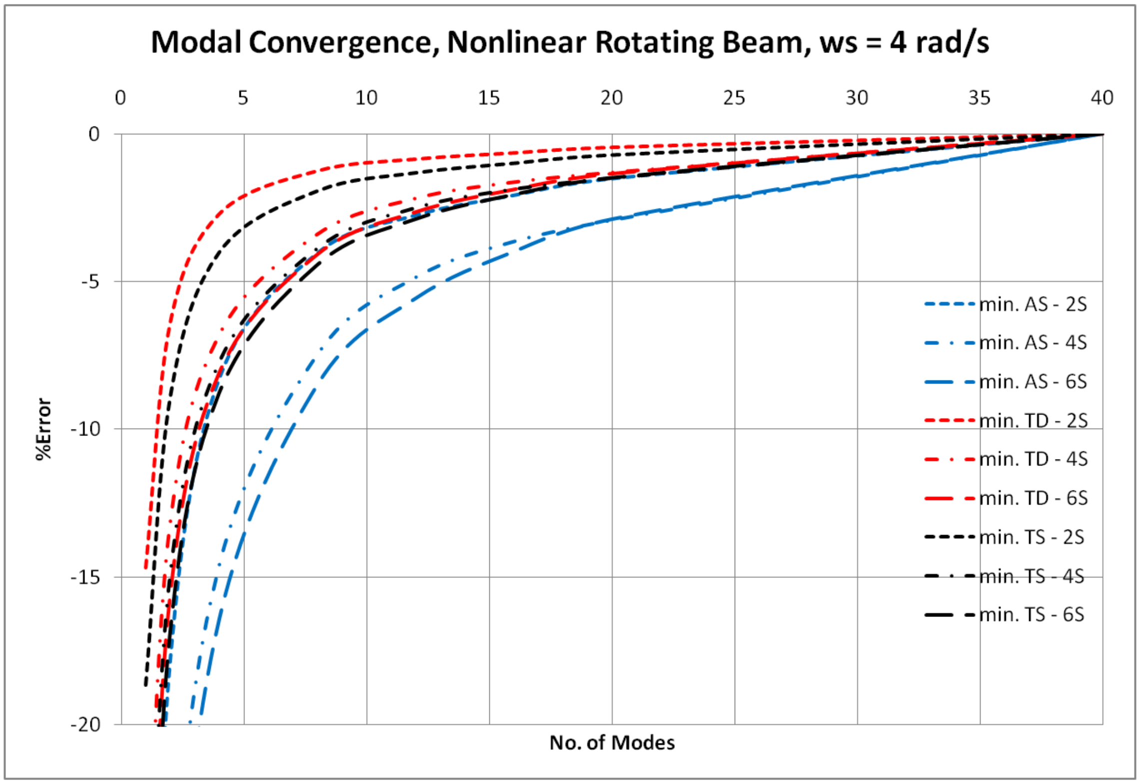

Figure 56: Modal Convergence, Nonlinear Rotating Beam, ω_s = *4 rad/s*

Figure 57, Figure 58 and Figure 59 present the time history plots of the axial shortening, tip deflection and tip slope of the 6 substructure, $\omega_s = 4\ rad/s$ case for different number of modes employed.

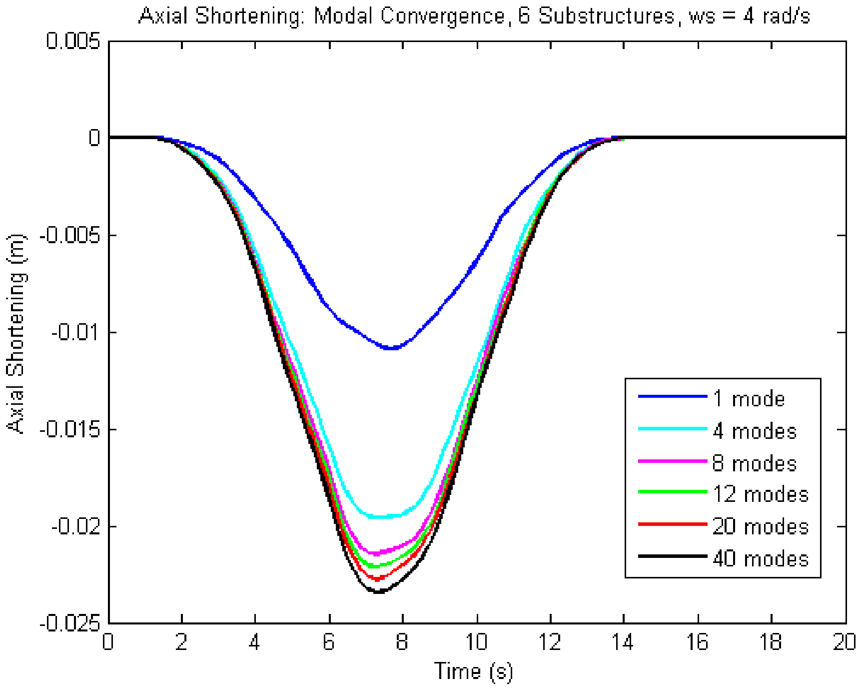

Figure 57: Time History of Axial Shortening, Modal Convergence, 6 Substructures, $\omega_s = 4\ rad/s$

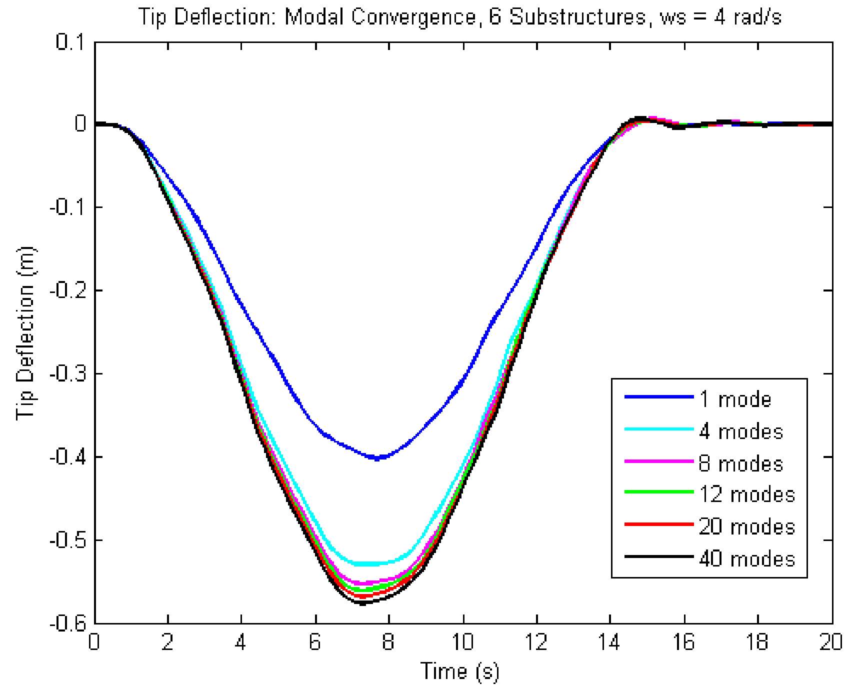

Figure 58: Time History of Tip Deflection, Modal Convergence, 6 Substructures, $\omega_s = 4$ rad/s

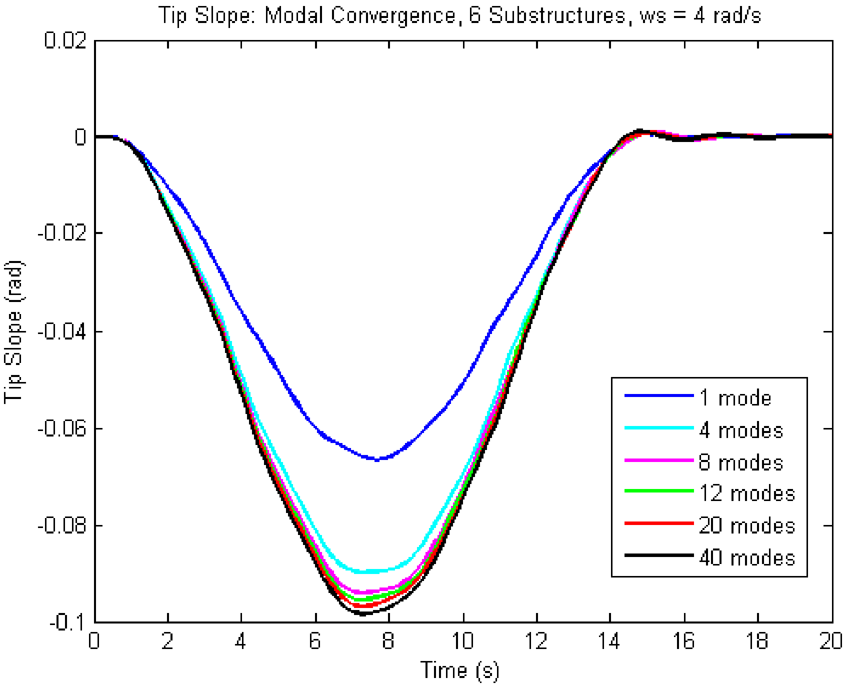

Figure 59: Time History of Tip Slope, Modal Convergence, 6 Substructures, $\omega_s = 4$ rad/s

Modal Convergence of Nonlinear Models at Different ω_s

Different values of ω_s do not significantly affect the rate of modal convergence.

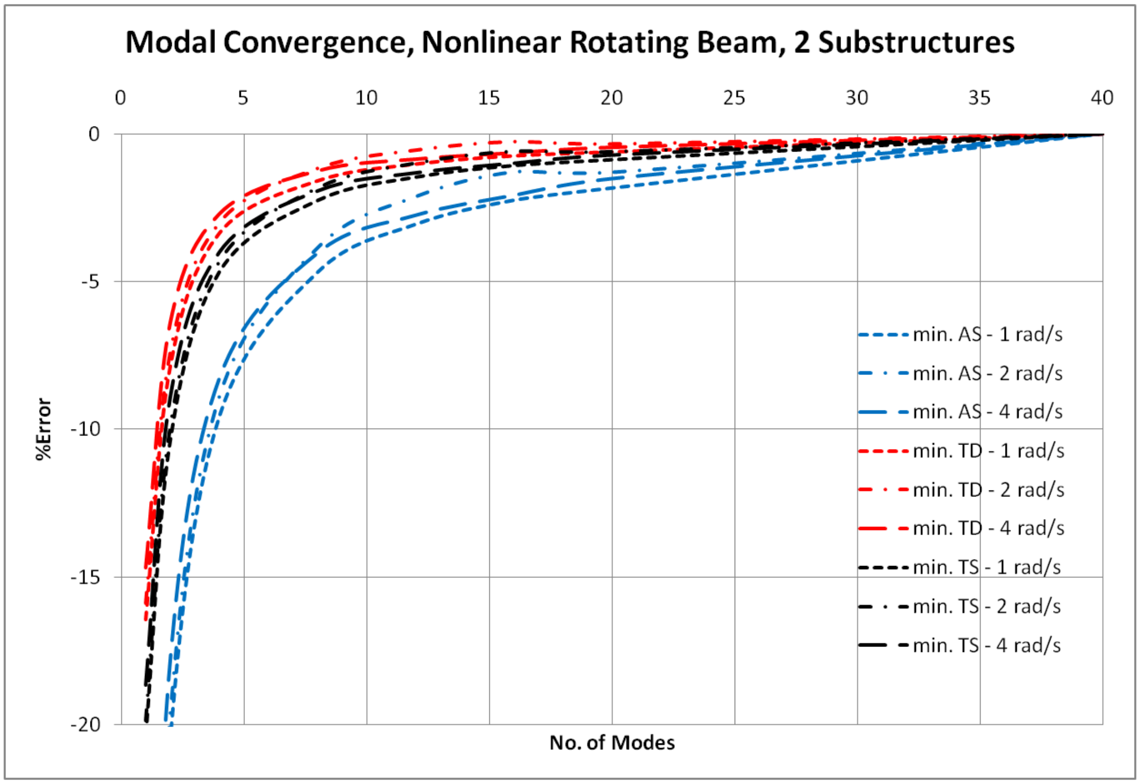

Figure 60: Modal Convergence, Nonlinear Rotating Beam, 2 Substructures

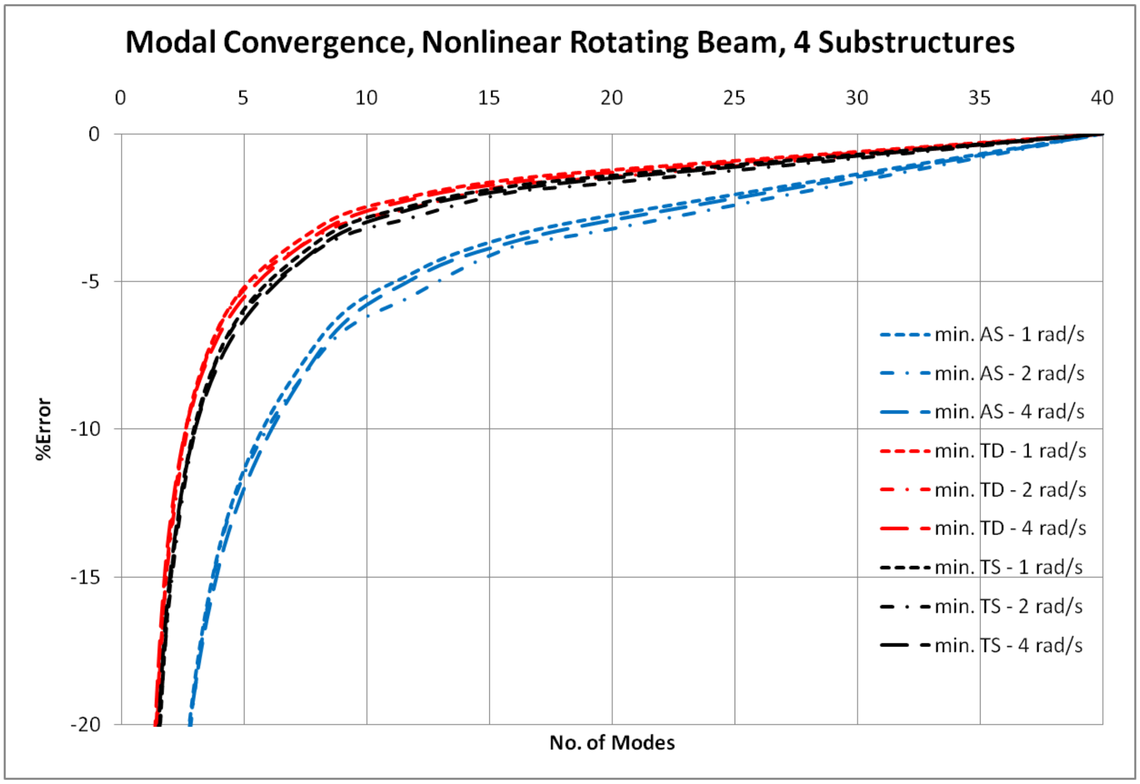

Figure 61: Modal Convergence, Nonlinear Rotating Beam, 4 Substructures

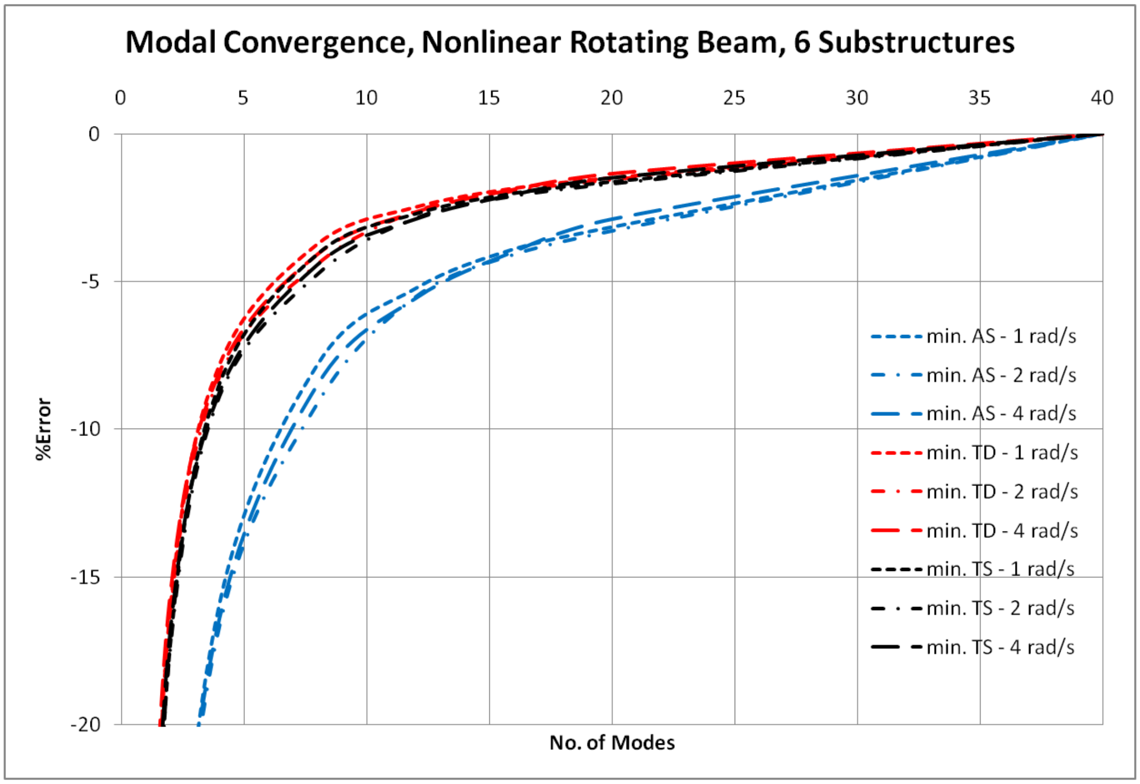

Figure 62: Modal Convergence, Nonlinear Rotating Beam, 6 Substructures

Computational Time of Nonlinear Models at Different Number of Substructures

Increasing the number of modes and/or substructures will lead to an increase in the computational time. This increase becomes more pronounced at larger number of modes and at larger number of substructures.

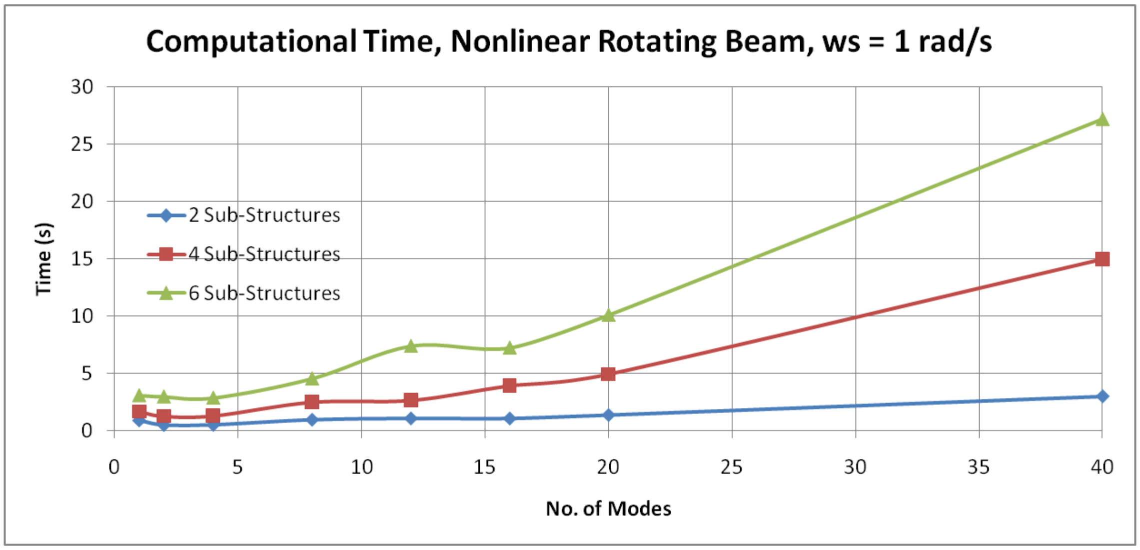

Figure 63: Computational Time, Nonlinear Rotating Beam, ω_s = *1 rad/s*

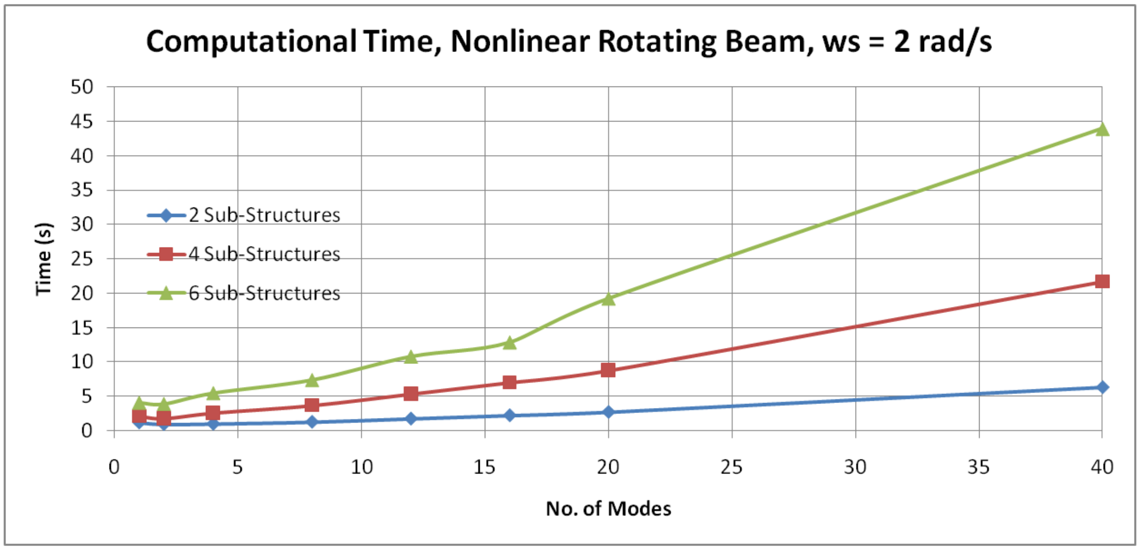

Figure 64: Computational Time, Nonlinear Rotating Beam, ω_s = *2 rad/s*

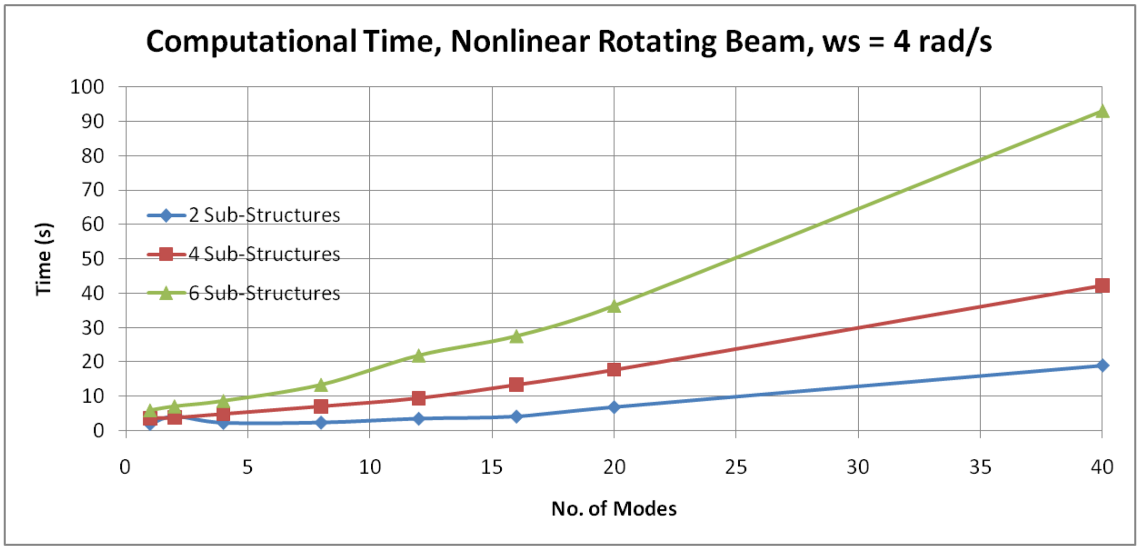

Figure 65: Computational Time, Nonlinear Rotating Beam, ω_s = *4 rad/s*

Computational Time of Nonlinear Models at Different ω_s

A higher ω_s will lead to an increase in the computational time. This increase becomes more pronounced at higher ω_s and larger number of modes.

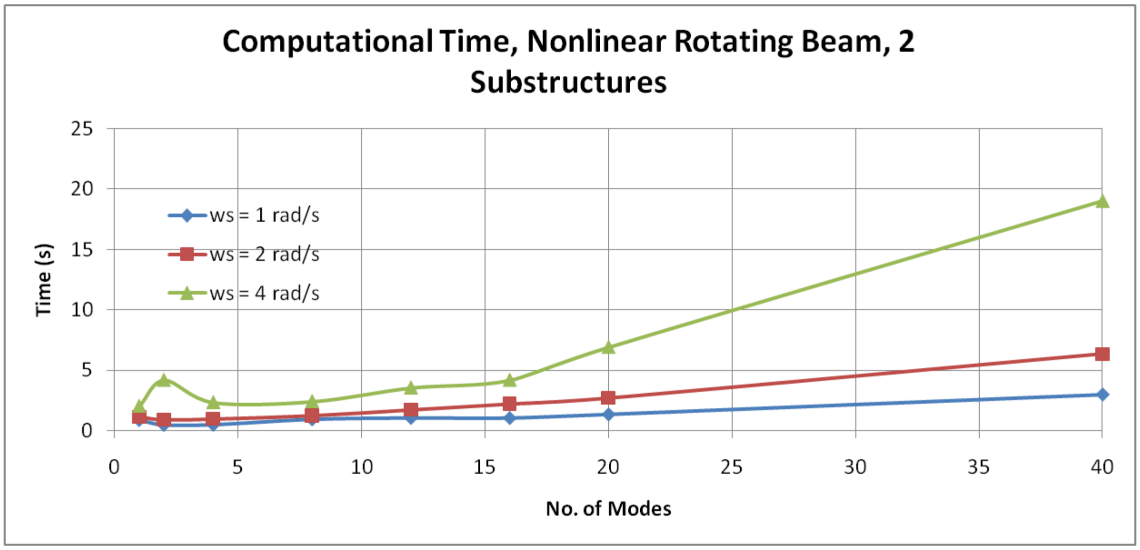

Figure 66: Computational Time, Nonlinear Rotating Beam, 2 Substructures

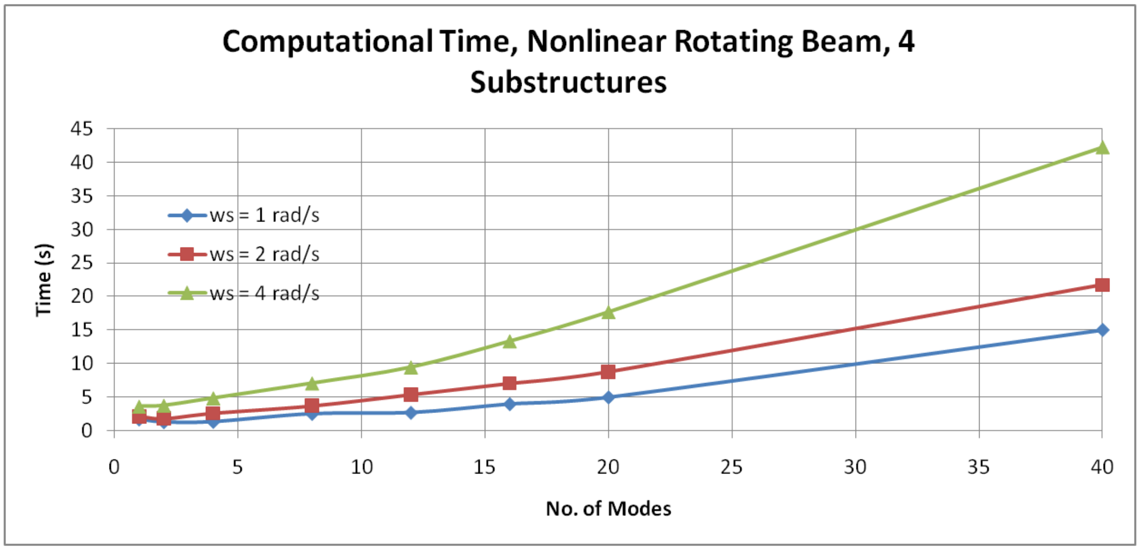

Figure 67: Computational Time, Nonlinear Rotating Beam, 4 Substructures

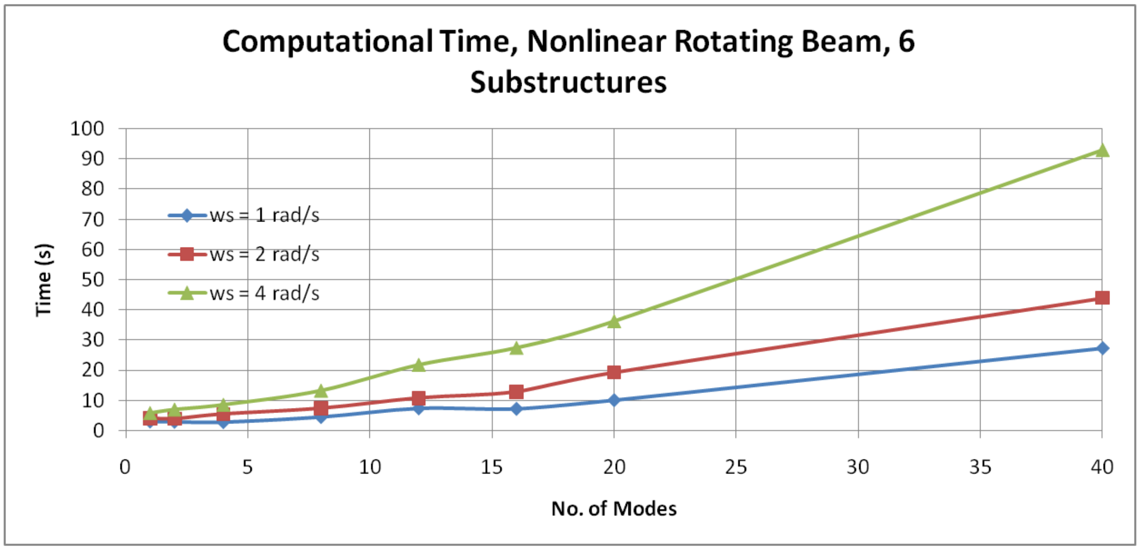

Figure 68: Computational Time, Nonlinear Rotating Beam, 6 Substructures

7.8. Structural Damping

In this subsection, the effect of the value of structural damping in the form of modal damping on the solution of the rotating beam will be investigated.

The six substructures, 10 modes, $\omega_s = 4\ rad/s$ case is discussed. Comparisons are made based on the percentage difference between the solutions at the current modal damping ratio and no damping. The time histories of the axial shortening, tip deflection and tip slope are plotted in Figure 69, Figure 70 and Figure 71 respectively. The percentage differences of the minimum tip displacements for the different modal damping values used are plotted in Figure 72. Figure 73 plots the computation times required for the different modal damping values used.

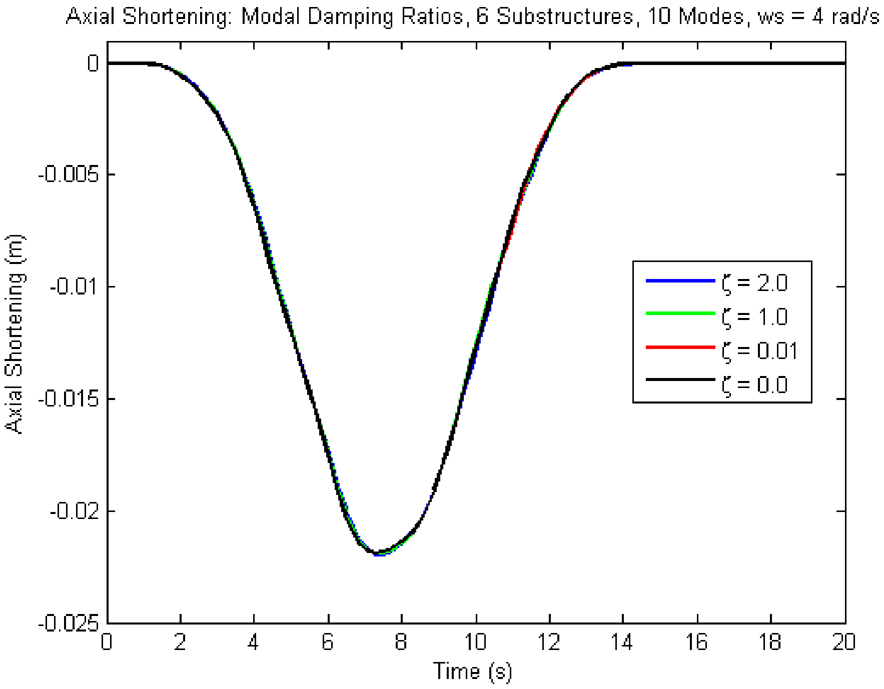

Figure 69: Time History of Axial Shortening, Modal Damping Ratios, 6 Substructures, 10 Modes, ω_s = 4 rad/s

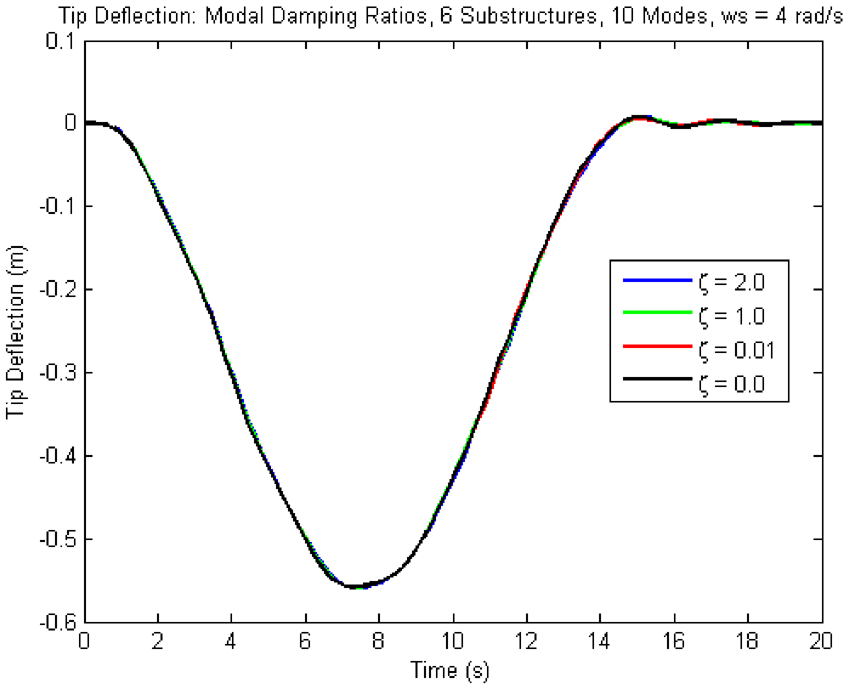

Figure 70: Time History of Tip Deflection, Modal Damping Ratios, 6 Substructures, 10 Modes, ω_s = *4 rad/s*

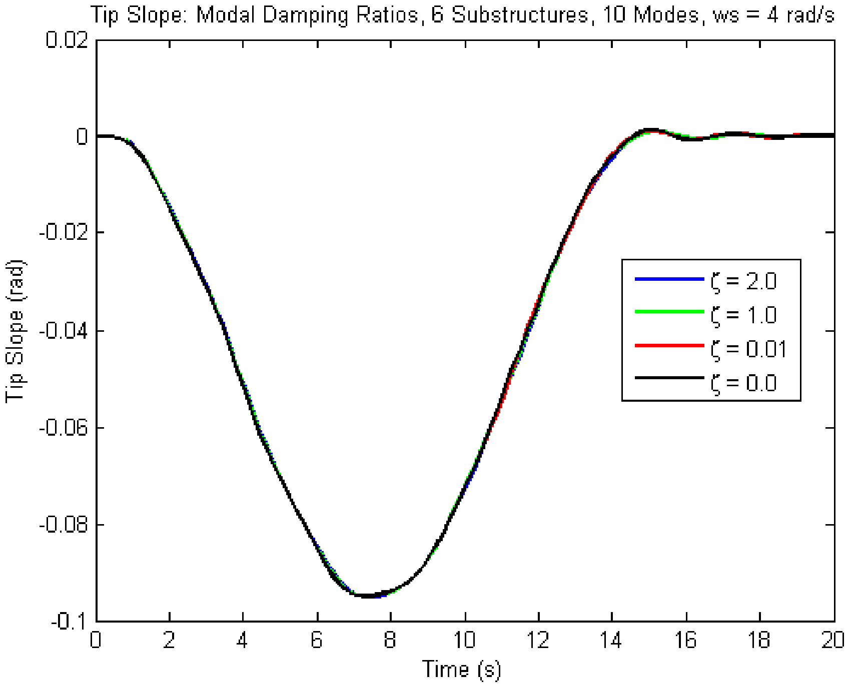

Figure 71: Time History of Tip Slope, Modal Damping Ratios, 6 Substructures, 10 Modes, ω_s = *4 rad/s*

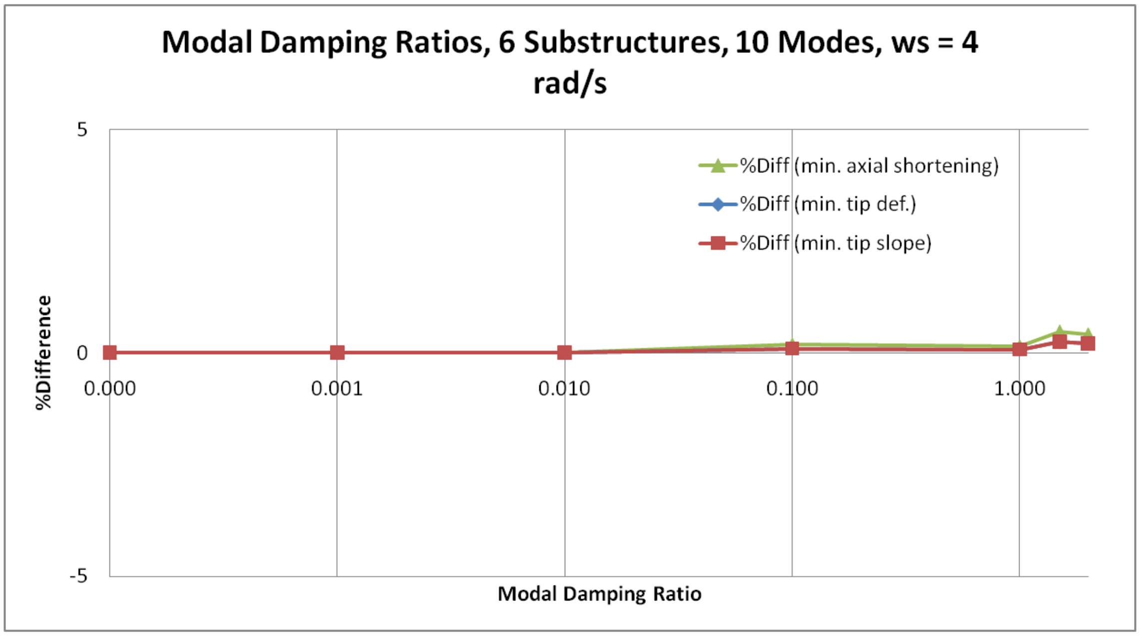

Figure 72: Modal Damping Ratios, 6 Substructures, 10 Modes, ω_s = *4 rad/s*

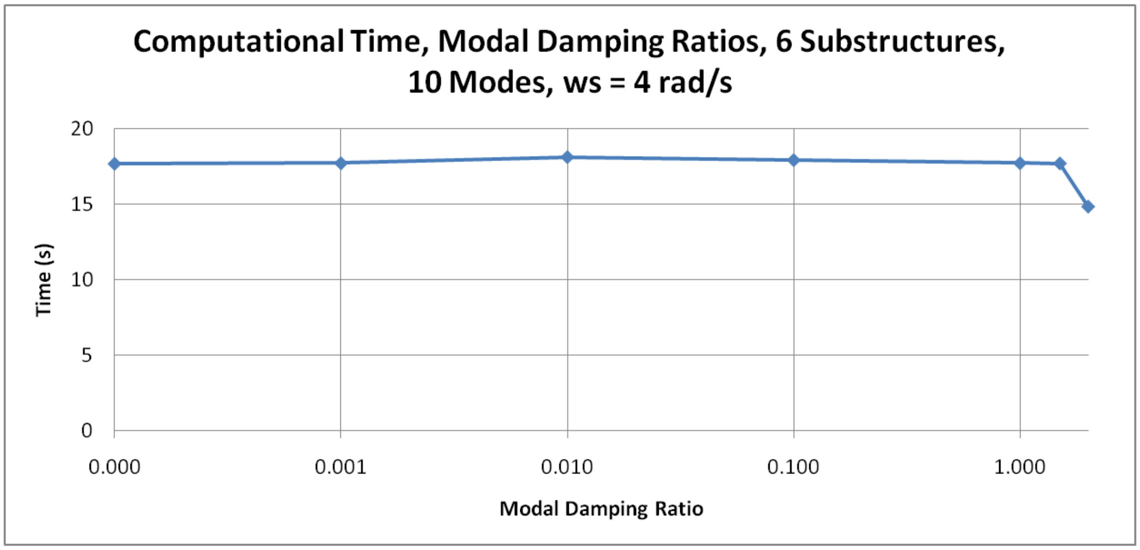

Figure 73: Computational Time, Damping Ratios, 6 Substructures, 10 Modes, ω_s = *4 rad/s*

There are virtually no differences in the solutions when different modal damping ratios are applied. This is also the observation made for the computational times required.

Modal damping can be applied to ensure success in solving the numerical solutions when there are evidently high frequency vibrations as the beam returns to its mean position after passing the minimum deflection point. This occurs approximately at the 12 to 20 seconds portion of the simulation run. An example is the 6 substructures, 10 modes, ω_s = *8 rad/s* case. The time increment at the 13.71651 seconds mark becomes excessively small and the solution is not able to proceed when zero modal damping is prescribed. A successful solution is achieved when a modal damping ratio of 0.01 is applied. There are also other similar instances but will not be presented here. Also, no further investigation will be carried out. This is because the specification of modal damping for this purpose is rather a trial and error type of problem.

7.9. Modal Acceleration

In this subsection, the modal acceleration technique discussed in subsection 3.5 will be applied. The six substructures, 10 modes and 40 modes, $\omega_s = 4\ rad/s$ cases are discussed. Only the proportion of fully coupled and decoupled modes within the total number of modes is varied, i.e. the total number of modes remains the same. The errors are measured as the percentage difference between the solutions at the current number of fully coupled modes (the rest of the modes are decoupled) and the full set of coupled modes (no decoupled modes).

Figure 74 and Figure 76 plot the errors and computational times required for the 10 mode case respectively. And, Figure 75 and Figure 77 plot for the 40 mode case.

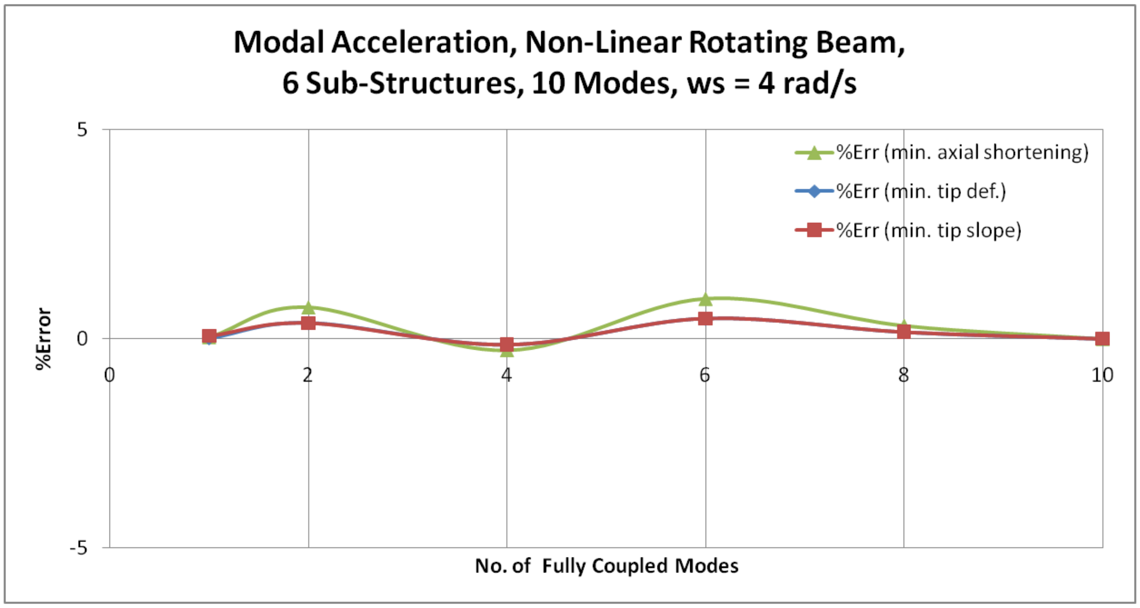

Figure 74: Modal Acceleration, Nonlinear Rotating Beam, 6 Substructures, 10 Modes, $\omega_s = 4\ rad/s$

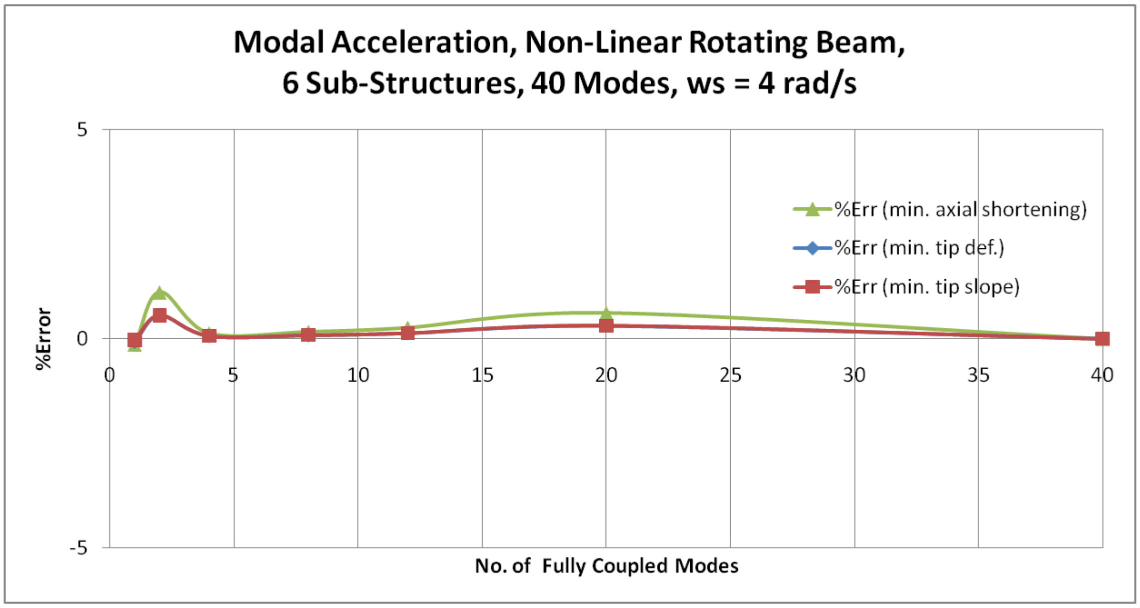

Figure 75: Modal Acceleration, Nonlinear Rotating Beam, 6 Substructures, 40 Modes, ω_s = *4 rad/s*

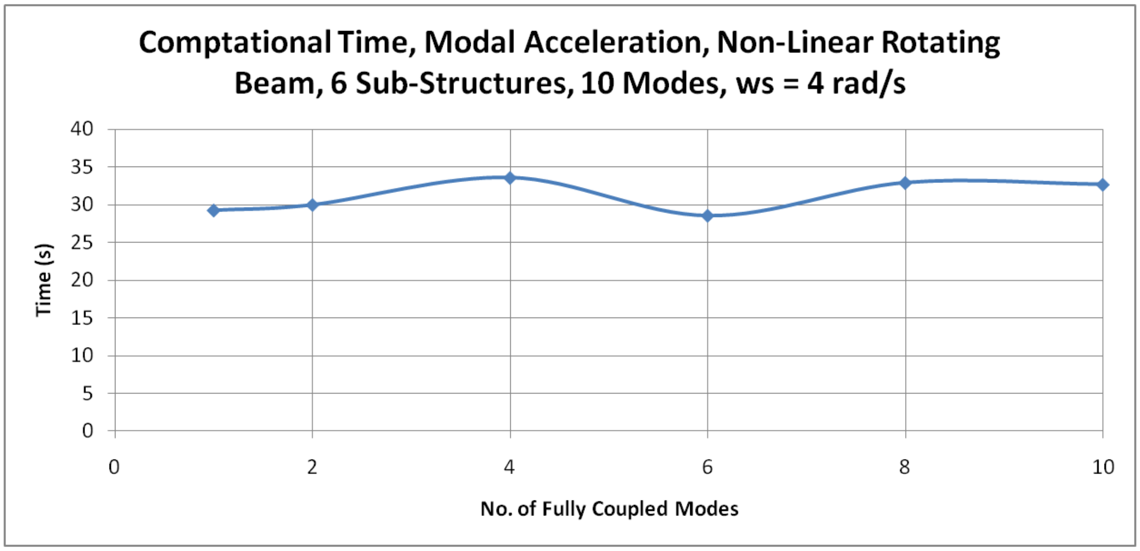

Figure 76: Computational Time, Modal Acceleration, Nonlinear Rotating Beam, 6 Substructures, 10 Modes, ω_s = *4 rad/s*

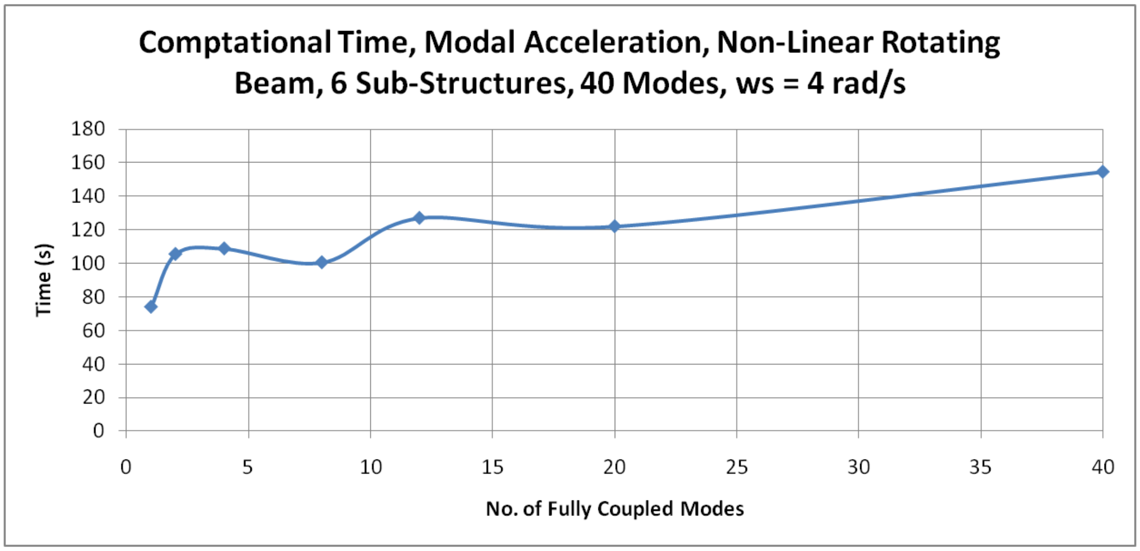

Figure 77: Computational Time, Modal Acceleration, Nonlinear Rotating Beam, 6 Substructures, 40 Modes, ω_s = *4 rad/s*

There are virtually no differences in the solutions when the proportion of fully coupled modes is increased. This strongly suggests that only the first mode is dominantly coupled to the rigid body motions and other elastic modes. Increasing the number of fully coupled modes and at the same time keeping the total number of modes constant does not improve the results. The results are improved by specifying a larger total number of modes (subsection 7.7).

Changing the proportion of fully coupled and decoupled modes for the 10 modes case does not adversely affect the computational time required. However, for the 40 modes case, increasing the number of fully coupled modes significantly increases the computational times required. There is significant computational time savings from using less fully coupled modes. The explanation for this is as follow. For the 10 modes case, the computational time savings from the size reduction of the square matrix inversion in the first line in equation (3.36) is not significant as compared to the computational time required for other parts of the computation. However, for the 40 modes case, the benefits are higher as the original square matrix to reduce from is much larger; 43x43 vs. 13x13.

THIS PAGE INTENTIONALLY LEFT BLANK.

8. Extension of IC Beam to Include Axial Modes

The IC beam formulation presented in section 3 does not include axial modes. The assumption is that axial deformations are small and thus neglected. The validity of this assumption is investigated here where the IC beam is extended to include axial modes and numerical tests performed to observe the effect of including axial modes.

8.1. IC Beam with Axial Modes Formulation

In this subsection, the extension of the IC beam formulation to include axial modes will be presented. The procedure of deriving the equations follows from section 3 and will not be repeated here. Only the key equations and formulations will be highlighted.

Consider the new IC beam substructure with axial modes in Figure 78. Notice that a point P_0 on the beam in the un-deformed state will move to point P after deformation.

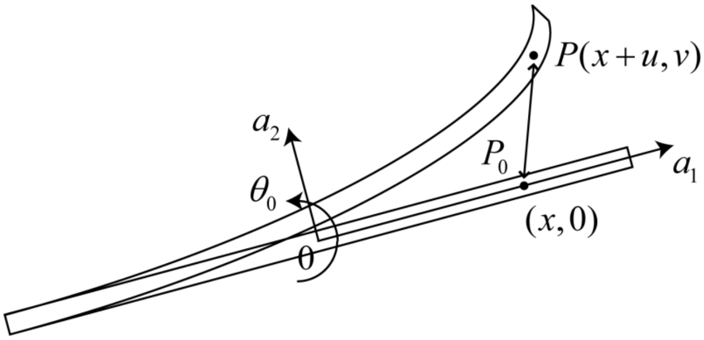

Figure 78: 2D Planar IC Beam Substructure with Axial Modes

With reference to equations (3.1) to (3.3), the velocity of point P is:

$$\vec{V}_P = \left(\dot{x}_0 - v\dot{\theta}_0 + \dot{u}\right)\vec{a}_1 + \left(\dot{y}_0 + \left(x+u\right)\dot{\theta}_0 + \dot{v}\right)\vec{a}_2 \tag{8.1}$$

With reference to equation (3.6), i.e. using the method of assumed mode shapes:

$$u = \sum_{j=1}^{N_u} X_j u_j, \quad \dot{u} = \sum_{j=1}^{N_u} X_j \dot{u}_j$$
$$v = \sum_{k=1}^{N_k} Y_k v_k, \quad \dot{v} = \sum_{k=1}^{N_k} Y_k \dot{v}_k \tag{8.2}$$

With reference to equations (3.4) to (3.13), the kinetic energy of the IC beam is:

$$
\begin{aligned}
T = {} & \frac{1}{2}M\dot{x}_0^2 + \frac{1}{2}M\dot{y}_0^2 + \frac{1}{2}J_0\dot{\theta}_0^2 \\
& + \sum_{j=1}^{N_u} \bar{m}_{u,j} u_j \dot{y}_0 \dot{\theta}_0 + \sum_{j=1}^{N_u} \bar{m}_{xu,j} u_j \dot{\theta}_0^2 + \frac{1}{2}\sum_{j=1}^{N_u} \bar{m}_{uu,j} u_j^2 \dot{\theta}_0^2 \\
& + \sum_{j=1}^{N_u} \bar{m}_{u,j} \dot{u}_j \dot{x}_0 + \frac{1}{2}\sum_{j=1}^{N_u} \bar{m}_{uu,j} \dot{u}_j^2 \\
& - \sum_{k=1}^{N_v} \bar{m}_{v,k} v_k \dot{x}_0 \dot{\theta}_0 + \frac{1}{2}\sum_{k=1}^{N_v} \bar{m}_{vv,k} v_k^2 \dot{\theta}_0^2 \\
& + \frac{1}{2}\sum_{k=1}^{N_v} \bar{m}_{vv,k} \dot{v}_k^2 + \sum_{k=1}^{N_v} \bar{m}_{v,k} \dot{v}_k \dot{y}_0 + \sum_{k=1}^{N_v} \bar{m}_{vx,k} \dot{v}_k \dot{\theta}_0
\end{aligned}
\tag{8.3}
$$

Where,

$$
\begin{aligned}
&\bar{m}_{u,j} = \int_{-\frac{L}{2}}^{\frac{L}{2}} mX_j\,dx, \quad \bar{m}_{uu,j} = \int_{-\frac{L}{2}}^{\frac{L}{2}} mX_j^2\,dx, \quad \bar{m}_{xu,j} = \int_{-\frac{L}{2}}^{\frac{L}{2}} mxX_j\,dx \\
&\bar{m}_{v,k} = \int_{-\frac{L}{2}}^{\frac{L}{2}} mY_k\,dx, \quad \bar{m}_{vv,k} = \int_{-\frac{L}{2}}^{\frac{L}{2}} mY_k^2\,dx, \quad \bar{m}_{xv,k} = \int_{-\frac{L}{2}}^{\frac{L}{2}} mxY_k\,dx
\end{aligned}
\tag{8.4}
$$

With reference to equations (3.14) to (3.15), the potential energy of the IC beam is:

$$
V = \frac{1}{2}\sum_{j=1}^{N_u} \bar{k}_{u,j} u_j^2 + \frac{1}{2}\sum_{k=1}^{N_v} \bar{k}_{v,k} v_k^2
\tag{8.5}
$$

Where,

$$
\begin{aligned}
\bar{k}_{u,j} &= \int_{-\frac{L}{2}}^{\frac{L}{2}} EA\left(X_j'\right)^2 dx \\
\bar{k}_{v,k} &= \int_{-\frac{L}{2}}^{\frac{L}{2}} EI\left(Y_k''\right)^2 dx
\end{aligned}
\tag{8.6}
$$

With reference to subsection 3.1.3 and 3.2 and considering two axial modes and two edgewise bending modes, the equations relating momentum and velocities are:

$$
\begin{bmatrix} P_{x_0} \\ P_{y_0} \\ P_{\theta_0} \\ P_{u_1} \\ P_{u_2} \\ P_{v_1} \\ P_{v_2} \end{bmatrix}
=
\begin{bmatrix}
M & 0 & A_{13} & \bar{m}_{u,1} & \bar{m}_{u,2} & 0 & 0 \\
0 & M & A_{23} & 0 & 0 & \bar{m}_{v,1} & \bar{m}_{v,2} \\
A_{31} & A_{32} & A_{33} & 0 & 0 & \bar{m}_{xv,1} & \bar{m}_{xv,2} \\
\bar{m}_{u,1} & 0 & 0 & \bar{m}_{uu,1} & 0 & 0 & 0 \\
\bar{m}_{u,2} & 0 & 0 & 0 & \bar{m}_{uu,2} & 0 & 0 \\
0 & \bar{m}_{v,1} & \bar{m}_{xv,1} & 0 & 0 & \bar{m}_{vv,1} & 0 \\
0 & \bar{m}_{v,2} & \bar{m}_{xv,2} & 0 & 0 & 0 & \bar{m}_{vv,2}
\end{bmatrix}
\begin{bmatrix} \dot{x}_0 \\ \dot{y}_0 \\ \dot{\theta}_0 \\ \dot{u}_1 \\ \dot{u}_2 \\ \dot{v}_1 \\ \dot{v}_2 \end{bmatrix}
\tag{8.7}
$$

Where,

$$
\begin{aligned}
A_{13} &= A_{31} = -\bar{m}_{v,1}v_1 - \bar{m}_{v,2}v_2 \\
A_{23} &= A_{32} = \bar{m}_{u,1}u_1 + \bar{m}_{u,2}u_2 \\
A_{33} &= J_0 + 2\bar{m}_{xu,1}u_1 + \bar{m}_{uu,1}u_1^2 \\
&\quad +2\bar{m}_{xu,2}u_2 + \bar{m}_{uu,2}u_2^2 \\
&\quad +\bar{m}_{vv,1}v_1^2 \\
&\quad +\bar{m}_{vv,2}v_2^2
\end{aligned}
\tag{8.8}
$$

And the remaining of the equations required for the IC beam implementation is:

$$
\begin{aligned}
e'_{x_0} &= M\dot{y}_0\dot{\theta}_0 + \left(\bar{m}_{u,1}u_1 + \bar{m}_{u,2}u_2\right)\dot{\theta}_0^2 + \left(\bar{m}_{v,1}\dot{v}_1 + \bar{m}_{v,2}\dot{v}_2\right)\dot{\theta}_0 \\
e'_{y_0} &= -M\dot{x}_0\dot{\theta}_0 - \left(\bar{m}_{u,1}\dot{u}_1 + \bar{m}_{u,2}\dot{u}_2\right)\dot{\theta}_0 + \left(\bar{m}_{v,1}v_1 + \bar{m}_{v,2}v_2\right)\dot{\theta}_0^2 \\
e'_{\theta} &= 0 \\
e'_{u_j} &= \bar{m}_{v,j}\dot{y}_0\dot{\theta}_0 + \left(\bar{m}_{xu,j} + \bar{m}_{u\ uj}u_j\right)\dot{\theta}_0^2 - \bar{k}_{u,j}u_j \qquad ;\, j = 1,2 \\
e'_{v_j} &= -\bar{m}_{v,j}\dot{x}_0\dot{\theta}_0 + \bar{m}_{vv,j}v_j\dot{\theta}_0^2 - \bar{k}_{v,j}v_j \qquad ;\, j = 1,2
\end{aligned}
\tag{8.9}
$$

Equations (8.7) and (8.9) are crucial parts of the final equations required for the IC beam implementation shown in equation (3.36). The bond graph model of the IC beam with axial modes is similar to the model with two bending modes as illustrated in Figure 3. The only modification is that two new axial modes generalized variables are added. This modification is straight forward and will not be presented. Also notice that the rigid body motions, axial and bending deformations are nonlinearly coupled in the formulation. However the elastic deformations within the substructure are still linear and described by modal superposition.

All but except the bond graph component model presented in subsection 4.2.1 remain useable. The component model that performs coordinate transformation from the IC beam origin to the right end of the beam requires modification (Figure 8). This modification is straight forward and will not be presented. Also, the equations (4.4) and (4.5) need to be modified as follow:

$$
\begin{aligned}
\dot{x}_2 &= \dot{x}_0 + \sum_{j=1}^{2} X_j\left(\frac{L}{2}\right)\dot{u}_j \\
\dot{y}_2 &= \dot{y}_0 + \frac{L}{2}\dot{\theta}_0 + \sum_{k=1}^{2} Y_k\left(\frac{L}{2}\right)\dot{v}_k \\
\dot{\theta}_2 &= \dot{\theta}_0 + \sum_{k=1}^{2} Y'_k\left(\frac{L}{2}\right)\dot{v}_k
\end{aligned}
\tag{8.10}
$$

$$
\begin{aligned}
F_{x_0,2} &= F_{x_2} \\
F_{y_0,2} &= F_{y_2} \\
F_{\theta_0,2} &= F_{\theta_2} + \frac{L}{2} F_{y_2} \\
F_{u_j,2} &= X_j\left(\frac{L}{2}\right)F_{x_2} && ,\, j = 1,2 \\
F_{v_k,2} &= Y_k\left(\frac{L}{2}\right)F_{y_2} + Y_k'\left(\frac{L}{2}\right)F_{\theta_2} && ,\, k = 1,2
\end{aligned}
\tag{8.11}
$$

8.2. Effect of Including Axial Modes

In this subsection, the effect of including axial modes is investigated in detail. The number of axial modes is varied (0 to 10) at different number of substructures (1, 2, 4, 6 and 8) for the different ω_s cases (*1, 2, 4 and 8 rad/s*). All cases employ 10 bending modes. The errors are measured as the percentage difference between the solutions at the current number of axial modes employed and when 10 axial modes are employed.

The results from one linear case (1 substructure, ω_s = *1 rad/s*) and one nonlinear case (8 substructures, ω_s = *8 rad/s*) are presented. The portion of axial shortening time history near to the steady state region for the nonlinear case is also presented in Figure 83. Note that m_{axial} denotes the number of axial modes employed.

Results from Linear Case

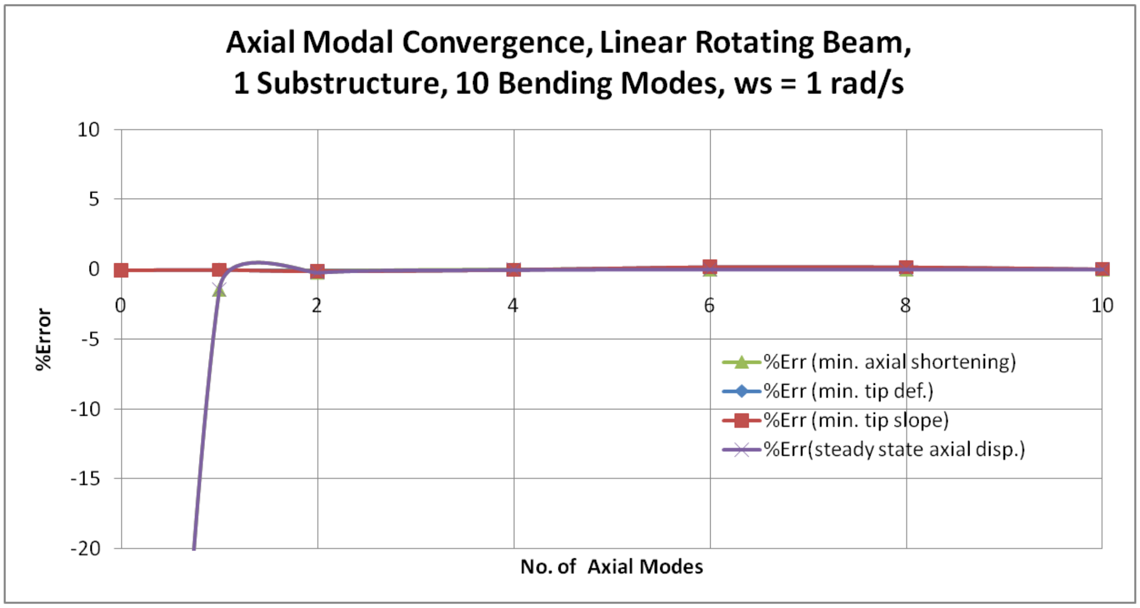

Figure 79: Axial Modal Acceleration, Linear Rotating Beam, 1 Substructure, 10 Bending Modes, ω_s = *1 rad/s*

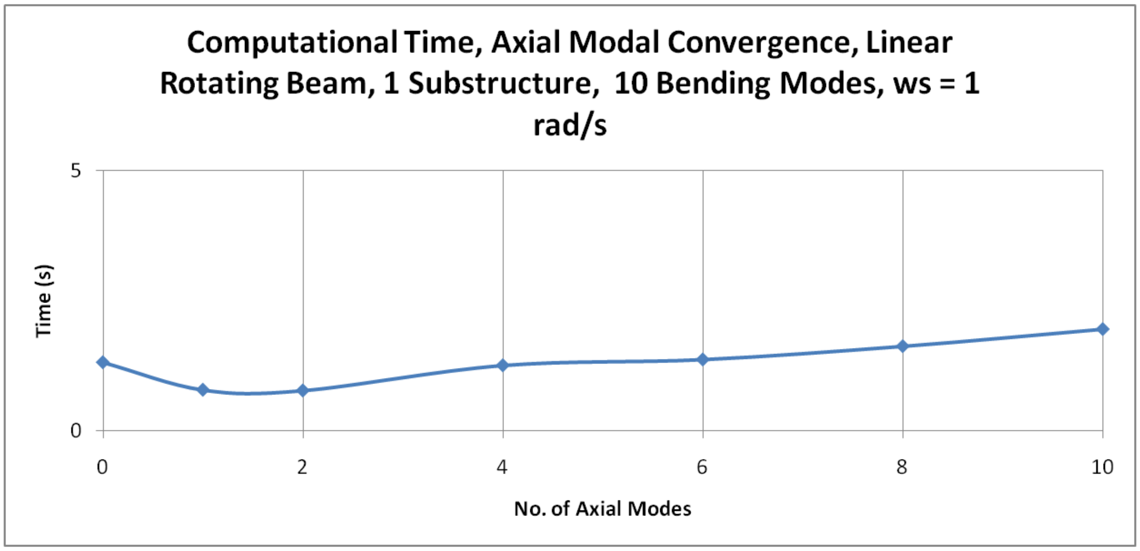

Figure 80: Computational Time, Axial Modal Convergence, Nonlinear Rotating Beam, 1 Substructure, 10 Bending Modes, ω_s = *1 rad/s*

Results from Nonlinear Case

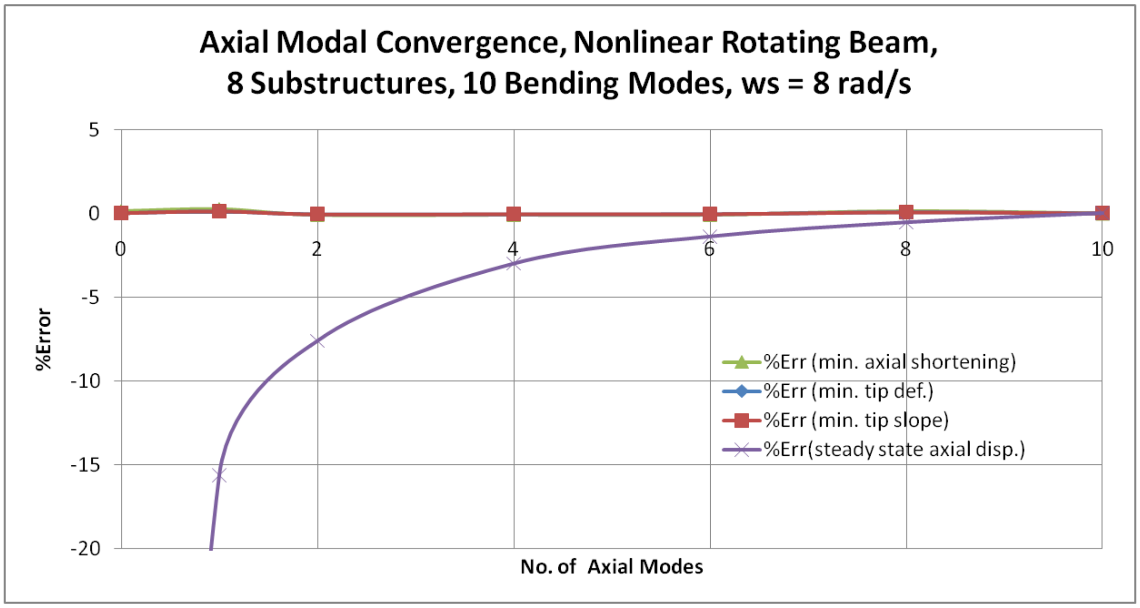

Figure 81: Axial Modal Acceleration, Nonlinear Rotating Beam, 8 Substructures, 10 Bending Modes, $\omega_s = 8$ rad/s

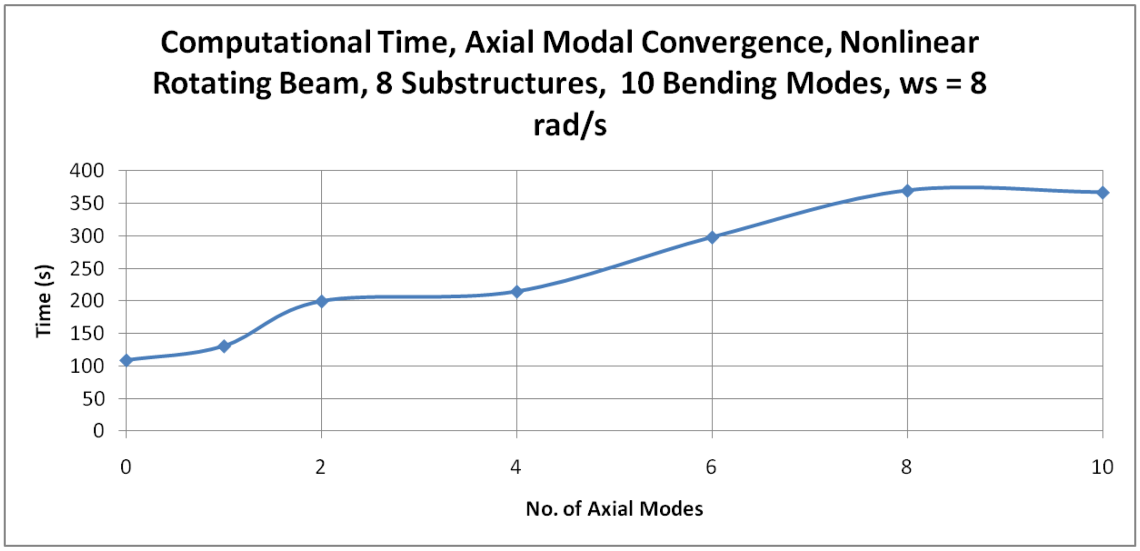

Figure 82: Computational Time, Axial Modal Convergence, Nonlinear Rotating Beam, 8 Substructures, 10 Bending Modes, $\omega_s = 8$ rad/s

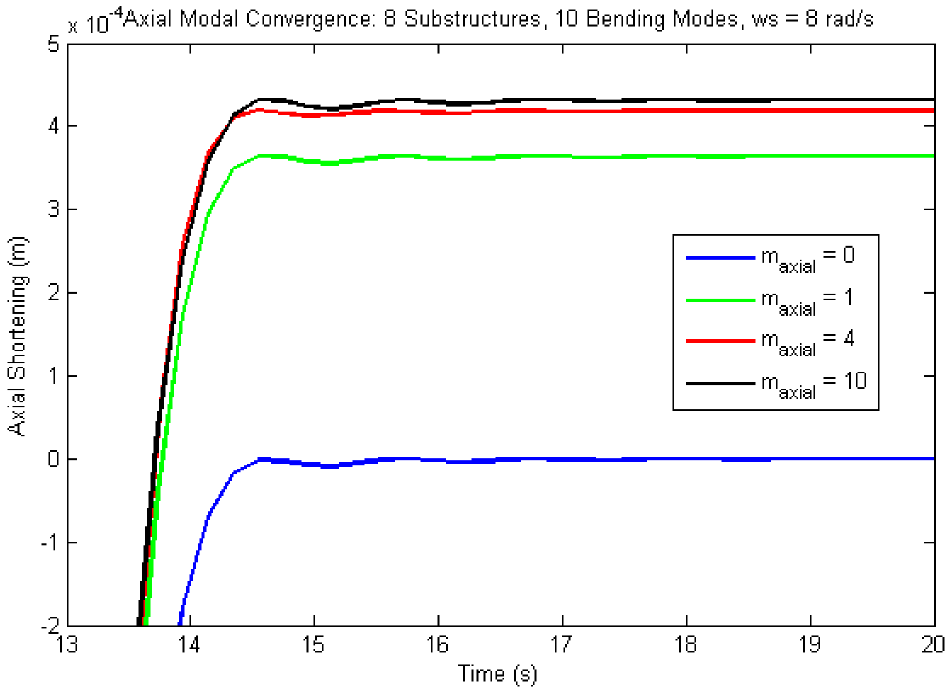

Figure 83: Time History of Axial Shortening, Axial Modal Convergence, 8 Substructures, 10 Bending Modes, ω_s = *8 rad/s*

Including axial modes do not improve the results. The time histories of the axial shortening, tip deflection and tip slope remain virtually unchanged as compared to when no axial modes are included. The only benefit is the steady state axial tip displacements are correctly modeled when axial modes are used. Obviously there are steady state tip axial displacements only when axial modes included. However, these displacements are small and might not be as essential as compared to the minimum axial shortening and tip deflections. For example, for 8 substructures and ω_s = *8 rad/s* case, the steady state axial tip displacement is 0.000432 m while the minimum axial shortening is 0.08804m, i.e. factor of 200 times larger. The minimum tip deflection is 1.11m which is a factor of 2600 times larger. Therefore, in the author’s opinion, the incentive for including axial modes for the rotating beam spin-up maneuver case is rather small and does not justify the additional computational times required.

The axial modal convergence for the steady state axial displacement in the linear case is significantly faster than for the nonlinear case. Using one axial mode in the linear case is sufficient to achieve converged solutions, however about 3 to 4 axial modes are required in the nonlinear case to achieve below 5% errors. Recall that this is similar to the modal convergence results presented in subsection 7.7; just one bending mode is required for convergence in the linear case and about 10 and 15 bending modes are required to achieve below 5% errors for the minimum tip deflection and slope and minimum axial shortening respectively. Also, the computational time required increases significantly for nonlinear cases, particularly for the higher number of substructures cases.

9. More Investigations into the Interconnecting Hinges

In sections 7 and 8, the IC beam substructures were connected using the Karnopp-Margolis method [1], i.e. using springs (capacitor elements). In subsections 4.2.1.3 and 0, dampers (resistor elements) were also included in the component models for the rotating hinge and interconnecting hinge but their resistance values (denoted '*R_hinge*') are set equal to zero. It was also presented in subsection 7.3 that the stiffness values of these springs (denoted '*k_hinge*') must be large. Too small a value will lead to extremely long computational times. Also, larger *k_hinge* values require more computational efforts.

In this section, the previously unutilized dampers will be used. Using dampers in place of springs will still ensure that the system stays in complete integral causality. However, dampers do not relate as well as springs to the physical problem; springs are the natural interfaces between the multibodies. Furthermore, dampers dissipate energy away from the system. While using dampers do not seem to be the correct representation of physical problem, it is still interesting to investigate their use. The reason is that using dampers in place of springs will not introduce any additional high stiffness terms and state variables into the system. Also using a combination of dampers and springs allows the use of a lower *k_hinge* value. This yields significant benefits in the computational efforts required.

The six substructures, 10 modes, $\omega_s = 4\ rad/s$ case is discussed. The solution when *R_hinge = 0* and *k_hinge = 1e10* is used is taken to be the converged solution.

9.1. *k_hinge = 0* and Varying *R_hinge*

In this subsection, *R_hinge* is varied from 1e1 to 1e10. The errors are measured as the percentage difference between the solutions at the current *R_hinge* and the converged solution, i.e. *R_hinge = 0* and *k_hinge = 1e10*.

The time histories of the axial shortening, tip deflection and tip slope are plotted in Figure 84, Figure 85 and Figure 86, and Figure 87 respectively. The percentage errors of the minimum tip displacements for the different R_hinge values used are plotted in Figure 88. Figure 89 plots the computation times required for the different *R_hinge* values used.

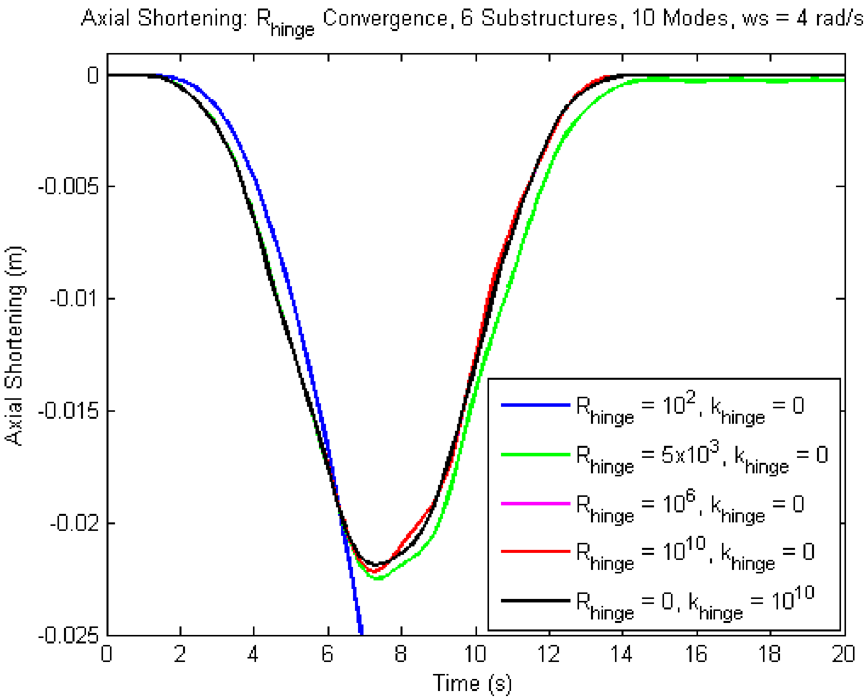

Figure 84: Time History of Axial Shortening, *R_hinge* Convergence, 6 Substructures, 10 Modes, ω_s = *4 rad/s*

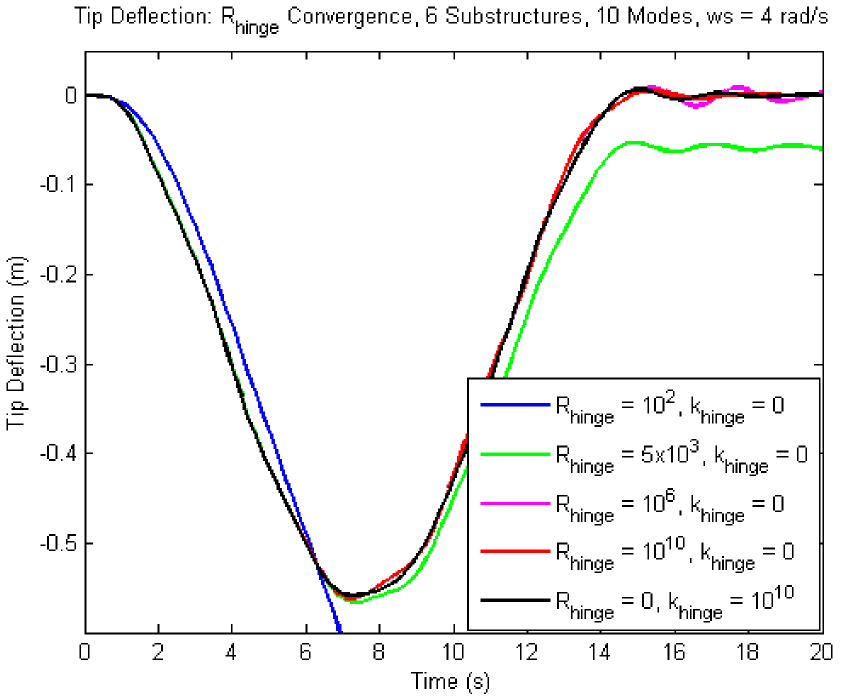

Figure 85: Time History of Tip Deflection (1), *R_hinge* Convergence, 6 Substructures, 10 Modes, ω_s = *4 rad/s*

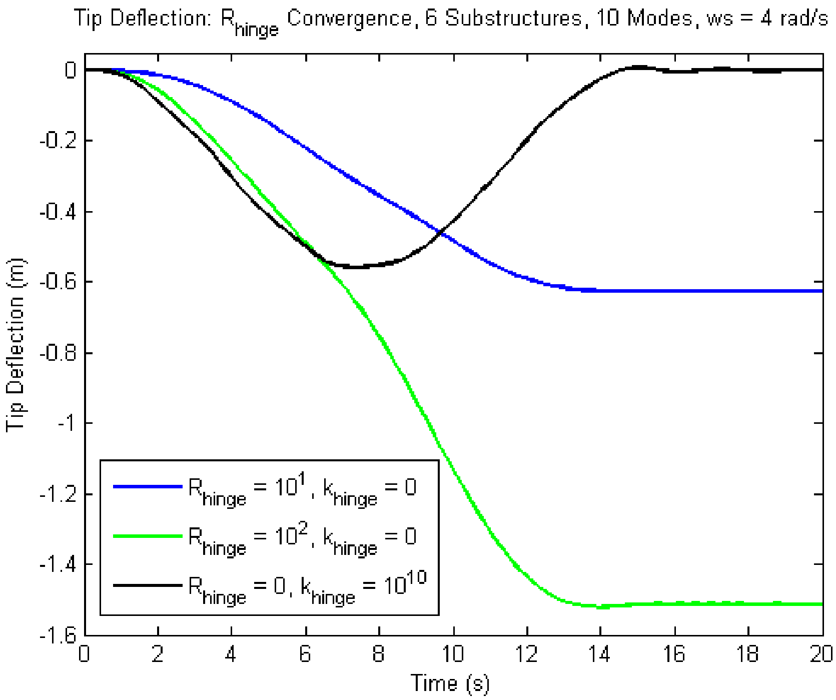

Figure 86: Time History of Tip Deflection (2), *R_hinge* Convergence, 6 Substructures, 10 Modes, ω_s = *4 rad/s*

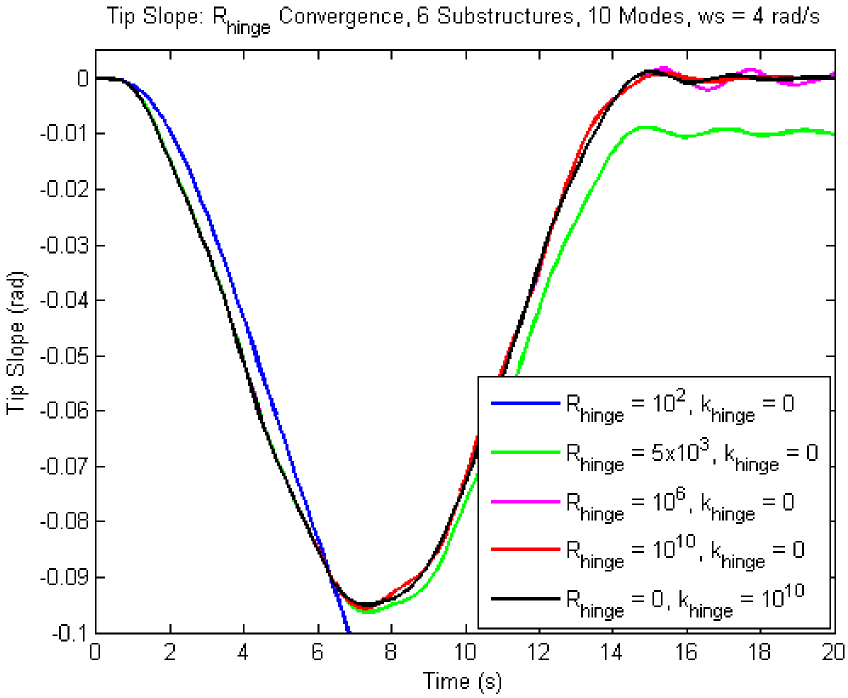

Figure 87: Time History of Tip Slope, *R_hinge* Convergence, 6 Substructures, 10 Modes, ω_s = *4 rad/s*

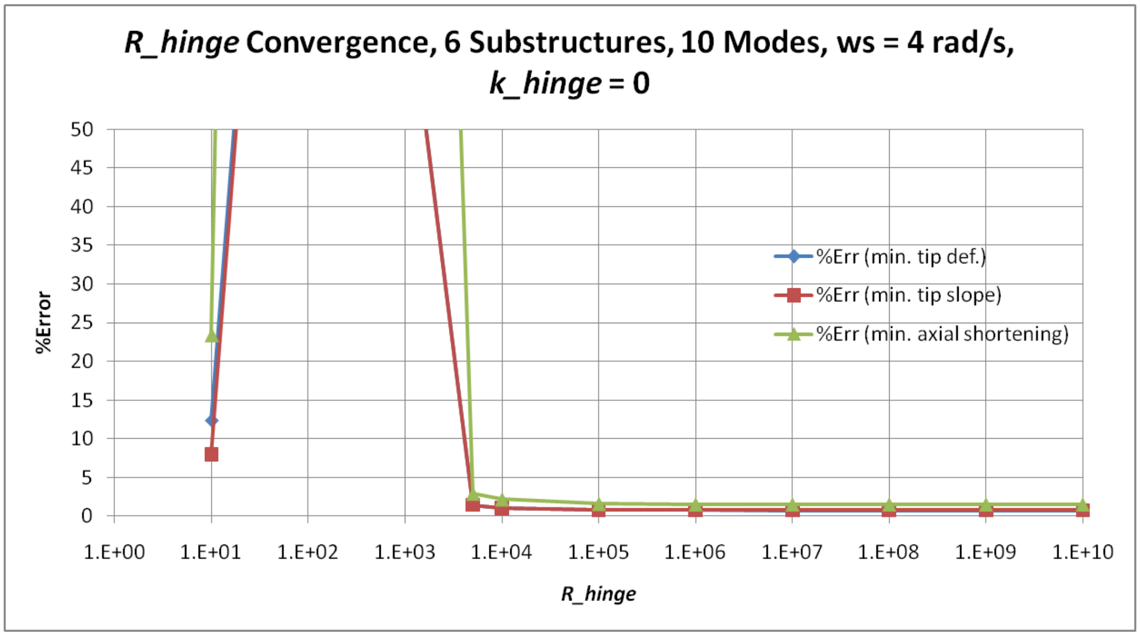

Figure 88: *R_hinge* Convergence, 6 Substructures, ω_s = *4 rad/s, k_hinge = 0*

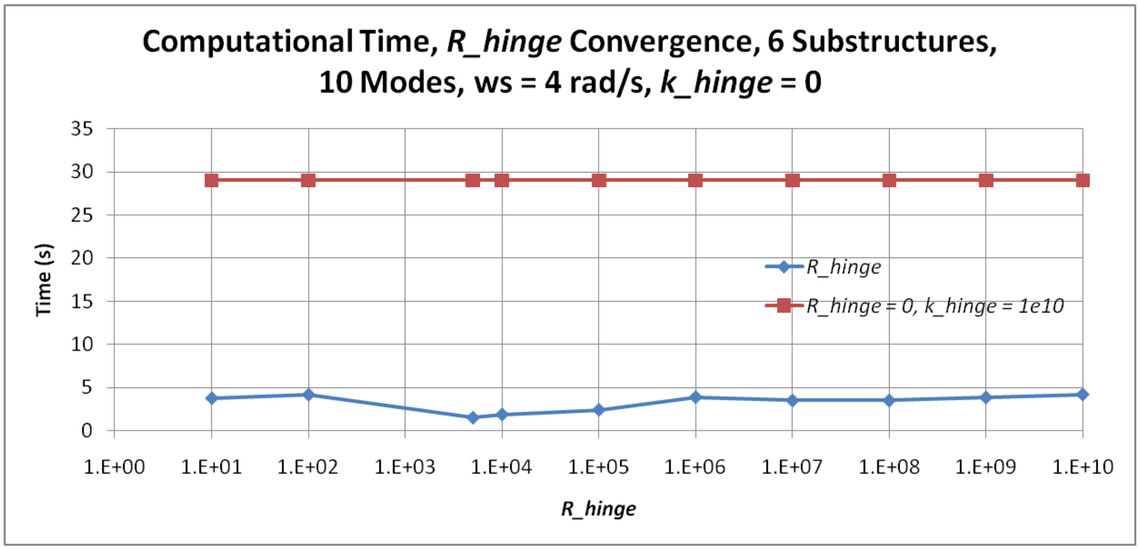

Figure 89: Computational Time, *R_hinge* Convergence, 6 Substructures, ω_s = *4 rad/s, k_hinge = 0*

Using *R_hinge* <= *5e3* lead to erroneous solutions. It is observed in Figure 86 that the tip will be far away from the undeflected position at steady state. This explains the large errors for small *R_hinge* values in Figure 88. In general, accurate minimum tip displacements are obtained when *R_hinge* >= *5e3* is used. However, the steady state tip displacements for *R_hinge* = *5e3* is 0.06m lower than the converged solution. Using *R_hinge* >= *1e6* results in solutions very close to the converged solution for both minimum and steady state tip displacements. However, the minimum tip displacements will not converge to the converged solution for the largest *R_hinge* values; there is consistently a small error. This is about 1.5% for axial shortening and 0.75% for tip deflection and slope. Also the oscillations at steady state die out slower as compared to when *k_hinge = 1e10* is used. This observation is probably unimportant as these small oscillations are not crucial in the spin-up maneuver problem.

Using dampers in place of springs decreases the computational efforts required by a factor of five. Also, using different *R_hinge* values do not affect the computational time required. This was also observed in subsection 7.2 for the case of resistance value of the resistor at the rotating hinge.

9.2. Varying *k_hinge* and Varying *R_hinge*

In this subsection, both *k_hinge* and *R_hinge* are varied from 1e1 to 1e10. The results of the investigations performed in this subsection are presented in Table 6.

Table 6: Summary of Varying *k_hinge* and Varying *R_hinge* Investigation

	***R_hinge* value**		
***k_hinge* value**	Improved computational time	Accurate minimum tip displacements	Accurate steady tip displacements
1e1	1e2	5e3	1e6
1e2	1e2	5e3	1e6
1e3	5e3	5e3	1e6
1e4	1e5	5e3	1e6
1e5	1e6	5e3	1e6
1e6	1e6	5e3	1e6
1e7	1e8	1e6 (Too long computations for *R_hinge < 1e6*)	1e6 (Too long computations for *R_hinge < 1e6*)
1e8	1e8	1e1	1e1
1e9	1e9	0	0
1e10	5e10	0	0

‘Improved computational time’ means the *R_hinge* value above which the computational time required will be below 10 seconds.

‘Accurate minimum tip displacement’ means the *R_hinge* value above which the percentage error in the minimum tip displacements will be below 5%.

‘Accurate steady state tip displacement’ means the *R_hinge* value above which the percentage error in the steady state tip displacements will be less than 0.01m from the converged solution.

When *R_hinge* is specified in combination with *k_hinge*, it was observed that the solution proceeds for small *k_hinge* values. This is in contrast to the results observed in subsection 7.3, where the numerical solution takes an extremely long time to proceed for *k_hinge < 1e9*. To achieve significant savings in computational time, the *R_hinge* value specified will have to be in the order of the same magnitude as the *k_hinge* value used.

For smaller *k_hinge* values, *R_hinge >= 5e3* and *R_hinge >= 1e6* are required to achieve accurate minimum and steady state tip displacements respectively. These are the same *R_hinge* values required in subsection 9.1. For larger *k_hinge* values, no *R_hinge* is required for convergence. In the case of *k_hinge = 1e8*, *R_hinge = 1e1* is required to ensure that the numerical solution proceeds. This suggests that if *k_hinge* is small, the criterion for convergence of the minimum tip displacements will rely on *R_hinge*. Also a small *R_hinge* value can be specified to ensure that the numerical solution proceeds when borderline insufficiently large *k_hinge* values are specified.

The steady state tip oscillations die out slower when large *R_hinge* values are used. This slower decay of the tip oscillations was also observed in subsection 9.1. Also notice that the solution takes a long time to compute for *k_hinge = 1e7* when *R_hinge < 1e6*. This is not investigated further as detailed numerical investigations are out of the scope of this thesis.

9.3. Summary

In summary, using dampers in place of springs or a combination of dampers and springs offer drastic improvements in the computational times required and do not adversely affect the solutions.

10. Modeling of Wind Turbine Rotor Blades using the IC Beam

In this section, the methodology to model the wind turbine rotor blade using the IC beam substructure formulation will be presented. The methodology is similar to the bond graph model of the NREL 5MW wind turbine rotor developed in Xing [38]. The only difference is that the blade model in Xing [38] is developed using the linear force-free beam bond graph model as described in Karnopp, Margolis and Rosenberg [29] and Margolis [37].

First, the three-dimensional IC beam will be derived in subsection 10.1. The wind turbine blade has a complex geometry and has to be described in full three-dimensional space. Second, the appropriate interfaces to link the blade model to the aerodynamic model will be presented in subsection 10.2. Lastly, in subsection 10.3, the methodology to connect the blade model to a wind turbine rotor hub model will be presented.

10.1. Extension to Three-Dimensional IC Beam

In this subsection, the two-dimensional IC beam presented in section 3 will be extended to a full three-dimensional IC beam. Similar to section 8, only the key equations and formulations will be highlighted here.

Consider the new IC beam substructure with axial modes in Figure 90. A point P_0 on the beam in the un-deformed state moves to point P after deformation.

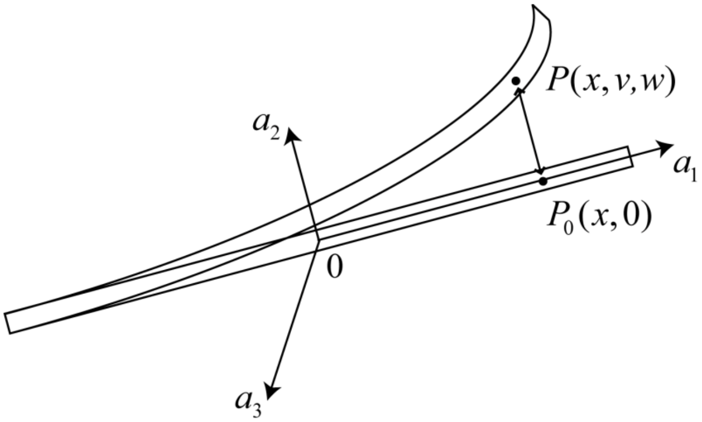

Figure 90: 3D IC Beam

Figure 91 illustrates views of the deflection point *P* from the three different two-dimensional planes.

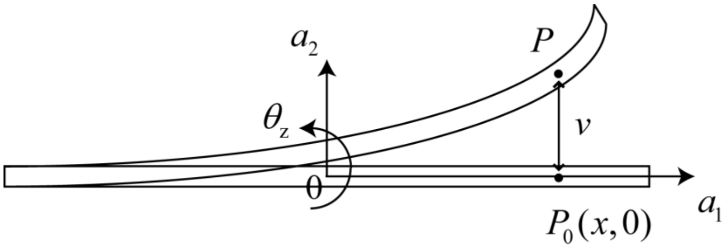

view from a_1-a_2 plane

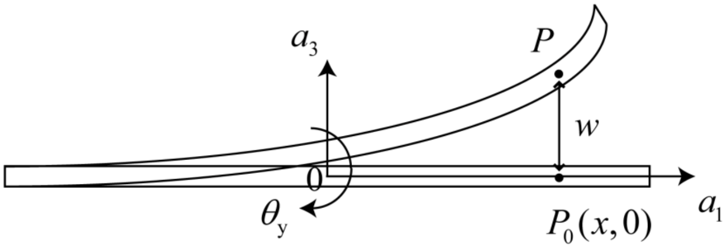

view from a_1-a_3 plane

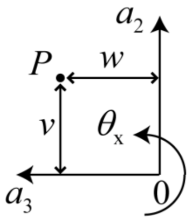

view from a_2-a_3 plane

Figure 91: Views of Point P from Three Different Two-Dimensional Planes – 3D IC Beam

With reference to equations (3.1) to (3.3), the velocity of point P is:

$$\begin{aligned}\vec{V}_P &= \left(\dot{x}_0 - v\dot{\theta}_z + w\dot{\theta}_y\right)\vec{a}_1 \\ &+ \left(\dot{y}_0 + x\dot{\theta}_z - w\dot{\theta}_x + \dot{v}\right)\vec{a}_2 \\ &+ \left(\dot{z}_0 - x\dot{\theta}_y + v\dot{\theta}_x + \dot{w}\right)\vec{a}_3\end{aligned} \tag{10.1}$$

With reference to equation (3.6), i.e. using the method of assumed mode shapes:

$$v = \sum_{j=1}^{N_v} Y_j v_j, \quad \dot{v} = \sum_{j=1}^{N_v} Y_j \dot{v}_j$$
$$w = \sum_{k=1}^{N_w} Z_k w_k, \quad \dot{w} = \sum_{k=1}^{N_w} W_k \dot{w}_k \tag{10.2}$$

With reference to equations (3.4) to (3.13), the kinetic energy of the IC beam is:

$$\begin{aligned}
T &= \frac{1}{2} M \dot{x}_0^2 + \frac{1}{2} M \dot{y}_0^2 + \frac{1}{2} M \dot{z}_0^2 \\
&+ \frac{1}{2} J_{xx} \dot{\theta}_y^2 + \frac{1}{2} J_{xx} \dot{\theta}_z^2 \\
&+ J_x \dot{y}_0 \dot{\theta}_z - J_x \dot{z}_0 \dot{\theta}_y \\
&- \sum_{j=1}^{N_v} \overline{m}_{v,j} v_j \dot{x}_0 \dot{\theta}_z + \sum_{j=1}^{N_v} \overline{m}_{v,j} v_j \dot{z}_0 \dot{\theta}_x - \sum_{j=1}^{N_v} \overline{m}_{xv,j} v_j \dot{\theta}_x \dot{\theta}_y \\
&+ \frac{1}{2} \sum_{j=1}^{N_v} \overline{m}_{vv,j} v_j^2 \dot{\theta}_x^2 + \frac{1}{2} \sum_{j=1}^{N_v} \overline{m}_{vv,j} v_j^2 \dot{\theta}_z^2 \\
&+ \sum_{k=1}^{N_w} \overline{m}_{w,k} w_k \dot{x}_0 \dot{\theta}_y - \sum_{k=1}^{N_w} \overline{m}_{w,k} w_k \dot{y}_0 \dot{\theta}_x - \sum_{k=1}^{N_w} \overline{m}_{xw,k} w_k \dot{\theta}_x \dot{\theta}_z \\
&+ \frac{1}{2} \sum_{k=1}^{N_w} \overline{m}_{ww,k} w_k^2 \dot{\theta}_x^2 + \frac{1}{2} \sum_{k=1}^{N_w} \overline{m}_{ww,k} w_k^2 \dot{\theta}_y^2 \\
&+ \sum_{j=1}^{N_v} \overline{m}_{v,j} \dot{v}_j \dot{y}_0 + \sum_{j=1}^{N_v} \overline{m}_{xv,j} \dot{v}_j \dot{\theta}_z \\
&+ \frac{1}{2} \sum_{j=1}^{N_v} \overline{m}_{vv,j} \dot{v}_j^2 \\
&+ \sum_{k=1}^{N_w} \overline{m}_{w,k} \dot{w}_k \dot{z}_0 - \sum_{k=1}^{N_w} \overline{m}_{xw,k} \dot{w}_j \dot{\theta}_y \\
&+ \frac{1}{2} \sum_{k=1}^{N_w} \overline{m}_{ww,k} \dot{w}_k^2 \\
&- \sum_{j=1}^{N_v} \sum_{k=1}^{N_w} \overline{m}_{vw,jk} v_j w_k \dot{\theta}_y \dot{\theta}_z + \sum_{j=1}^{N_v} \sum_{k=1}^{N_w} \overline{m}_{vw,jk} v_j \dot{w}_k \dot{\theta}_x - \sum_{j=1}^{N_v} \sum_{k=1}^{N_w} \overline{m}_{vw,jk} \dot{v}_j w_k \dot{\theta}_x
\end{aligned} \tag{10.3}$$

Where,

$$J_{xx} = \int_{-\frac{L}{2}}^{\frac{L}{2}} mx^2 dx, \quad J_x = \int_{-\frac{L}{2}}^{\frac{L}{2}} mxdx \tag{10.4}$$

$$\overline{m}_{v,j} = \int_{-\frac{L}{2}}^{\frac{L}{2}} mY_j dx, \quad \overline{m}_{vv,j} = \int_{-\frac{L}{2}}^{\frac{L}{2}} mY_j^2 dx, \quad \overline{m}_{xv,j} = \int_{-\frac{L}{2}}^{\frac{L}{2}} mxY_j dx$$

$$\overline{m}_{w,k} = \int_{-\frac{L}{2}}^{\frac{L}{2}} mZ_k dx, \quad \overline{m}_{ww,k} = \int_{-\frac{L}{2}}^{\frac{L}{2}} mZ_k^2 dx, \quad \overline{m}_{xw,k} = \int_{-\frac{L}{2}}^{\frac{L}{2}} mxZ_k dx$$

$$\overline{m}_{vw,jk} = \int_{-\frac{L}{2}}^{\frac{L}{2}} mY_j Z_k dx$$

With reference to equations (3.14) to (3.15), the potential energy of the IC beam is:

$$V = \frac{1}{2}\sum_{j=1}^{N_v} \overline{k}_{v,j} v_j^2 + \frac{1}{2}\sum_{k=1}^{N_w} \overline{k}_{w,k} w_k^2 \tag{10.5}$$

Where,

$$\overline{k}_{v,j} = \int_{-\frac{L}{2}}^{\frac{L}{2}} EI_{zz} \left(Y_j''\right)^2 dx \tag{10.6}$$

$$\overline{k}_{w,k} = \int_{-\frac{L}{2}}^{\frac{L}{2}} EI_{yy} \left(Z_k''\right)^2 dx$$

With reference to subsection 3.1.3 and 3.2 and considering two flapwise bending modes and two edgewise bending modes, the equations relating momentum and velocities are:

$$\begin{bmatrix} P_{x_0} \\ P_{y_0} \\ P_{z_0} \\ P_{\theta_x} \\ P_{\theta_y} \\ P_{\theta_z} \\ P_{v_1} \\ P_{v_2} \\ P_{w_1} \\ P_{w_2} \end{bmatrix} = \begin{bmatrix} M & 0 & 0 & 0 & A_{15} & A_{16} & 0 & 0 & 0 & 0 \\ 0 & M & 0 & A_{24} & 0 & J_x & \overline{m}_{v,1} & \overline{m}_{v,2} & 0 & 0 \\ 0 & 0 & M & A_{34} & -J_x & 0 & 0 & 0 & \overline{m}_{w,1} & \overline{m}_{w,2} \\ 0 & A_{42} & A_{43} & A_{44} & A_{45} & A_{46} & A_{47} & A_{48} & A_{49} & A_{410} \\ A_{51} & 0 & -J_x & A_{54} & A_{55} & A_{56} & 0 & 0 & -\overline{m}_{xw,1} & -\overline{m}_{xw,2} \\ A_{61} & J_x & 0 & A_{64} & A_{65} & A_{66} & \overline{m}_{xv,1} & \overline{m}_{xv,2} & 0 & 0 \\ 0 & \overline{m}_{v,1} & 0 & A_{74} & 0 & \overline{m}_{xv,1} & \overline{m}_{vv,1} & 0 & 0 & 0 \\ 0 & \overline{m}_{v,2} & 0 & A_{84} & 0 & \overline{m}_{xv,2} & 0 & \overline{m}_{vv,2} & 0 & 0 \\ 0 & 0 & \overline{m}_{w,1} & A_{94} & -\overline{m}_{xw,1} & 0 & 0 & 0 & \overline{m}_{ww,1} & 0 \\ 0 & 0 & \overline{m}_{w,2} & A_{104} & -\overline{m}_{xw,2} & 0 & 0 & 0 & 0 & \overline{m}_{ww,2} \end{bmatrix} \begin{bmatrix} \dot{x}_0 \\ \dot{y}_0 \\ \dot{z}_0 \\ \dot{\theta}_x \\ \dot{\theta}_y \\ \dot{\theta}_z \\ \dot{v}_1 \\ \dot{v}_2 \\ \dot{w}_1 \\ \dot{w}_2 \end{bmatrix} \tag{10.7}$$

Where,

$$
\begin{aligned}
A_{15} &= A_{51} = \overline{m}_{w,1}w_1 + \overline{m}_{w,2}w_2 \\
A_{16} &= A_{61} = -\overline{m}_{v,1}v_1 - \overline{m}_{v,2}v_2 \\
A_{24} &= A_{42} = -\overline{m}_{w,1}w_1 - \overline{m}_{w,2}w_2 \\
A_{34} &= A_{43} = \overline{m}_{v,1}v_1 + \overline{m}_{v,2}v_2 \\
A_{44} &= \overline{m}_{vv,1}v_1^2 + \overline{m}_{vv,2}v_2^2 + \overline{m}_{ww,1}w_1^2 + \overline{m}_{ww,2}w_2^2 \\
A_{45} &= A_{54} = -\overline{m}_{xv,1}v_1 - \overline{m}_{xv,2}v_2 \\
A_{46} &= A_{64} = -\overline{m}_{xw,1}w_1 - \overline{m}_{xw,2}w_2 \\
A_{47} &= A_{74} = -\overline{m}_{vw,11}w_1 - \overline{m}_{vw,12}w_2 \\
A_{48} &= A_{84} = -\overline{m}_{vw,21}w_1 - \overline{m}_{vw,22}w_2 \\
A_{49} &= A_{94} = -\overline{m}_{vw,11}v_1 - \overline{m}_{vw,21}v_2 \\
A_{410} &= A_{104} = \overline{m}_{vw,12}v_1 + \overline{m}_{vw,22}v_2 \\
A_{55} &= J_{xx} + \overline{m}_{ww,1}w_1^2 + \overline{m}_{ww,2}w_2^2 \\
A_{56} &= A_{65} = -\overline{m}_{vw,11}v_1w_1 - \overline{m}_{vw,12}v_1w_2 - \overline{m}_{vw,21}v_2w_1 - \overline{m}_{vw,22}v_2w_2 \\
A_{66} &= J_{xx} + \overline{m}_{vv,1}v_1^2 + \overline{m}_{vv,2}v_2^2
\end{aligned}
\qquad \textbf{(10.8)}
$$

And the remaining of the equations required for the IC beam implementation is:

$$
\begin{aligned}
e'_{x_0} &= -\dot{\theta}_y \frac{\partial T}{\partial \dot{z}_0} + \dot{\theta}_z \frac{\partial T}{\partial \dot{y}_0} \\
e'_{y_0} &= \dot{\theta}_x \frac{\partial T}{\partial \dot{z}_0} - \dot{\theta}_z \frac{\partial T}{\partial \dot{x}_0} \\
e'_{z_0} &= -\dot{\theta}_x \frac{\partial T}{\partial \dot{y}_0} - \dot{\theta}_y \frac{\partial T}{\partial \dot{x}_0} \\
e'_{\theta_x} &= -\dot{\theta}_y \frac{\partial T}{\partial \dot{\theta}_z} + \dot{\theta}_z \frac{\partial T}{\partial \dot{\theta}_y} \\
e'_{\theta_y} &= \dot{\theta}_x \frac{\partial T}{\partial \dot{\theta}_z} - \dot{\theta}_z \frac{\partial T}{\partial \dot{\theta}_x} \\
e'_{\theta_z} &= -\dot{\theta}_x \frac{\partial T}{\partial \dot{\theta}_y} + \dot{\theta}_y \frac{\partial T}{\partial \dot{\theta}_x} \\
e'_{v_j} &= \frac{\partial T}{\partial v_1} - \frac{\partial V}{\partial v_1} \qquad ; j = 1,2 \\
e'_{v_k} &= \frac{\partial T}{\partial w_1} - \frac{\partial V}{\partial w_1} \qquad ; k = 1,2
\end{aligned}
\qquad \textbf{(10.9)}
$$

Where,

$$\begin{aligned}
\frac{\partial T}{\partial \dot{x}_0} &= M\dot{x}_0 + \left(\overline{m}_{w,1}w_1 + \overline{m}_{w,2}w_2\right)\dot{\theta}_y - \left(\overline{m}_{v,1}v_1 + \overline{m}_{v,2}v_2\right)\dot{\theta}_z \\
\frac{\partial T}{\partial \dot{y}_0} &= M\dot{y}_0 - \left(\overline{m}_{w,1}w_1 + \overline{m}_{w,2}w_2\right)\dot{\theta}_x + J_x\dot{\theta}_z + \overline{m}_{v,1}\dot{v}_1 + \overline{m}_{v,2}\dot{v}_2 \\
\frac{\partial T}{\partial \dot{z}_0} &= M\dot{z}_0 + \left(\overline{m}_{v,1}v_1 + \overline{m}_{v,2}v_2\right)\dot{\theta}_x - J_x\dot{\theta}_y + \overline{m}_{w,1}\dot{w}_1 + \overline{m}_{w,2}\dot{w}_2
\end{aligned} \tag{10.10}$$

$$\begin{aligned}
\frac{\partial T}{\partial \dot{\theta}_x} = &-\left(\overline{m}_{w,1}w_1 + \overline{m}_{w,2}w_2\right)\dot{y}_0 + \left(\overline{m}_{v,1}v_1 + \overline{m}_{v,2}v_2\right)\dot{z}_0 \\
&+\left(\overline{m}_{vv,1}v_1^2 + \overline{m}_{vv,2}v_2^2 + \overline{m}_{ww,1}w_1^2 + \overline{m}_{ww,2}w_2^2\right)\dot{\theta}_x \\
&-\left(\overline{m}_{xv,1}v_1 + \overline{m}_{xv,2}v_2\right)\dot{\theta}_y \\
&-\left(\overline{m}_{xw,1}w_1 + \overline{m}_{xw,2}w_2\right)\dot{\theta}_z \\
&-\left(\overline{m}_{vw,11}w_1 + \overline{m}_{vw,12}w_2\right)\dot{v}_1 \\
&-\left(\overline{m}_{vw,21}w_1 + \overline{m}_{vw,22}w_2\right)\dot{v}_2 \\
&+\left(\overline{m}_{vw,11}v_1 + \overline{m}_{vw,21}v_2\right)\dot{w}_1 \\
&+\left(\overline{m}_{vw,12}v_1 + \overline{m}_{vw,22}v_2\right)\dot{w}_2 \\
\frac{\partial T}{\partial \dot{\theta}_y} = &\left(\overline{m}_{w,1}w_1 + \overline{m}_{w,2}w_2\right)\dot{x}_0 - J_x\dot{z}_0 \\
&-\left(\overline{m}_{xv,1}v_1 + \overline{m}_{xv,2}v_2\right)\dot{\theta}_x \\
&+\left(J_{xx} + \overline{m}_{ww,1}w_1^2 + \overline{m}_{ww,2}w_2^2\right)\dot{\theta}_y \\
&-\left(\overline{m}_{vw,11}v_1w_1 + \overline{m}_{vw,12}v_1w_2 + \overline{m}_{vw,21}v_2w_1 + \overline{m}_{vw,22}v_2w_2\right)\dot{\theta}_z \\
&-\overline{m}_{xw,1}\dot{w}_1 - \overline{m}_{xw,2}\dot{w}_2 \\
\frac{\partial T}{\partial \dot{\theta}_z} = &-\left(\overline{m}_{v,1}v_1 + \overline{m}_{v,2}v_2\right)\dot{x}_0 + J_x\dot{y}_0 \\
&-\left(\overline{m}_{xw,1}w_1 + \overline{m}_{xw,2}w_2\right)\dot{\theta}_x \\
&-\left(\overline{m}_{vw,11}v_1w_1 + \overline{m}_{vw,12}v_1w_2 + \overline{m}_{vw,21}v_2w_1 + \overline{m}_{vw,22}v_2w_2\right)\dot{\theta}_y \\
&+\left(J_{xx} + \overline{m}_{vv,1}v_1^2 + \overline{m}_{vv,2}v_2^2\right)\dot{\theta}_z \\
&+\overline{m}_{xv,1}\dot{v}_1 - \overline{m}_{xv,2}\dot{v}_2
\end{aligned} \tag{10.11}$$

$$\begin{aligned}
\frac{\partial T}{\partial v_1} &= \overline{m}_{v,1}\left(\dot{z}_0\dot{\theta}_x - \dot{x}_0\dot{\theta}_z\right) + \overline{m}_{vv,1}v_1\left(\dot{\theta}_x^2 + \dot{\theta}_z^2\right) - \overline{m}_{xv,1}\dot{\theta}_x\dot{\theta}_y \\
&\quad + \left(\overline{m}_{vw,11}\dot{w}_1 + \overline{m}_{vw,12}\dot{w}_2\right)\dot{\theta}_x - \left(\overline{m}_{vw,11}w_1 + \overline{m}_{vw,12}w_2\right)\dot{\theta}_y\dot{\theta}_z \\
\frac{\partial T}{\partial v_2} &= \overline{m}_{v,2}\left(\dot{z}_0\dot{\theta}_x - \dot{x}_0\dot{\theta}_z\right) + \overline{m}_{vv,2}v_2\left(\dot{\theta}_x^2 + \dot{\theta}_z^2\right) - \overline{m}_{xv,2}\dot{\theta}_x\dot{\theta}_y \\
&\quad + \left(\overline{m}_{vw,21}\dot{w}_1 + \overline{m}_{vw,22}\dot{w}_2\right)\dot{\theta}_x - \left(\overline{m}_{vw,21}w_1 + \overline{m}_{vw,22}w_2\right)\dot{\theta}_y\dot{\theta}_z \\
\frac{\partial T}{\partial w_1} &= \overline{m}_{w,1}\left(\dot{x}_0\dot{\theta}_y - \dot{y}_0\dot{\theta}_x\right) + \overline{m}_{ww,1}w_1\left(\dot{\theta}_x^2 + \dot{\theta}_y^2\right) - \overline{m}_{xw,1}\dot{\theta}_x\dot{\theta}_z \\
&\quad - \left(\overline{m}_{vw,11}\dot{v}_1 + \overline{m}_{vw,21}\dot{v}_2\right)\dot{\theta}_x - \left(\overline{m}_{vw,11}v_1 + \overline{m}_{vw,21}v_2\right)\dot{\theta}_y\dot{\theta}_z \\
\frac{\partial T}{\partial w_2} &= \overline{m}_{w,2}\left(\dot{x}_0\dot{\theta}_y - \dot{y}_0\dot{\theta}_x\right) + \overline{m}_{ww,2}w_2\left(\dot{\theta}_x^2 + \dot{\theta}_y^2\right) - \overline{m}_{xw,2}\dot{\theta}_x\dot{\theta}_z \\
&\quad - \left(\overline{m}_{vw,12}\dot{v}_1 + \overline{m}_{vw,22}\dot{v}_2\right)\dot{\theta}_x - \left(\overline{m}_{vw,12}v_1 + \overline{m}_{vw,22}v_2\right)\dot{\theta}_y\dot{\theta}_z \\
\frac{\partial V}{\partial v_1} &= \overline{k}_{v,1}v_1 \\
\frac{\partial V}{\partial v_2} &= \overline{k}_{v,2}v_2 \\
\frac{\partial V}{\partial w_1} &= \overline{k}_{w,1}w_1 \\
\frac{\partial V}{\partial w_2} &= \overline{k}_{w,2}w_2
\end{aligned} \tag{10.12}$$

Equations (10.7) and (10.9) are crucial parts of the final equations required for the IC beam implementation shown in equation (3.36). The bond graph model of the three-dimensional IC beam is similar to the model with two bending modes as illustrated in Figure 3. The only modifications are the addition of the three additional rigid body motion variables and two additional flapwise bending modes generalized variables. These modifications are straight forward and will not be presented here. Also notice that the rigid body motions, flapwise and edgewise bending deformations are nonlinearly coupled in the formulation. However the elastic deformations within the substructure are still linear and described by modal superposition.

10.2. Blade – Aerodynamics Models Interface

In this subsection, the appropriate bond graph component model to interface the blade model to the aerodynamics model will be presented. Since the elastic deformations within the IC beam substructure are described by the method of assumed modes, the aerodynamic forces on the blade will thus be described by modal forces. Also since the IC beam is formulated in the centre of mass body fixed coordinate system, the aerodynamic forces will also give contributions to the rigid body modes. The model that performs the calculation of modal forces and rigid body contributions is the blade-aerodynamics models interface.

The aerodynamic loading on the blade is first discretized into a number of segments. Then, the aerodynamic load within each segment is then integrated together with the mode shape of the IC beam substructure the segment is in over the segment length. The result is the modal load that acts at the mid-point of each segment. The modal load can be also approximated by product of the value of the mode shape function at the mid-point and the averaged aerodynamic load in the segment. The rigid body contribution from a segment is the averaged aerodynamic load in that segment and acts through the segment's mid-point. Figure 92 illustrates a blade modeled by two substructures each with four modal loading points.

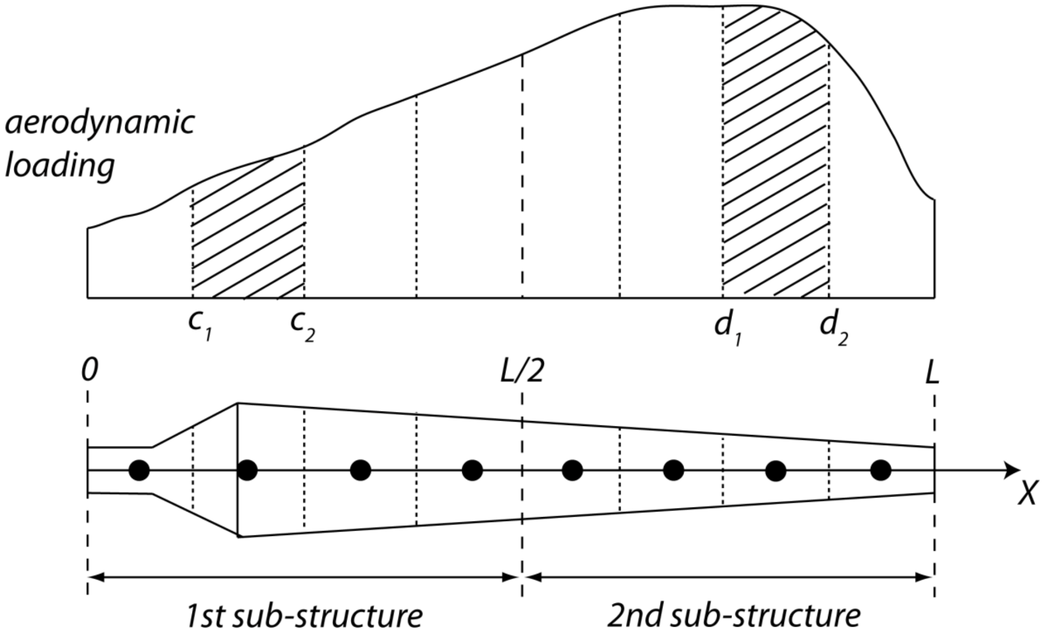

Figure 92: Blade Modeled by Two Substructures each with Four Modal Loading Points

The number of modal loading points or aerodynamic calculation points is important in ensuring the correct aerodynamic loads are calculated for the blade. In De Vaal and Xing [46], approximately 20 aerodynamic calculation sections are required to obtain converged solutions for the global responses, e.g. tower bottom bending moment, of the NREL

5MW wind turbine. While for the local responses, e.g. blade tip deflection, approximately 40 to 50 aerodynamic calculation sections are required.

The modal loads due to the second aerodynamic segment in the first substructure are:

$$\begin{aligned}
F_{v,12,j} &= \int_{c_1}^{c_2} Y_j\left(x\right) F_{aero,\vec{a}_2}\left(x\right) dx + \int_{c_1}^{c_2} Y_j'\left(x\right) M_{aero,\vec{a}_3}\left(x\right) dx \\
&\approx Y_j\left(\frac{c_1+c_2}{2}\right)\int_{c_1}^{c_2} F_{aero,\vec{a}_2}\left(x\right)dx + Y_j'\left(\frac{c_1+c_2}{2}\right)\int_{c_1}^{c_2} M_{aero,\vec{a}_3}\left(x\right)dx \\
F_{w,12,k} &= \int_{c_1}^{c_2} Z_k\left(x\right) F_{aero,\vec{a}_3}\left(x\right) dx + \int_{c_1}^{c_2} Z_k'\left(x\right) M_{aero,\vec{a}_2}\left(x\right) dx \\
&\approx Z_k\left(\frac{c_1+c_2}{2}\right)\int_{c_1}^{c_2} F_{aero,\vec{a}_3}\left(x\right)dx + Z_k'\left(\frac{c_1+c_2}{2}\right)\int_{c_1}^{c_2} M_{aero,\vec{a}_2}\left(x\right)dx
\end{aligned} \tag{10.13}$$

Where,

$F_{v,mn,j}$	Modal force in the *'v'* direction (m-th substructure, n-th modal loading point, j-th mode)
$F_{w,mn,k}$	Modal force in the *'w'* direction (m-th substructure, n-th modal loading point, k-th mode)
$F_{aero,\vec{a}_2}(x)$	Aerodynamic force in the *'a_2'* direction along the substructure
$M_{aero,\vec{a}_2}(x)$	Aerodynamic moment about the *'a_2'* direction along the substructure
$F_{aero,\vec{a}_3}(x)$	Aerodynamic force in the *'a_3'* direction along the substructure
$M_{aero,\vec{a}_3}(x)$	Aerodynamic moment about the *'a_3'* direction along the substructure

The rigid body contributions due to the second aerodynamic segment in the first substructure are:

(10.14)

$$F_{y_0,12} = \int_{c_1}^{c_2} F_{aero,\vec{a}_2}(x)dx$$

$$M_{\theta_z,12} = \int_{c_1}^{c_2} M_{aero,\vec{a}_3}(x)dx + \frac{l}{2} \cdot \int_{c_1}^{c_2} F_{aero,\vec{a}_2}(x)dx$$

$$F_{z_0,12} = \int_{c_1}^{c_2} F_{aero,\vec{a}_3}(x)dx$$

$$M_{\theta_y,12} = \int_{c_1}^{c_2} M_{aero,\vec{a}_2}(x)dx - \frac{l}{2} \cdot \int_{c_1}^{c_2} F_{aero,\vec{a}_3}(x)dx$$

Where,

$F_{y_0,mn}$	Rigid body contribution in the *'y_0'* direction (m-th substructure, n-th modal loading point)
$M_{\theta_z,mn}$	Rigid body contribution in the *'θ_z'* direction (m-th substructure, n-th modal loading point)
$F_{z_0,mn}$	Rigid body contribution in the 'z_0' direction (m-th substructure, n-th modal loading point)
$M_{\theta_y,mn}$	Rigid body contribution in the *'θ_y'* direction (m-th substructure, n-th modal loading point)
l	Length of substructure

Similarly, the modal loads and rigid body contributions due to the third aerodynamic segment in the second substructure are:

(10.15)

$$F_{v,23,j} \approx Y_j\left(\frac{d_1+d_2}{2}\right)\int_{c_1}^{c_2} F_{aero,\vec{a}_2}(x)dx + Y_j'\left(\frac{d_1+d_2}{2}\right)\int_{c_1}^{c_2} M_{aero,\vec{a}_3}(x)dx$$

$$F_{w,23,k} \approx Z_k\left(\frac{d_1+d_2}{2}\right)\int_{c_1}^{c_2} F_{aero,\vec{a}_3}(x)dx + Z_k'\left(\frac{d_1+d_2}{2}\right)\int_{c_1}^{c_2} M_{aero,\vec{a}_2}(x)dx$$

(10.16)

$$F_{y_0,23} = \int_{d_1}^{d_2} F_{aero,\vec{a}_2}(x)dx$$

$$M_{\theta_z,23} = \int_{d_1}^{d_2} M_{aero,\vec{a}_3}(x)dx + \frac{l}{2} \cdot \int_{d_1}^{d_2} F_{aero,\vec{a}_2}(x)dx$$

$$F_{z_0,23} = \int_{d_1}^{d_2} F_{aero,\vec{a}_3}(x)dx$$

$$M_{\theta_y,23} = \int_{d_1}^{d_2} M_{aero,\vec{a}_2}(x)dx - \frac{l}{2} \cdot \int_{d_1}^{d_2} F_{aero,\vec{a}_3}(x)dx$$

An equivalent bond graph model of the interface between the first IC beam substructure and the second aerodynamic segment is presented in Figure 93. This IC beam has two flapwise and two edgewise bending modes. It is straight forward to extend this model to incorporate additional bending modes and/or more aerodynamics segments.

THIS PAGE INTENTIONALLY LEFT BLANK.

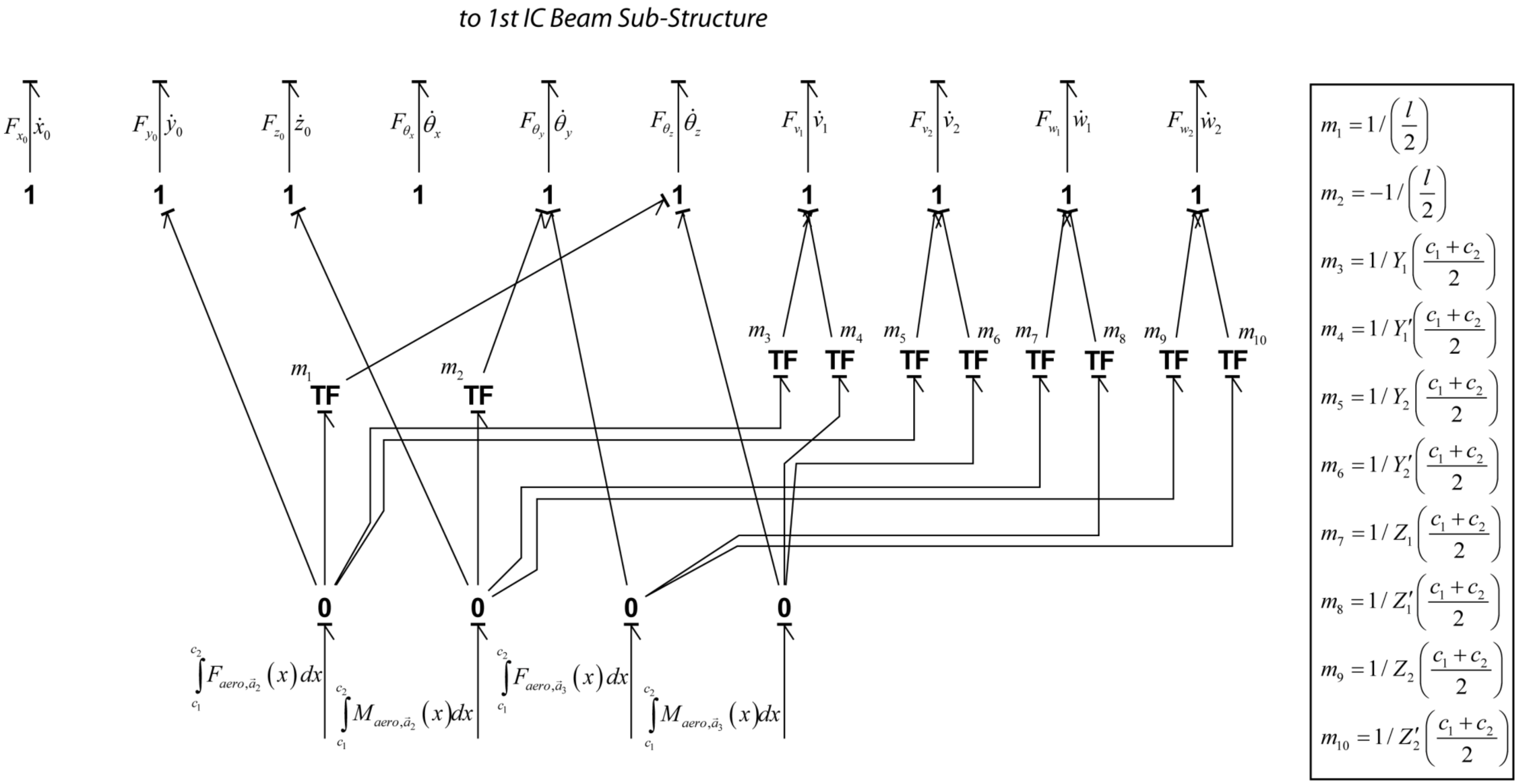

Figure 93: Example of Blade-Aerodynamic Models Interface

THIS PAGE INTENTIONALLY LEFT BLANK.

10.3. Connection of Blade Model to Rigid Hub Model

The Karnopp-Margolis method [1] can be used for the connection of the blade to the rigid hub model. This method has also been applied for connecting the elastic blade body to the rigid hub body in the bond graph model of the wind turbine rotor in Xing [38]. As mentioned in subsections 4.2.1.3 and 4.2.1.4, differential causalities will occur when two bodies are connected directly together. The Karnopp-Margolis method ensures that the system will remain in complete integral causality. A system in complete integral causality yields a much more efficient numerical system than a system with differential causality. The model implementation of this connection is similar to the interconnecting hinge model presented in subsection 4.2.1.4. It is straight forward to modify the interconnecting hinge model into the connection model for the blade and hub. Therefore, no further details will be presented here.

THIS PAGE INTENTIONALLY LEFT BLANK.

11. Conclusions and Future Work

11.1. Conclusions

In this thesis, an Inertia-Capacitance (IC) beam substructure formulation based on bond graph terminology was developed. The IC beam is formulated in the centre of mass body fixed coordinate system. This coordinate system allows for easy interfacing of the IC beam in a multibody system setting. This multibody floating frame approach is also much faster than nonlinear finite element methods. Elastic deformations in the IC beam are assumed to be small and described by the method of assumed mode shapes. The formulation couples rigid body motions and elastic deformations in a nonlinear fashion. Detailed derivations for a two-dimensional planar IC beam with bending modes were presented. Brief derivations were also presented for the two-dimensional IC beam with both bending and axial modes and for the three-dimensional IC beam with bending modes. A modal acceleration method via the decoupling of modes was also developed as the conventional modal acceleration method is not suitable for use in the IC beam.

Extensive linear and nonlinear numerical tests were performed on the two-dimensional planar IC beam using the model description of the rotating beam problem in Wu and Haug [25]. The IC beam was also verified against the numerical results presented in Wu and Haug [25]. The Karnopp-Margolis method [1] was used in the model set-ups to ensure complete integral causality in the system. This results in an efficient numerical system.

The static tests show that the IC beam substructure is capable in solving nonlinear static problems. Also, it was shown that the use of unsuitable mode shapes e.g. the free-free modes will lead to slow modal convergence.

The spin-up maneuver problem is solved in the dynamic tests. Convergence studies of various model parameters were performed. More substructures are required to ensure accuracy in the more nonlinear cases, i.e. $\omega_s = 4$ *& 8 rad/s*. For these cases, the solution for the tip displacements will be unbounded if only a single substructure is prescribed. Prescribing insufficient number of substructures will result in an overestimation of the tip displacements. A small absolute error tolerance value must also be specified. Insufficiently small values give rise to incorrect high frequency oscillations. The resistance value of the resistor in the rotating hinge must be large to ensure accurate results. Using different resistance values do not affect the amount of computational time required. The stiffness values of the springs in all hinges must large to ensure accuracy and that the numerical solutions will proceed. Using larger stiffness values lead to increased computational requirements. The modal acceleration tests show that only the first mode is strongly coupled to the rigid body motions and the rest of the modes can be decoupled and yet yield virtually the same solution. There are significant computational savings if a large number of modes can be decoupled.

10 to 15 modes are required for convergence in the multi substructure cases for both the static and dynamics tests. Prescribing too little number of modes will result in an underestimation of the tip displacements. For the single substructure case, the solution is entirely dominated by the first mode.

The additional of axial modes in the two-dimensional planar IC beam does not improve the solution for the spin-up maneuver problem. The only additional benefit is that the steady state axial lengthening is modeled correctly. However, this displacement is significantly smaller than the minimum axial shortening, tip deflection and slope experienced during the spin-up maneuver. Therefore, including axial modes does not justify the additional computational times required.

In general, more computational efforts are required when more modes, more substructures and/or higher ω_s values are used. Using dampers in place of springs or a combination of dampers and springs at the hinges can drastically improve the computational times required.

Lastly, the methodology to apply the IC beam formulation to the wind turbine rotor blades was presented. The model to interface the blade and aerodynamic models was presented in detail. The method to connect the blade model to the rigid hub model was also discussed.

In conclusion, an efficient IC beam substructure formulation based on bond graph terminology was developed. The IC beam was shown to perform well for large deflection static problems and rotating beam problems. The IC beam looks promising to be further developed for application in wind turbine structural dynamics problems.

11.2. Future Work

The IC beam formulation developed in this thesis provides a framework to solve wind turbine structural dynamics problems. The IC beam can be applied to the wind turbine problem to further understand its applicability and capability. The IC beam can be used to construct the wind turbine model and then interfaced with preexisting aerodynamic software such as AeroDyn [47]. Detailed numerical investigations should be also performed to fully understand its numerical behavior.

THIS PAGE INTENTIONALLY LEFT BLANK.

References

[1] *Bond Graph Modeling of Multibody Systems: A Library of Three-Dimensional Joints.* **Zeid, A. and Chung, C.H.** 4, pp 605-636, s.l. : Journal of Franklin Institute, 1992, Vol. 329.

[2] **Jonkman, J., et al.** *Definition of a 5-MW Reference Wind Turbine for Offshore System Development, Technical Report.* s.l. : NREL/TP-500-38060, 2009.

[3] **Xing, Y.H.** *Effect of Blade Model Flexibility on the Dynamic Response of a Large Onshore Wind Turbine.* Trondheim : NTNU PhD Course MR8205 Project Report, 2010.

[4] **Iarsen, T.J.** *How 2 HAWC2.* Roskilde : Risø National Laboratory, Technical University of Denmark, 2009. Risø-R-1597 (ver. 3-9)(EN).

[5] *Influence of Wind Turbine Flexibilty on Loads and Power Production.* **Ahlstorm, A.** 3, 237-249, s.l. : Wind Energy, 2005, Vol. 9.

[6] *Non-linear Dynamics of Wind Turbine Wings.* **Larsen, J.W. and S.R.K, Nielsen.** pp 629-643, s.l. : International Journal of Non-Linear Mechanics, 2006, Vol. 41.

[7] *Nonlinear Parameteric Instability of Wind Turbine Wings.* **Larsen, J.W. and Nielsen, S.R.K.** pp 64-82, s.l. : Journal of Sound and Vibration, 2007, Vol. 299.

[8] **Holm-Jørgensen, K.** *PhD Thesis: Nonlinear Multibody Dynamics of Wind Turbines.* s.l. : Aalborg University, Department of Civil Engineering,Division of Structural Mechanics, 2009. DCE Thesis No. 19.

[9] *A Criterion on Inclusion of Stress Stiffening Effects in Flexible Multibody Dynamic System Simulation.* **Ryu, J., Kim, S.S. and Kim, S.S.** 6, pp 1035-1048, s.l. : Computers and Structures, 1997, Vol. 62.

[10] *Dyanmic Modelling and Control of a Rotating Euler-Beroulli Beam.* **Yang, J.B., Jiang, L.J. and Chen, D.CH.** pp 863-875, s.l. : Journal of Sound and Vibration, 2004, Vol. 274.

[11] *Frequency Analysis of a Rotating Cantilever Beam Using Assumed Mode Method with Coupling Effect.* **Cheng, J.C., Xu, H. and Yan, A.** 1, pp 25-47, s.l. : Mechanics Based Design of Structures and Machines, 2006, Vol. 34.

[12] *Modal Analysis and Shape Optimization of Rotating Cantilever Beams.* **Yoo, H.H, Cho, J.E. and Chung, J.** pp 223-241, s.l. : Journal of Sound and Vibration, 2006, Vol. 290.

[13] *Vibration Analysis of Rotating Cantilever Beams.* **Yoo, H.H. and Shin, S.H.** 5, pp 807-828, s.l. : Journal of Sound and Vibration, 1998, Vol. 212.

[14] *Finite-Element Based Nonlinear Modal Reduction of a Rotating Beam with Large-Amplitude Motion.* **Apiwattanaluggarn, P., et al.** pp 235-263, s.l. : Journal of Vibration and Control, 2003, Vol. 9.

[15] *Computational Strategies for Flexible Multibody Systems.* **Wasfy, T.M. and Noor, A.K.** 6, s.l. : Applied Mechanics Review, 2003, Vol. 56.

[16] *Nonlinear Normal Modes for Vibratory Systems Under Harmonic Excitation.* **Jiang, D., Pierre, C. and Shaw, S.W.** 4-5, pp 791-812, s.l. : Journal of Sound and Vibration, 2005, Vol. 20.

[17] *Nonlinear Normal Modes and Their Application in Structural Dynamics.* **Pierre, C., Jiang, D. and Shaw, S.** s.l. : Mathematical Problems in Engineering, 2006, Vols. pp 1-15.

[18] *Normal Modes for Non-Linear Vibratory Systems.* **Shaw, S.W. and Pierre, C.** 1, pp 85-124, s.l. : Journal of Sound and Vibration, 1993, Vol. 164.

[19] *Accurate Reduced-Order Models for a Simple Rotor Blade Model Using Nonlinear Normal Modes.* **Pesheck, E., Pierre, C. and Shaw, S.W.** pp 1085-1097, s.l. : Mathematical and Computer Modelling , 2001, Vol. 33.

[20] *Modal Reduction of a Nonlinear Rotating Beam Through Nonlinear Normal Modes.* **Pesheck, E., Pierre, C. and Shaw, S.W.** pp 229-236, s.l. : Journal of Vibration and Acoustics, 2002, Vol. 124.

[21] *Nonlinear Normal Modes of a Rotating Shaft Based on the Invariant Manifold Method.* **Legrand, M., et al.** 4, pp 319-335, s.l. : International Journal of Rotating Machinery, 2004, Vol. 10.

[22] *The Construction of Non-Linear Normal Modes for Systems with Internal Resonance.* **Jiang, D., Pierre, C. and Shaw, S.W.** pp 729-746, s.l. : International Journal of Non-Linear Mechanics, 2005, Vol. 40.

[23] *A New Galerkin-Based Approach for Accurate Non-Linear Normal Modes Thtough Invariant Manifolds.* **Pesheck, E. and Pierre, C.** 5, pp 971-993, s.l. : Journal of Vibration and Sound, 2002, Vol. 249.

[24] *Invited Paper: Non-Linear Normal Modes and Their Applications in Vibration Theory: An Overview.* **Vakakis, A.F.** 1, pp 3-22, s.l. : Mechanical Systems and Signal Processing, 1997, Vol. 11.

[25] *Geometric Non-Linear Substructuring for Dynamics of Flexible Mechanical Systems.* **Wu, C.H. and Haug, E.J.** 2211-2226, s.l. : International Journal for Numerical Methods in Engineering, 1988, Vol. 26.

[26] *A Substructure Technique for Dynamics of Flexible Mechanical Systems with Contact-Impact.* **Wu, S.C. and Haug, E.J.** 390-398, s.l. : ASME Journal of Mechanical Design, 1990, Vol. 112.

[27] *Non-Linear Substructure Approach for Dynamic Analysis of Rigid Flexible Multibody Systems.* **Liu, A.Q. and Liew, K.M.** 379-390, s.l. : Computational Methods in Applied Mechanics and Engineering, 1994, Vol. 114.

[28] *On the Modal Acceleration Method in Structural Dyanmics. Mode Truncation and Static Correction.* **H.L., Soriano and F., Venancio Filho.** 5, pp 777-782, s.l. : Computers and Structures, 1988, Vol. 29.

[29] **Karnopp, D.C., Margolis, D.L. and Rosenberg, R.C.** *System Dyanmics: Modeling and Simulation of Mechatronic Systems.* New Jersey : John Wiley & Sons Inc., 2006. ISBN 0-471-70965-4.

[30] **Williams, D.** *Dynamic Loads in Aeroplanes under Given Impulsive Loads with Particular Reference to Landing and Gust Loads on a Large Flying Boat.* s.l. : Great Britain RAE Reports, 1945. SME 3309 and 3316.

[31] **Bisplinghoff, R.L., Ashley, H. and R.L., Halfman.** *Aeroelasticity.* Cambridge, Mass : Addison-Wesley Publishing Company Inc., 1955. ISBN 0-486-69189-6.

[32] *On the Number of Modes Necessary for Accurate Response and Resulting Forces in Dynamic Analysis.* **Maddox, N.R.** pp 516-517, s.l. : Journal of Applied Mechanics, ASME, 1975, Vol. 42.

[33] *On the Accuracy of Mode Superposition Analysis in Structural Dynamics.* **Hansteen, O.E. and Bell, K.** pp 405-411, s.l. : Earthquake Engineering and Structural Dynamics, 1979, Vol. 7.

[34] *On the Applications of the Mode-Acceleration Method to Structural Engineering Problems.* **Cornwell, R.E., Craig Jr, R.R. and Jonhson, C.P.** pp 679-688, s.l. : Earthquake Engineering and Structural Dynamics, 1983, Vol. 11.

[35] *A Method for Improving Dynamic Solutions in Flexible Multibody Dynamics.* **Ryu, J., Kim, H.S. and Wang, S.** 6, pp 765-776, s.l. : Computers and Structures, 1998, Vol. 66.

[36] **Pedersen, E. and Engja, H.** *Mathematical Modeling and Simulation of Physical Systems.* s.l. : Department of Marine Technology, NTNU Trondheim, 2008. UK-2008-5.

[37] *Bond Graphs, Normal Modes and Vehicular Structures.* **Margolis, D.L.** pp 49-63, s.l. : Vehicle System Dynamics, 1978, Vol. 7.

[38] **Xing, Y.H.** *Bond Graph Modeling of Wind Turbine Rotor.* Trondheim : NTNU PhD Course MR8400 Project Report, 2010.

[39] *Lagrange's Equations for Complex Bond Graphs Systems.* **Karnopp, D.** Series G, pp 300-306, s.l. : ASME Journal of Dyanmic Systems Measurement and Control, 1977, Vol. 99.

[40] *Hybrid State Equations of Motion for Flexible Bodies in Terms of Quasi-Coordinates.* **Meirovitch, L.** pp. 1008-1013, s.l. : Journal of Guidance, Control and Dynamics, 1991, Vol. 14.

[41] **Meirovitch, L.** *Methods of Analytical Dyanmics.* New York : McGraw-Hill, 1970. ISBN 0-486-43239-4.

[42] *Rotordynamics and Bond Graphs: Basic Model.* **Pedersen, E.** 4, pp 337-352, s.l. : Mathematical and Computer Modelling of Dynamic Systems, 2009, Vol. 15.

[43] *The Matlab ODE Suite.* **Shampine, L.F. and Reichelt, M.W.** pp 1-22, s.l. : SIAM Journal of Scientific Computing, 1997, Vol. 18.

[44] *Solving Index-1 DAEs in Matlab and Simulink.* **Shampine, L.F., Reichelt, M.W. and Kierzenka, J.A.** pp 538-552, s.l. : SIAM Review, 1999, Vol. 41.

[45] *On the Finite Deflections of Thin Beams.* **Holden, J.T.** pp 1051-1055, s.l. : International Journal of Solids and Structures, 1972, Vol. 8.

[46] **De Vaal, J. and Xing, Y.H.** *Wind Turbine Modeling Using HAWC2.* Trondheim : NTNU PhD Course BA8607 Project, 2010.

[47] **Moriarty, P. J. and Hansen, A. C.** *AeroDyn Theory Manual.* Colorado : National Renewable Energy Laboratory, 2005.